DEVELOPMENT OF NANOPARTICLE-BASED APPROACHES FOR THE TREATMENT AND IMAGING OF PANCREATIC CANCER

by

Mubin Tarannum

A dissertation submitted to the faculty of
The University of North Carolina at Charlotte
in partial fulfillment of the requirements
for the degree of Doctor of Philosophy in
Nanoscale Science

Charlotte

2020

Approved by:

_____
Dr. Juan L. Vivero-Escoto

_____
Dr. Pinku Mukherjee

_____
Dr. Didier Dréau

_____
Dr. Kirill Afonin

_____
Dr. Jerry Troutman

ABSTRACT

MUBIN TARANNUM. Development of nanoparticle-based approaches for treatment and imaging of pancreatic cancer. (Under the direction of DR. JUAN L. VIVERO-ESCOTO)

Pancreatic ductal adenocarcinoma (PDAC) is a type of exocrine pancreatic cancer which accounts for over 90% of cases. PDAC is the fourth-leading cause of cancer-related mortality in the United States with a 5-year survival rate of 9% with little to no change in the last 40 years. The high mortality and poor prognosis of PDAC can be attributed to multifactorial reasons including late diagnosis, intrinsic and acquired resistant behavior, early micrometastatic dissemination, desmoplastic effect, and heterogeneities in tumors, rendering the current treatments rather ineffective. Hence, it is imperative to focus on improved methods for the detection and treatment of PDAC. Mesoporous silica nanoparticles (MSN)-based modalities can be a promising approach for PDAC treatment, owing to their outstanding properties. Research in this Thesis focuses on the development of novel MSN-based modalities to address many of the drawbacks impeding the success of current PDAC therapies.

In Chapter 2, MSNs were used to achieve high drug loading and provide synergistic co-delivery of Gem/cisPt. The MSN platform was functionalized with a novel tMUC1-specific antibody (TAB004) for targeted drug delivery. The TAB004-Gem-cisPt-MSNs showed increased accumulation in the tumors, which therapeutically outperformed the untargeted MSN material as well as free Gem/cisPt. The carrier design using chemical conjugation of drugs to MSNs along with stimuli-responsive behavior eliminated systemic drug release and off-target toxicities in KCM syngeneic mice. For Chapter 3, sequential therapy was designed to combat the stromal barrier via SHh

inhibition using cyclopamine (CyP). The time-staggered sequential combination therapy of CyP-MSNs plus Gem-cisPt-MSNs showed increased tumor inhibition in aggressive HPAF II tumor-bearing mice and showed changes in the tumor stroma. Chapter 4 addresses the early diagnosis of PDAC which is essential to improve PDAC prognosis. In this direction, target specific TAB004-MSNs was used as an imaging and diagnostic probe. TAB004-MSNs demonstrated increased selectivity in tMUC1-expressing PDAC cells. More importantly, TAB004-MSNs could selectivity accumulate in the pancreas at an early PanIN lesion stage. The versatile uses of MSNs and their thorough investigation in KCM, syngeneic mice, HPAF II xenograft mice, and transgenic PDA.MUC1 mice demonstrate safety, bioimaging, and therapeutic performance of MSNs. Overall, the data in this Thesis provides evidence for successful multi-modal applications of MSNs and provides proof for the clinical translation of our platform.

Acknowledgments

TABLE OF CONTENTS

LIST OF FIGURES

LIST OF TABLES

LIST OF ABBREVIATIONS

TME	tumor microenvironment
EPR	enhanced permeation and retention effect
PDAC	pancreatic ductal adenocarcinoma
PanIN	pancreatic intraepithelial neoplasia
IPMN	intraductal papillary mucinous neoplasia
MCN	mucinous cystic neoplasia
miRNA	micro RNA
lncRNA	long non-coding RNA
Gem	Gemcitabine
dFdC	2',2'-difluoro 2'-deoxycytidine
NT	nucleoside tranporters
ENT	equilibrative nucleoside tranporters
CNT	concentrative nucleoside tranporters
dCK	deoxycytidine kinase
dFdCMP	2',2'-difluoro 2'-deoxycytidine monophosphate
dFdCTP	2',2'-difluoro 2'-deoxycytidine triphosphate
CDA	cytidine deaminase
dFdU	2',2'-difluorodeoxyuridine
RR	ribonucleotide reductase
dNTP	deoxynucleotide
RRM1	ribonucleotide reductase subunit M1

5-FU	5-fluorouracil
RR	response rate
mPFS	median progression-free survival
OS	overall survival
FDA	food drug administration
EGFR	epidermal growth factor receptor
HER2	human epidermal growth factor receptor 2
VEGFR	vascular endothelial growth factor receptor
HA	hyaluronan
MMP	metalloproteinases
CTGF	connective tissue growth factor
PEGPH20	PEGylated recombinant hyaluronidase
IFP	interstitial fluid pressure
GEM	genetically engineered mice
MPS	mononuclear phagocyte system
GMP	gemcitabine monophosphate
CTX	cetuximab
CPT	camptothecin
uPAR	urokinase plasminogen activator receptor
IONPs	iron oxide nanoparticles
MRI	magnetic resonance imaging
SPION	superparamagnetic iron oxide nanoparticles
MSN	mesoporous silica nanoparticles

CMC	critical micellar concentration
CTAB	cetyl trimethyl ammonium bromide
TEOS	tetraethyl orthosilicate
PEI	polyethyleneimine
PEG	polyethylene glycol
PDX	patient-derived tumor xenograft
tMUC1	tumor-associated mucin1
cisPt	cisplatin
NCI	national cancer institute
EMT	epithelial-mesenchymal transition
VNTR	variable number tandem repeat
CDRs	complementary determinant regions
APTES	(3-aminopropyl)triethoxysilane
DEA	diethanolamine
TPMP	3-(trihydroxylsilyl) propyl methylphosphonate monosodium salt
SPDP	N-succinimidyl-3-(2-pyridine) propionate
TBTU	O-(Benzotriazol-1-yl)-N,N,N',N'-tertamethyluronium tetrafluoro borate
DIPEA	N, N-Diisopropylethylamine
EDC	1-Ethyl-3-(3-dimethylaminopropyl) carbodiimide
TFA	trifluoroacetic acid
TEA	triethylamine
MeO-PEG-NHS	methoxy polyethylene glycol N-hydroxysuccinimide

MAL-PEG-SCM	Maleimide polyethylene glycol N-hydroxysuccinimide
RPMI	rosewell park memorial institute
DMEM	dulbecco modified eagle medium
PBS	phosphate buffer saline
NEAA	non-essential amino acids
FBS	fetal bovine serum
ICP-OES	inductively coupled plasma optical emission spectroscopy
ICP-MS	inductively coupled plasma mass spectrometry
DMSO	dimethyl sulfoxide
DMF	dimethylformamide
DCM	dichloromethane
HCl	hydrochloric acid
NIR	near-infrared
SATA	N-succinimidyl S-acetythioacetate
TEM	transmission electron microscopy
AAS	atomic absorption spectroscopy
DLS	dynamic light scattering
TGA	thermogravimetric analysis
MTS	[3-(4,5-dimethythiazol-2-yl)-5-(3-carboxymethoxyphenyl)-2-(4-sulfophenyl)-2H-tetrozolium]
EMEM	Eagle's minimal essential medium
CI	Combination index
FACS	fluorescence-activated cell sorting

ROI	region of interest
H&E	hematoxylin and eosin
IHC	immunohistochemistry
IC_{50}	half-maximal inhibitory concentration
FTIR	fourier-transform infrared spectroscopy
^{13}C NMR	carbon-13 nuclear magnetic resonance
^{1}H NMR	proton nuclear magnetic resonance
D_h	hydrodynamic diameter
DDR	DNA damage response
FITC	fluorescein isocyanate
PI	propidium iodide
RES	reticuloendothelial system
PK	pharmacokinetics
PD	pharmacodynamics
AST	aspartate aminotransferase
ALT	alanine transaminase
BUN	blood urea nitrogen
SHh	sonic hedgehog
PTCH	patched receptor
SMO	Smoothened receptor
CyP	cyclopamine
UHPLC	ultra high performance liquid chromatography
NSG	NOD SCID gamma

GFR   growth factor reduced

HF   hydrofluoric acid

HRI   high-risk individuals

CEA   carcinoembryonic antigen

CHAPTER 1: INTRODUCTION

1.1 Cancer.

Cancer encompasses an array of complex diseases involving dynamic changes in the genome of tumor cells and surrounding microenvironment, resulting in a complicated tissue-like system far exceeding the complexity of healthy organs. The difficulty in treating cancer stems from the fact that different cancers behave as individual diseases (1). Cancers vary in the growth rate, the origin of cells in the organ, metastatic potential, and the designated site of cancer spread, which leads to differences in response to therapies. These differences hamper patients' selection, tumor behavior prediction, clinical outcome, development of resistance, and relapse (2).

1.1.1 Hallmarks of cancer.

Hanahan and Weinberg described the key cancer hallmarks in 2000 as six specific characteristics manifested by cancer cells to dictate malignant growth (3). These hallmark list was revised in 2011 to include four additional enabling and new emerging characteristics of cancer (**Figure 1.1**) (4). They include sustaining proliferative signaling, evading growth suppressors, activating invasion and metastasis, enabling replicative immortality, inducing angiogenesis, and resisting cell death. Enabling hallmarks of cancer encompass metabolic reprogramming and immune evasion. These biological capabilities provide a logical framework for understanding the characteristics of cancer and its remarkable diversity. Tumors are not just an insular mass of cancer cells; instead, they form a complex tissue-like system, where distinct components have a specific role in tumorigenesis, progression, and metastatic dissemination. These cellular and non-cellular components, now well established as "tumor microenvironment" (TME), contribute

heavily to the development of the cancer hallmarks (5, 6).
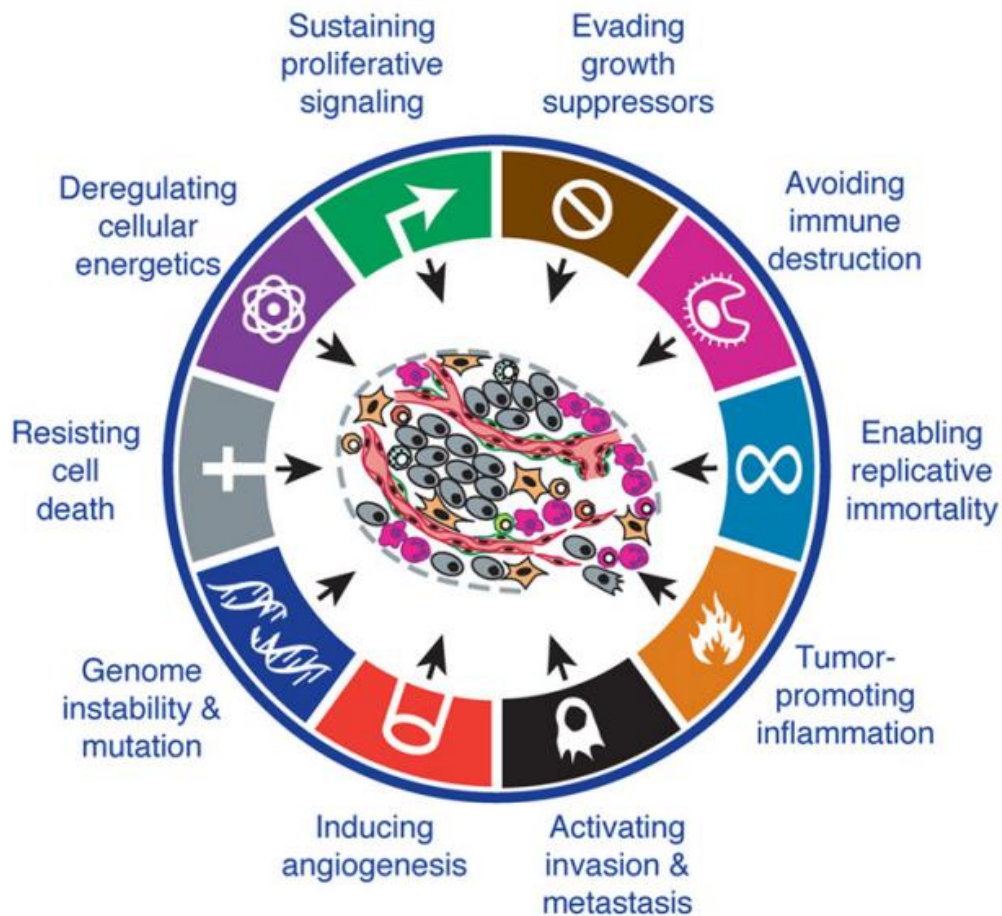
Figure 1.1. The hallmarks of cancer, as described by Hanahan and Weinberg (4). Cancer cells transiently acquire these properties during the process of evolution from the normal state to the neoplastic state.

Healthy cells strictly control the production and release of growth-promoting signals that instruct the cell division, growth, and cell death, ensuring normal tissue function and homeostasis. On the contrary, cancer cells can **sustain proliferative potential** by overexpressing the growth factor ligands, mutational defects in proliferation pathways, and disrupting negative feedback (7-9). This sustained proliferation is accompanied by the ability of cancer cells to circumvent robust cellular programs and **evade growth suppressors.** Cancer cells have shown defective checkpoints like tumor

suppressor genes (RB and TP53), and they adapt to abolish contact inhibition at an early stage (10).

The intrinsic and extrinsic programmed cell death mechanisms, i.e., cell apoptosis, in a healthy cell serves as a significant barrier to cancer progression. Cancer cells have evolved a variety of strategies for **resisting cell death** through the loss of tumor suppressor genes and its regulation, increased expression of the anti-apoptotic proteins (Bcl-2, Bcl-xL, Mcl-1), and decreased expression of pro-apoptotic proteins (Bid, Noxa, Bmf) (11, 12). To acquire **replicative immortality**, cancer cells evade the telomere-related senescence via various strategies (13, 14). Tumors **induce angiogenesis** to sprout new blood vessels that are required to support tumor growth with nutrients and oxygen (15, 16) (**Figure 1.1**). Tumor neovasculature is marked by precocious capillary sprouting, convoluted and excessive vessel branching, distorted and enlarged vessels, erratic blood flow, micro-hemorrhaging, and the leakiness (17). This provides the basis of the enhanced permeability and retention (EPR) effect, which is an essential concept for the accumulation of nanoparticles in tumors.

Cancer cells acquire and lose various properties to undergo the multistep process of **invasion and metastasis**. The process starts with local invasion of cancer cells from the primary tumor, intravasation into nearby blood and lymphatic vessels. This is followed by the transit of cancer cells through the circulation followed by escape (extravasation) into the parenchyma of the distant tissue. The cancer cells finally colonize into metastatic lesions in the distant host tissue (18).

In addition, the uncontrolled growth of the cancer cells demands **reprogramming in energy metabolism** to fuel the continuous growth-division process. The abilities

mentioned above result in sustained cell growth, which also requires solid tumors to **avoid the detection of immune cells** by disabling the components of the immune system and induce immune-suppressive properties in the tumor (19, 20). Taken together, the cancer hallmarks provide a solid foundation of cancer biology for their mechanistic underpinnings and to shape the research direction for emerging therapeutics (**Figure 1.1**).

1.2 Pancreatic ductal adenocarcinoma (PDAC).

The pancreas is a gland situated deep in the abdomen between the stomach and the spine. The pancreas is responsible for exocrine and endocrine functions like the production of enzymes to aid in digestion and vital hormones to control blood sugar, respectively (21). About 95% of the pancreatic cancers are exocrine in origin and originate from the ductal cells, referred to as pancreatic ductal adenocarcinoma (PDAC) (22). Despite having a low rate of incidence (0.01%), PDAC is ranked high as the fourth leading cause of cancer-related mortality (**Figures 1.2a and 1.2b**).
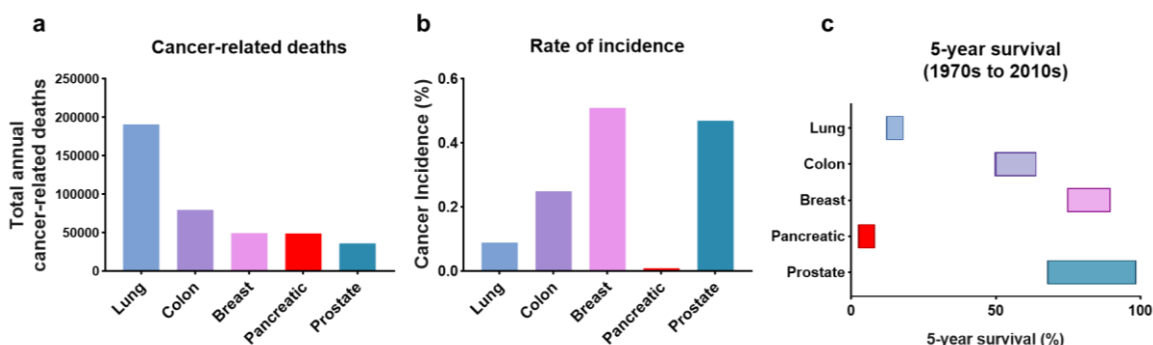
Figure 1.2. Graph representing the total deaths, incidence, and 5-year survival of top five cancers. **(a)** The total annual number of deaths related to cancer in the USA in 2017 based on cancer type, emphasizing the high ranking of pancreatic cancer as the fourth leading cause. **(b)** Pancreatic cancer has low incidence among top five cancers. **(c)** A graph to represent the change in 5-year survival in the range from 1970-1977 to 2007-2013, which indicates that the 5-year survival of pancreatic cancer has not significantly increased over 40 years (23, 24).

PDAC is an aggressive and devastating malignant disease that poses a substantial health impact, with approximately 57,600 new cases and 47,050 deaths anticipated in

2020 (25). Unfortunately, despite the tremendous scientific efforts, PDAC remains the cancer with the worst prognosis i.e., a 5-year survival rate of 9% for all the stages combined. Moreover, this dismal prognosis is further decreased to 3% for the patients diagnosed with advanced disease. Improvement in PDAC 5-year survival has not been significant compared to the top five cancer types (**Figure 1.2c**) (24). Further, the PDAC burden is projected to increase in the next decade and is anticipated to be the second-leading cause of cancer-related deaths by 2030 (23). Despite progress in our understanding of cancer biology, oncology research, drug development, and novel therapeutic strategies, pancreatic cancer still remains one of the most challenging cancers to treat. Therefore, developing reliable methods for early diagnosis of PDAC and improved therapeutic strategies can have a significant impact on the clinical outcome for this deadly disease.

1.2.1 Molecular pathogenesis of PDAC.

PDAC is distinguished by four genes that are altered in a high fraction of patients, including KRAS (>90%), CDKN2A (>95%), p53 (50-75%), and DPC4/SMAD4 (55%) (26). PDAC progresses through a series of precursor lesions, which include pancreatic intraepithelial neoplasia (PanIN), intraductal papillary mucinous neoplasia (IPMN), and mucinous cystic neoplasia (MCN). PanIN lesions are the most prevalent type of preinvasive lesions, which arise from small pancreatic ducts. They are morphologically classified into four grades, PanIN 1A, PanIN 1B, PanIN 2 and PanIN 3, where PanIN 3 is referred to as carcinoma *in-situ* before they give rise to invasive adenocarcinoma and metastasis (**Figure 1.3**) (27).
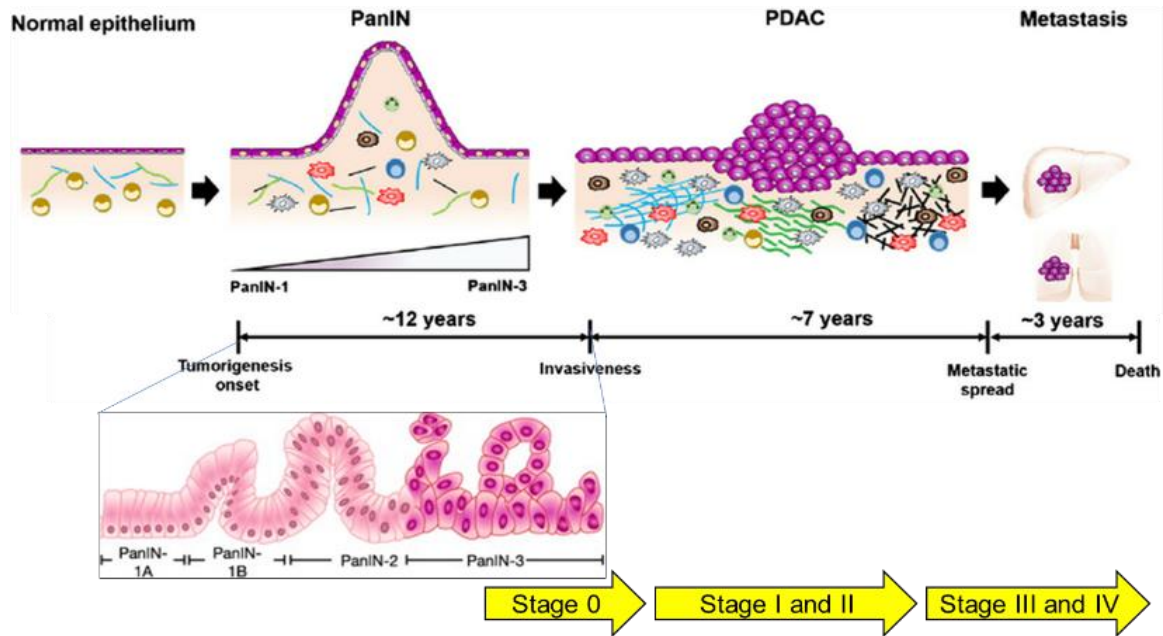
Figure 1.3. Molecular pathology of PDAC. Estimated time required for the progression of PDAC from PanIN precursor stage to invasive carcinoma and metastasis (27).

1.2.2 Major causes of the poor prognosis in PDAC.

The high mortality rate and poor prognosis of PDAC can be attributed to multifactorial reasons including (28, 29):

a. **Lack of early diagnosis**: PDAC is asymptomatic at the early stages of the disease. Signs and symptoms in PDAC such as abdominal pain, yellow skin and eyes, and weight loss occur only at the late stages (22). There are no reliable biomarkers for effective screening tests. In addition, the positioning of the pancreas towards the back of the abdomen is anatomically unfavorable for bioimaging. These factors result in less than 20% of patients diagnosed at early stages who may be eligible for the potentially curative surgical option (30).

b. **High metastatic burden**: More than half of PDAC patients at diagnosis, present with locally advanced or metastatic disease with the main metastatic sites being liver, lungs, and peritoneum (31). The metastatic propensity is rapidly acquired during

carcinogenesis, and the metastatic spread in PDAC is seen even when primary tumors are as small as 2 cm. The pancreas is situated in the abdominal region at the junction of several vital organs including the stomach, liver, and diaphragm. The early invasion of cancer cells to nearby blood vessels is due to the high vascular and lymphatic connections between the pancreas and the surrounding organs (32).

c. **Inherent and acquired resistance to systemic therapies**: PDAC exhibits extremely efficient pre-existing and acquired resistance to various therapies like chemotherapy, radiotherapy, and immunotherapy. The resistance is a result of genetic heterogeneity, aberrant signaling of carcinogenic pathways, and altered metabolism. These factors lead to cellular clones in tumors that respond differently to treatments, exhibit different metastatic potential, and contribute to recurrence. With the recent understanding of genetic and transcriptome analysis of PDAC tumors, it was proved that epigenetics and abnormal production of miRNA (micro RNA) and lncRNA (long non-coding RNA) contribute heavily to the resistance in PDAC (33). It is essential to point out that TME in PDAC acts as a physical barrier for systemic drugs and is an active contributor of resistance to therapies (34).

d. **Abundant desmoplastic stroma**: PDAC exhibits a unique desmoplastic stroma, which can account for up to 80-90% of the tumor volume. PDAC stroma is composed of cellular and acellular components, including pancreatic stellate cells (PSCs), cancer-associated fibroblasts (CAFs), immune cells, and excessive extracellular matrix (ECM). Stroma is responsible for hypovascularized and hypoxic tumors. The high desmoplastic stroma results in poor perfusion of systemic drugs and acts as a physical barrier for drug delivery. Moreover, the stroma-tumor crosstalk builds a

unique tumor microenvironment (TME) that accelerates tumor progression, immune suppression, and metastasis (35).

1.3 Current clinical approaches for PDAC treatment.

Complete surgical resection remains the only potentially curative treatment for PDAC. However, only less than 20% of newly diagnosed patients are suitable for surgery at the time of diagnosis. Unfortunately, more than 70% of diagnosed patients present with advanced disease and metastasis, which preclude curative surgical resection (36). Therefore, systemic therapies such as chemotherapy and radiation therapy are the mainstay for PDAC in the clinic.

1.3.1 Gemcitabine and limitations associated with gemcitabine monotherapy.

Gemcitabine (Gem) has been the cornerstone for PDAC chemotherapy since its approval in 1997 (37). Gem (2',2'-difluoro 2'-deoxycytidine, dFdC) is a deoxycytidine analog, which is transported into cells via nucleoside transporters (NTs) like ENTs and CNTs (38). Once taken up by the cells, Gem is phosphorylated by the intracellular enzyme (dCK) to produce dFdCMP, which is further converted to its active diphosphate form (dFdCTP). The active form dFdCTP is incorporated in the DNA leading to DNA polymerase dislodgement from the DNA strand, specifically one nucleotide downstream. The masking of the extra nucleotide makes the break site unattractive to DNA repair enzymes that lead to cell apoptosis (39). Though potent, drawbacks in Gem therapy lead to modest overall effect; median survival of 5.6 months, 23.8% response rate (40). Understanding and addressing intrinsic and extrinsic limitations in Gem monotherapy is essential to improve the therapeutic index of Gem (**Figure 1.4**). These limitations are explained in detail below:

a. <u>**Inefficient Gem delivery**</u>: Gem is deactivated in the blood and TME by enzyme-mediated deamination. Cytidine deaminase (CDA) is the critical enzyme responsible for Gem deactivation. This limits the circulation of Gem and leads to its short plasma half-life (41). Further, the desmoplastic stroma in PDAC tumors behaves as a physical barrier for Gem delivery (**Figure 1.4a**). All these factors contribute to reduced tumor accumulation of Gem in the tumors and cancer cells.

b. <u>**Cellular transport of Gem**</u>: Cellular uptake of Gem acts as the crucial next step in the Gem cytotoxicity and resistance. The nucleoside transporter (ENTs and CNTs) serves as a major limiting factor, and decreased expression of nucleoside transporters is reported as a mechanism of resistance (42).

c. <u>**Intracellular Gem processing**</u>: The intracellular processing of Gem by dCK enzyme in cells is a rate-limiting step for the conversion of Gem into its active metabolite (dFdCTP). The acquired and intrinsic deficiency of dCK in PDAC cells is related to the resistance of Gem (43).

d. <u>**Intracellular deactivation of Gem**</u>: Further intracellular Gem deactivation by CDA results in the inactive Gem metabolite (dFdU), which is excreted out from the cells. The overexpression of CDA in cancer cells plays a vital role in Gem resistance (**Figure 1.4b**) (34).

e. <u>**Enzymes potentiating Gem cytotoxicity**</u>: Ribonucleotide reductase (RR) is important for maintaining the deoxynucleotide (dNTP) pool in the cell. Hence, decreased activity of RR potentiates the incorporation of Gem in the DNA and increases the effectiveness of the drug by decreasing the competition between Gem and deoxycytidine. While Gem self-potentiates its effect by directly inhibiting the RR

subunit M1 (RRM1), the upregulation of the RR enzyme can confer resistance (44).

f. **Increased off-target toxicity**: Gem deactivation leading to the short half-life, and insufficient Gem concentrations in the tumor tissue requires high dosage administration in order to increase the therapeutic dose. This leads to high systemic toxicities in healthy tissues (45).
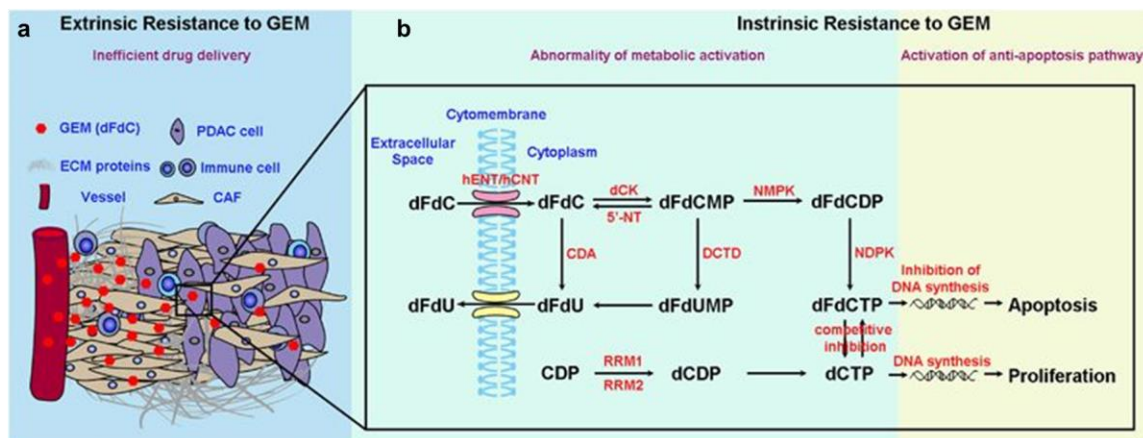
Figure 1.4. Complex intrinsic and extrinsic mechanisms of Gem resistance. **(a)** Extrinsic resistance of Gem is related to inefficient drug delivery in the tumor cells due to plasma inactivation of Gem and desmoplastic stroma. **(b)** Intrinsic resistance is related to cellular transport, intracellular metabolism, and intracellular inactivation of Gem (34).

1.3.2 Combination therapies approved in the clinic.

The improvement of Gem therapy is an essential goal in the treatment of PDAC. As a promising option, combination therapies have been investigated in research and clinical settings (46). The most common strategy is to enhance the cytotoxic effect of Gem by exploiting its combination with other chemotherapeutic drugs. For example, numerous studies evaluated the addition of chemotherapeutic agents like 5-fluorouracil (5-FU), capecitabine, oxaliplatin, and cisplatin to the Gem regimen. Unfortunately, these studies failed to show improvements in survival compared to Gem monotherapy (46). Recent combinations like Gem plus nab-paclitaxel or FOLFIRINOX have brought back the excitement in combination therapies to improve prognosis in PDAC.

The combination of Gem with nab-paclitaxel, an albumin-bound nanoparticle formulation of paclitaxel, resulted in a 2-month survival benefit compared to Gem monotherapy. The Gem plus nab-paclitaxel regimen exhibited improved response rate (RR) (23% vs. 7%), prolonged median progression-free survival (mPFS) (5.5 vs. 3.7 months), and prolonged overall survival (OS) (8.5 vs 6.7 months) compared to Gem monotherapy (47). The role of nab-paclitaxel in the treatment regimen presumably is associated with increasing the tumor delivery of Gem, modulation of stroma, and synergistic performance with and Gem (48). This improvement led to the FDA approval of Gem plus nab-paclitaxel as the standard front-line therapy for PDAC in 2013. Nevertheless, this regimen is associated with some adverse effects including neutropenia, fatigue, peripheral neuropathy, and alopecia (46).

FOLFIRINOX regimen, which includes folinic acid, 5-FU, irinotecan, and oxaliplatin, resulted in an OS (11.1 months vs 6.8 months), mPFS (6.4 months vs 3.3 months) and objective RR (31.6% vs 9.4%) compared to Gem monotherapy (49). Although FOLFIRINOX showed superior activity, the regimen is reserved for patients with good performance status due to its increased toxicity. The adverse effects of FOLFIRINOX include fatigue, bone marrow suppression, neutropenia, diarrhea, and sensory neuropathy. To reduce these side effects, a modified regimen of FOLFIRINOX, which includes reduced doses of irinotecan and bolus 5-FU or omission of bolus 5-FU (50). Currently, the clinical choice of FOLFIRINOX vs Gem plus nab-paclitaxel as front-line therapy is based on the physician choice and the performance of the patients.

Second-line chemotherapy for PDAC is designed when the disease continues to progress even after first-line therapy. The choice of second-line regimen is contingent on

the first-line regimen used: if the patient was treated with a Gem-based approach, then a 5-FU-based therapy is typically utilized as second-line and vice versa. A combination of nanoliposomal irinotecan and 5-FU showed improved outcomes compared to 5-FU alone (6.1 months vs 4.2 months), which lead to the regimen approval by the FDA in 2015 (51).

Another combination therapy approach investigates the molecular targeted therapies based on the genetic or phenotypic characteristics of PDAC (52). In this approach of combining targeted molecular therapies to chemo-agents, a marginal benefit was observed for Gem plus erlotinib. Erlotinib is an epidermal growth factor receptor (EGFR) tyrosine kinase inhibitor, which prolonged median overall survival by 10 days when added to Gem (6.24 months vs 5.91 months) (53). This combination was approved by the FDA in 2007 for marginal improvement. However, this regimen is not widely used in the clinical practice due to the limited clinical utility, increased toxicity, and high cost (46).

1.4 Novel approaches currently explored in clinical trials for PDAC.

The current clinical investigation for PDAC therapies can be organized into three main approaches: 1) combination therapies involving multiple chemo-agents, 3) targeted molecular agents, and 3) TME modifying agents. As mentioned in the previous sections, current front-line therapies include Gem alone, Gem plus nab-paclitaxel, and FOLFIRINOX. Hence, these act as the backbone drugs to which additional experimental drugs are added under various clinical trials (46).

1.4.1 Combination therapies based on chemotherapy agents

With the success of two- and three-drug combinations, there has been a growing interest in utilizing more aggressive regimens to increase cytotoxicity and improve

tolerability. Recent trials include the addition of chemo-agents like cisplatin and capecitabine to current therapies. Results of a phase Ib/II pilot trial evaluating the addition of cisplatin to Gem plus nab-paclitaxel regimen reported a high RR (complete response 8.3%; partial response 62.5%; stable disease 16.7%; progressive disease 12.5%), albeit at the expense of high toxicity profile (54). Another cytotoxic combination involved the addition of cisplatin and capecitabine to Gem plus nab-paclitaxel (4-drug regimen), which showed a PFS at 6 months of 100% in the combination arm versus 61% in the control arm (55). This regimen is further being tested under metastatic settings (NCT01730222) (37). The aforementioned regimens are under discussion for evaluation in phase III clinical trials. Overall, multi-drug therapies exhibit significant improvement in the PDAC prognosis. Nevertheless, these combinations are associated with high toxicity profiles. Therefore, developing safe delivery systems becomes a critical factor in exploiting the full potential of multi-drug combinations.

1.4.2 Combination therapies based on targeted molecular agents.

PDAC has high genomic heterogeneity in terms of mutational landscape. Hence, genetic and molecular pathway alterations have shaped the development of novel PDAC therapies (56).

a. It is well established that the KRAS mutation is the driver mutation in PDAC, as demonstrated by the fact that over 90% of the PDAC tumor harbor the KRAS mutation (57). KRAS mediates signal transduction between membrane growth factor receptors and downstream pathways, such as MEK, PI3K/AKT, and ERK. All these signaling pathways contribute to tumor growth, progression, and metastasis. Due to its importance, various clinical trials are focused on targeting KRAS and the

downstream effectors (37).

b. Certain cell surface receptors are overexpressed and play an essential role in PDAC tumorigenesis. These receptors are extensively studied as therapeutic target including EGFR, human epidermal growth factor receptor 2 (HER2), and vascular endothelial growth factor receptor (VEGFR) (58).

c. At least 10% of the PDAC disease is associated with genetic predisposition. About half of these germline mutations occur in DNA damage repair-related genes. Hence, molecules that inhibit DNA repair in combination with DNA damaging chemo-agents, such as PARP inhibitors combined with Pt-based drugs, are investigated as a promising strategy (59).

d. Therapies targeting epigenetic and metabolic changes are also highly investigated in PDAC. Epigenetic changes in the DNA including miRNA, lncRNA are now thought to be a target in the PDAC therapy. High desmoplastic stroma and hypoxic tumors have shown to reprogram the tumor cells metabolically to sustain unrestricted tumor growth. This gives an opportunity to explore metabolic inhibitors as potential therapeutic strategies (60).
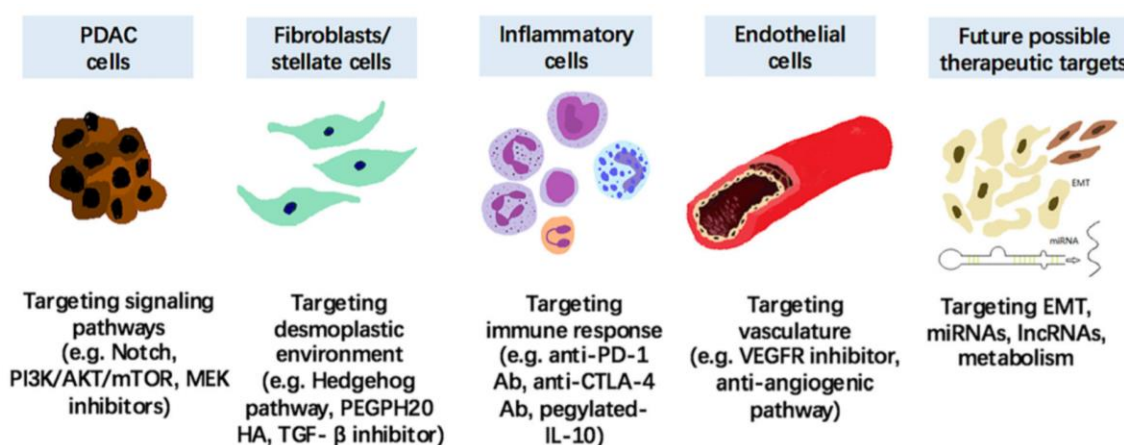
Figure 1.5. Novel therapies targeting various elements of PDAC tumors. Therapies targeting signaling pathways participating in tumorigenesis, the components of tumor microenvironment,

immune responses, tumor vasculature, novel epigenetic changes, and metabolic changes in PDAC (58).

1.4.3 Therapies modulating the components of TME.

PDAC is a highly desmoplastic tumor where the crosstalk between the cancer cells and components in the TME drives the tumor progression, invasion, and metastasis. As each of the TME components has a specific role in tumor growth, these components are considered to be potential therapeutic targets. The stromal ECM components including collagen, hyaluronan (HA), metalloproteinases (MMP), and other soluble cytokines and growth factors have been the early targets to disrupt stroma in order to increase the drug delivery and decrease resistance (29). One of the most recent approaches in this direction is the enzymatic depletion of HA using PEGylated recombinant hyaluronidase (PEGPH20) (61). A combination of PEGPH20 with chemotherapy improved progression-free survival of advanced PDAC patients in clinical trials. This combination is currently under advanced phases of clinical evaluation with selected PDAC patients pre-screened for increased HA levels in the tumors (58, 62). Other molecular agents including MMP, connective tissue growth factor (CTGF), CXC chemokines, and angiotensin inhibitors have been investigated in pre-clinical settings with improved outcomes and need further clinical validation (29). These targets are noncellular ECM components, which result in disruption of ECM, leading to a reduction in the interstitial fluid pressure (IFP), allowing for increased perfusion of systemic drugs in the tumors.

Remodeling or reprogramming the tumor stroma to induce quiescence rather than stromal depletion is the current focus based on the evidence of catastrophic results of excessive stromal disruption (62). In parallel, the importance of pancreatic CSCs in the

formation and maintenance of the TME has highlighted the deactivation of PSCs as a potential target for reshaping TME in PDAC. Therapies to induce cancer-associated fibroblasts (CAFs) and PSCs quiescence are currently investigated including treatment with vitamin A and D analogs (63). These therapies have shown potential in pre-clinical models including genetically engineered mice (GEM) models warranting the ongoing clinical trials (62).

An alternate direction is to intervene on the molecular pathways involved in the crosstalk between the various TME components. These pathways include the TGF-β and sonic hedgehog pathways (58, 64) (**Figure 1.5**). The role of the Hedgehog pathway in PDAC and the corresponding therapies which is a major topic in this thesis, are discussed in detail in section 3.1.2. Moreover, other TME components like immune cells and pancreatic CSCs have been recently investigated as novel therapeutic targets for the treatment of PDAC (58, 65, 66).

1.5 Use of nanoparticles for PDAC treatment.

Nanotechnology has evolved to the forefront in the areas of medical diagnostics, imaging, and therapeutic drug delivery. Nanomaterials are applied in a plethora of scientific areas by virtue of their unique properties associated with the nanoscale, such as surface area and quantum effect (67). Nanomedicine brings nanotechnology and medicine together to improve current diagnosis and treatment as an effective solution to address some of the critical issues associated with cancer. Nanomaterials such as liposomes, albumin-based nanoparticles, polymeric nanoparticles, micelles, gold, and silica nanoparticles have been extensively used to develop novel imaging probes and therapies to improve cancer treatment (68-70). The applications of nanomedicine have

made their way to the benefit of cancer patients with products like Doxil, Abraxane, and MM-398; additionally, many other platforms are under clinical investigation (71, 72).

The rationale design of nanocarriers for the anticancer drug delivery has resulted in increased plasma half-life, improved pharmacodynamic and pharmacokinetic properties of drugs, target-specific drug delivery via passive or active targeting, and decreased off-target toxicity (73-75). As previously mentioned, the leaky vasculature and poor lymphatic drainage in tumors allow nanoparticles to accumulate within tumors (EPR effect). The nanoparticles are large enough to escape filtration by the kidneys yet small enough to evade phagocytic removal by Kupffer cells and splenocytes in the mononuclear phagocyte system (MPS). In conjunction, nanoparticles can actively target tumor tissue with the use of targeting moieties. Active targeting is advantageous, specifically in tumors where the EPR effect is diminished (76). The nanoparticles between 1 and 500 nm provide the inherent property to interact with the cell surface and organelles. Several nanomaterials have been investigated for early detection of PDAC (77-79) as well as the development of PDAC therapies, including chemo, gene, photodynamic, and photothermal therapies (68, 80-83).

1.5.1 Nanoparticles designed for safe delivery of single chemotherapy agents.

The primary chemotherapy agent for PDAC treatment (Gem) as currently administered has multiple limitations and thus, maybe substantially improved. Nanomaterials have proven to increase the overall intracellular Gem concentration via improved pharmacokinetics, decreased the metabolic deactivation, and to overcome Gem resistance.

As discussed in the previous sections, the primary limitation in the efficacy of

Gem is its rapid deactivation and elimination from the body. Nanoparticles have been used to overcome the rapid metabolization and drug resistance associated with Gem. Cosco et al. demonstrated the increased delivery of Gem to tumor tissue using Gem-loaded PEGylated liposomes (L-Gem). L-Gem increased the systemic availability of Gem, where the plasma half-life was increased to 8 h using L-Gem compared to 1.5 h for free Gem. This resulted in the longer circulation of L-Gem and enhanced antitumor activity against PDAC tumor-bearing mice as compared to free Gem (84). In addition, Wonganan et al. and Zhu et al. demonstrated that Gem prodrug (Gem C18) loaded nanoparticles had superior performance compared to the free Gem in Gem-resistant cells that are deficient in hENT1 or dCK while overexpressing RRM1 (section 1.3.1). These studies showed that nanoparticles could deliver increased Gem concentrations in cells, independent of the nucleotide transporter expression. The prodrug form of Gem can overcome the deactivation by CDA, intracellularly converted into Gem active metabolite, and interact efficiently with the increased RRM1 in resistant cells (85, 86).

Similar nanoformulations have been investigated using various Gem prodrugs. For example, the chemical linkage of squalene at the 4-amino position of Gem (SQ-Gem) has been shown to inhibit its deamination by CDA (87). This prodrug has been used to form self-assembled nanoparticles, which decreased the Gem deactivation while increasing Gem half-life and intracellular Gem concentrations. The controlled release of Gem from nanoparticles reduced the rapid saturation of intracellular enzymes required for potentiating the Gem cytotoxicity (section 1.3.1d). This further prevents acquired Gem resistance in cells (88). Other nano-formulations like polymeric micelles have been used to deliver Gem (P-Gem) with improved plasma stability and sustained drug release

by incorporating chemical linkages between Gem and polymer forming the micelles. The P-Gem micelles successfully inhibited tumor growth in PDAC tumor-bearing mice (89, 90).

1.5.2 Nanoparticles designed for multi-drug or combination drug delivery.

Combination therapies involving the addition of multiple chemo-agents with Gem is the primary approach to increase Gem efficacy while decreasing resistance. One of the limitations with conventional combination therapy is that participating drugs have different physicochemical properties. This leading to differences in pharmacokinetics and pharmacodynamics and differential tumor accumulation of drugs. In addition, the full potential of combination therapies is limited by their increased adverse effects. Nanoparticles can alleviate these limitations by carrying multiple drugs in order to augment drug synergism by controlled spatiotemporal delivery while reducing side effects. Poon et al. reported a synergistic combination of Gem/oxaliplatin using nanoscale coordination polymer (NCP). This study used GMP (Gem monophosphate), which is formed after intracellular phosphorylation of Gem and is a rate-limiting step for Gem potency (section 1.3.1). Thus, using GMP bypasses this critical step to improve Gem efficacy. *In vivo* efficacy studies were carried out in PDAC subcutaneous xenograft mice. The results indicate that the co-delivery of GMP/oxaliplatin using NCP led to synergistic therapeutic effects and enhanced antitumor efficacy compared to their single drug counterparts (91). Similarly, Emamzadeh et al. reported the use of liposomes to deliver Gem and cisplatin, which can precisely manipulate and control the synergism of Gem/cisplatin. Also, the liposomes are coated with a thermosensitive polymer, which allows for stimuli-responsive drug release under temperature as an external stimuli. The

liposomes could co-deliver Gem/cisplatin with increased cytotoxicity in PDAC cells compared to single drug-loaded liposomes (92).

1.5.3 Nanoparticles designed for targeted drug delivery.

Effective cancer treatment demands that the administered drug efficiently reaches the tumor tissue by overcoming the barriers associated with blood circulation and tumor penetration. In general, nanoparticles access to the tumor site by passive or active targeting. Passive targeting is facilitated by the inherent nanometer scale, which takes advantage of the leaky tumor vasculature. Indeed, the neo-vasculature in tumors is characterized by gaps between the adjacent endothelial cells resulting in a leaky and defective architecture of the blood vessels. It is accompanied by poor lymphatic drainage in the tumor. This feature of tumors gives rise to enhanced permeability and retention (EPR) effect (**Figure 1.6**). However, the EPR effect varies with tumor types and degree of tumor vascularization (76, 93).

The active targeting of nanoparticles relies on the nanoparticle functionalization with specific targeting moieties, which are selected based on high avidity and specificity to the cancer cell surface receptors. Various targeting ligands have been investigated, like monoclonal antibodies, aptamers, peptides, and antibody fragments (76). Targeted nanoparticles are internalized in the specific cells using receptor-mediated endocytosis (**Figure 1.6**). Hence, this approach offers increased nanoparticle tumor accumulation. The higher nanoparticle accumulation leads to increased drug delivery to tumors as well as decreased off-target toxicities.
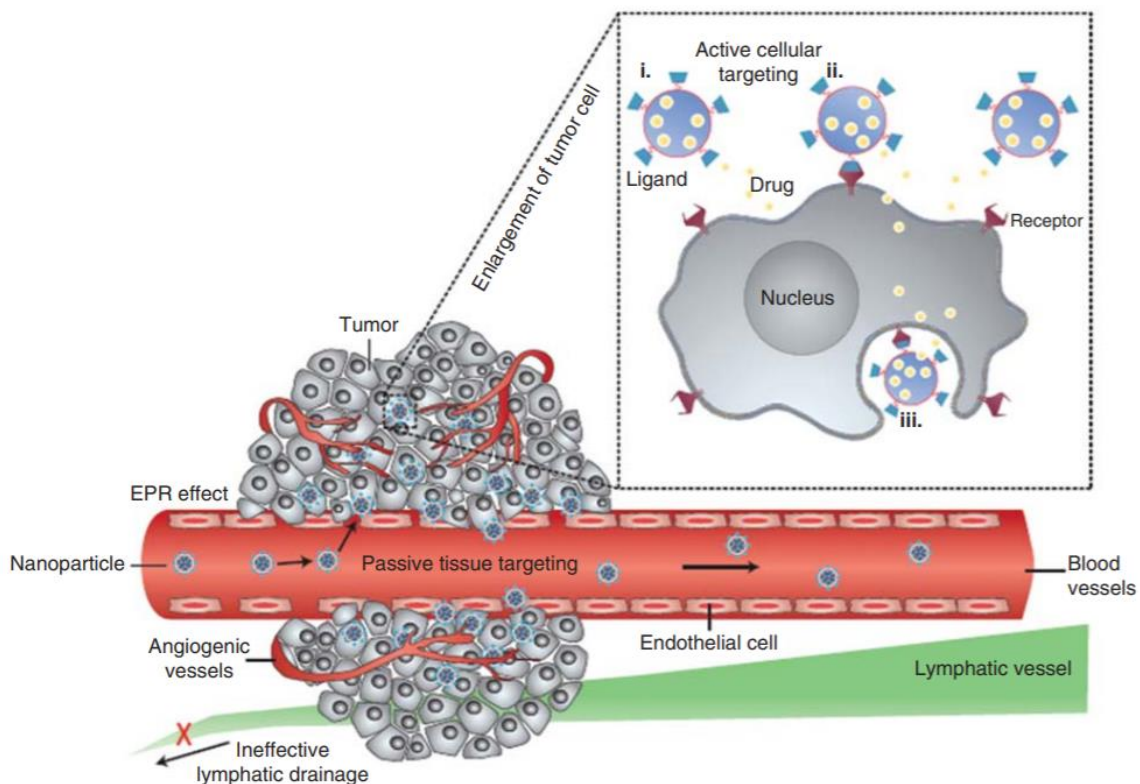
Figure 1.6. Passive and active targeting mechanism of nanoparticles. Passive targeting of nanoparticles is achieved via the EPR effect. The active targeting is accomplished via nanoparticle surface functionalization leading to increased binding of nanoparticles to specific target cells (93).

Overexpression of epidermal growth factor receptor (EGFR) is linked to various cancer types, including PDAC (94). Clinically, cetuximab is an anti-EGFR antibody used to inhibit EGFR signaling, and various studies have used this antibody for targeted drug delivery of gold, iron oxide, and polymeric nanoparticles (95). McDaid et al. reported cetuximab (CTX) functionalized polymeric nanoparticles designed to deliver the anticancer drug, camptothecin (CPT). The therapeutic effectiveness of targeted nanoparticles was validated *in vitro* and *in vivo*. CTX-nanoconjugation improved the targeting of nanoparticles and enhanced CPT-induced apoptosis of PDAC cells. *In vivo* experiments with PDAC tumor-bearing mice showed that targeted nanoparticles could effectively target the cancer cells and increase tumor inhibition (96). In addition,

cetuximab-conjugated gold nanoparticles (AuNPs) were investigated for the delivery of Gem. The therapeutic efficacy of the targeted delivery system exhibited significant inhibition of pancreatic cancer cell proliferation *in vitro* and inhibited the orthotopic pancreatic tumor growth *in vivo*. Pharmacokinetic experiments, along with the quantification of Au both *in vitro* and *in vivo,* further confirmed that the inhibition of tumor growth was due to enhanced targeted delivery (97).

Mondal et al. also reported the use of polymeric micelles decorated with cetuximab. The micelles were used to deliver Gem and miR-205, which is involved in Gem resistance. Systemic administration of the targeted micelles exhibited significant tumor growth inhibition in orthotopic pancreatic tumor-bearing mice compared to untargeted micelles (98). Another receptor investigated for targeted delivery is urokinase plasminogen activator receptor (uPAR), which is overexpressed in pancreatic cancer cells. Lee et al. engineered uPAR-targeted magnetic iron oxide nanoparticles (IONPs) carrying Gem for targeted delivery. These theranostic nanoparticles enable the intracellular release of Gem following receptor-mediated endocytosis into tumor cells and, also provide contrast enhancement in magnetic resonance imaging (MRI) of tumors. Systemic administration of uPAR-IONPs significantly inhibited the growth of orthotopic PDAC tumors and allowed for the detection of residual tumors (99).

1.5.4 Nanoparticles designed for tumor stroma modulation therapy.

The unique microenvironment in PDAC is a cardinal histopathological feature where the stroma comprises up to 80% of the tumor mass, rendering most of the systemic treatments ineffective. Excessive ECM generates high interstitial fluid pressure resulting in compressed blood vessels causing hypoperfusion, hypovascularity, and hypoxia. In

addition, the dense stroma compromises on the performance of the nanomedicine, hindering the penetration and extravasation of nanoparticles in the tumors and off-target toxicity in the stromal components. To elevate therapeutic effectiveness, combination therapies targeting different stromal barriers and tumor-stroma crosstalk pathways are being investigated. Various advanced drug delivery carriers have been tested to overcome the stroma barrier in different ways to increase the nanoparticle therapeutic efficacy against PDAC (100, 101).

Mardhian et al. reported the use of nano-targeted relaxin to modify stroma and increase the efficacy of Gem. Relaxin is an anti-fibrotic agent that inhibits the activation of PSCs. In this study, relaxin was delivered using superparamagnetic iron oxide nanoparticles (SPIONs) to overcome the drawbacks of relaxin delivery, such as rapid degradation and short circulation. Administration of relaxin-SPIONs into tumor-bearing mice reduced the activation of PSCs, as indicated by decreased fibrosis, reduced ECM deposition. When co-administered with Gem, relaxin-SPIONs potentiated the effect of Gem. This can be attributed to reduced collagen deposition, allowing better drug penetration in tumors (102). PSCs are also known to support metastasis in PDAC. Another study by Mengying et al. investigated the role of relaxin-loaded lipid nanoparticles for targeting the liver metastasis of pancreatic cancer. Relaxin reversed the stromal microenvironment, which makes it unfavorable for established liver metastasis to grow, resulting in significant inhibition of metastatic progression and prolonged survival (103).

The studies described above focused on using nanoparticle-based delivery systems to carry a TME modulating agent, co-administered with free chemotherapy

agents. Other reports demonstrated the use of nanoparticles for co-delivery of a TME modulating agent and a chemotherapy agent. Zhao et al. reported the co-delivery of cyclopamine (CPA, sonic hedgehog inhibitor) and paclitaxel (PTX) using polymeric micelles (M-CPA/PTX). The low dose of CPA and co-delivery of PTX resulted in stromal modulation, decreased ECM, and alleviated hypoxia while maintaining the tumor-restraining function of the stroma. The M-CPA/PTX nanoparticle therapy resulted in extend animal survival by suppressing tumor growth. This study used multifunctional nanoparticles to simultaneously target cancer cells and stromal components (85).

1.6 Mesoporous silica nanoparticles.

1.6.1 Introduction to mesoporous silica nanoparticles.

Among the various nanomaterials, mesoporous silica nanoparticles (MSNs) have attracted considerable interest in different fields of science and engineering due to their unique properties. MSNs offer several unique and advantageous properties such as chemical and thermal stability, high surface area, tunable particle size and pore diameter, chemically modifiable surfaces, and facile functionalization (104). MSNs have been used for a wide variety of applications including, catalysis, food manufacturing, biosensing, delivery of drugs, and contrast agents (105-108). MSNs exhibit several advantages, which make them an excellent candidate for biomedical applications (**Figure 1.7**) (109-111). These factors are explained in detail below:

a. **High drug loading capacity**: MSNs' high surface area and ordered porous structure allows for high drug loading. Drugs can be encapsulated in the internal surface and/or conjugated to the external MSN surface.

b. **Multifunctionality**: The silanol-containing MSN surfaces can be functionalized with high selectivity to achieve better control over drug loading and release. Moreover, the external surface can be conjugated with various targeting/imaging agents and stimuli-responsive molecules for efficient cell-specific drug delivery (112).

c. **Biocompatibility**: Silica is "Generally Recognized as Safe" material by the United States FDA. Recently, Cornell dots (C dots), another class of silica nanoparticle have been approved for stage I/II human clinical trial for targeted molecular imaging (113). Various *in vivo* preclinical evaluations have established that MSNs are biocompatible. In addition, the biodistribution, passive targeting, and the clearance of MSNs can be tuned by modifying their key structural parameters, such as particle size, morphology, porosity, surface properties, functionalization, and administration routes.

d. **Stimuli-responsiveness**. MSN surface can be modified with macrocycle molecules, polymers, and proteins, which act as capping agents or pore gating agents. Another approach for controlled drug release is to use stimuli-responsive chemical handles to conjugate drugs to MSNs. These chemical linkages can prevent the premature release of drugs in the systemic circulation, whereas once in the target tissue (tumor), the chemical linkages break in response to the stimuli (114).
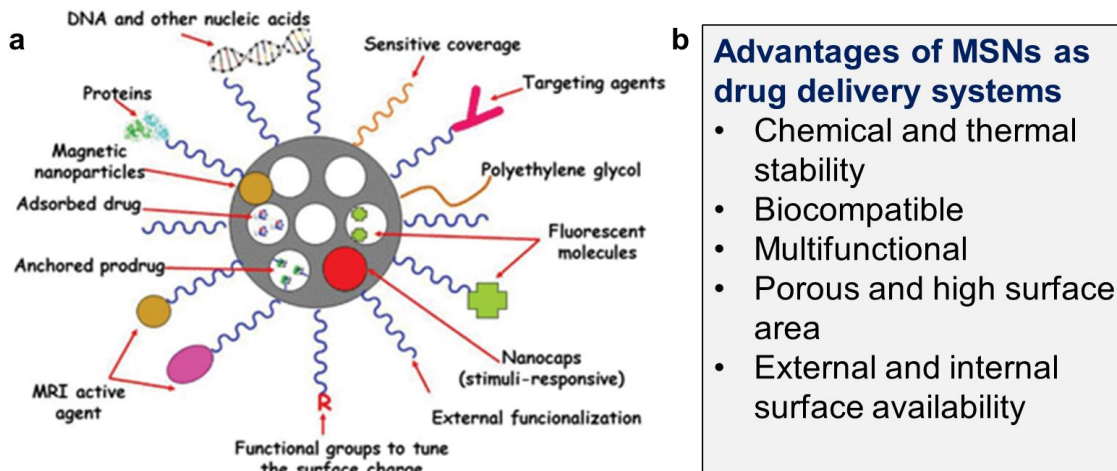
Figure 1.7. Advantages of mesoporous silica nanoparticle as drug delivery systems (115).

1.6.2 Synthesis and functionalization of MSNs.

1.6.2.1 Synthesis of MSNs.

The Stöber process is one of the most widely employed methods for silica nanoparticles. This method enables a high control over the polymerization and reaction kinetics leading to a wide variety of silica-based nanomaterials like solid, mesoporous, or hollow. The surfactant-template approach is a variation of the Stöber method used for the fabrication of MSNs. In this approach, a surfactant like cetyltrimethylammonium bromide (CTAB) is utilized, where the surfactant self-assemble into micelles at a concentration higher than the critical micellar concentration (CMC) (116). Upon the reaction conditions, this process leads to the formation of a liquid crystal, which acts as a template for the formation of a porous structure in MSNs (**Figure 1.8a**). Once the surfactant template is formed, the addition of silica precursor (tetraethyl orthosilicate, TEOS) condenses around the micellar template. The pH of the reaction solution controls the hydrolysis/condensation rates, which plays a major role in the polymerization of silica (117). Finally, the template surfactant can be removed either by calcination or by solvent

extraction to generate a highly ordered porous structure, as observed in the TEM image (**Figure 1.8b**).
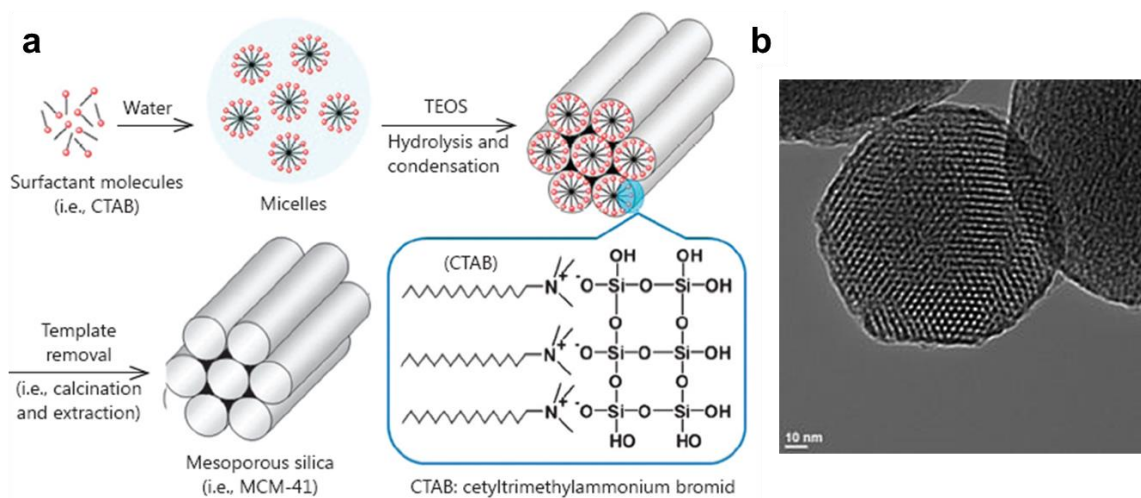
Figure 1.8. Synthesis of MSNs. **(a)** Schematic representation of the fabrication of mesoporous silica nanoparticles. **(b)** TEM image depicting the ordered porous structure of MSNs (117).

1.6.2.2 Functionalization of MSNs.

The functionalization of MSNs can be carried out through two main approaches: post-synthesis grating or co-condensation. In the post-synthesis grafting method, the organosilanes (example: aminopropyl triethoxysilane, mercaptopropyl trimethoxysilane) react with the silanol groups on the surface of the MSNs. The post-synthesis grafting can be carried out before or after surfactant template extraction. This reaction process is specifically advantageous to functionalize the exterior surface of the MSNs. In the co-condensation method, the organosilanes are introduced at the time of silica framework formation. This approach is advantageous to functionalize the interior surface of MSNs (**Figure 1.9**). One of the outstanding features of MSNs compared to other nanomaterials is the ability of multi-functionalization with high precision. As mentioned above, the interior or exterior surface of the MSNs can be selectively functionalized with different

functional groups. We have used this approach to functionalize the interior surface with pro-drugs and/or imaging agents and the external surface with other types of drugs and/or targeting moieties (118, 119).
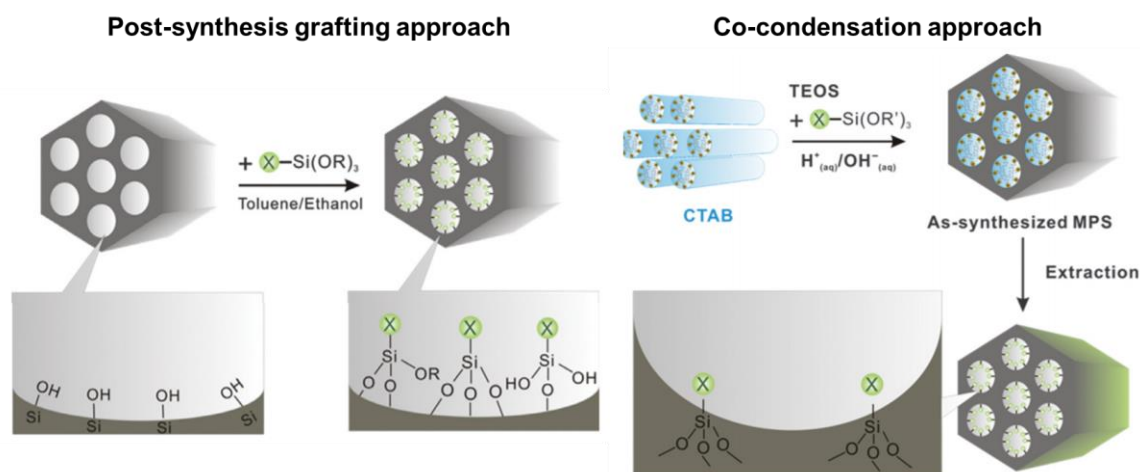
Figure 1.9. Main approaches for the functionalization of MSNs: post-synthesis grafting and co-condensation approach (119).

1.6.3 Use of MSNs for PDAC therapy.

Various studies have investigated the use of MSNs to develop different strategies for the detection and/or therapy of PDAC in cellular and preclinical settings. These approaches include the delivery of single chemotherapeutics (example: gemcitabine, doxorubicin, irinotecan) (120-122), the combination of chemotherapy agents and/or small molecule inhibitors (example: gemcitabine/paclitaxel) (120, 123, 124), and other therapeutic modalities (example: photodynamic therapy and photothermal therapy) (125, 126). In addition, novel target-specific MSN-based nanoprobes have also been developed for cancer imaging (127, 128). Overall, these studies demonstrate that MSN is a promising nanoplatform for the detection and/or treatment of PDAC.

a. **MSNs for increased delivery of single chemotherapy agents**: Irinotecan is an important component in the FOLFIRINOX regimen used for PDAC; however, it is

associated with increased toxicities (129). Liu et al. reported the use of lipid bilayer coated MSNs (LB-MSNs). The irinotecan was encapsulated in the MSN pores via proton gradient and the lipid bilayer further seals the pores. This approach resulted in the reduction of drug leakage, toxicity and improving the stability while increasing the drug concentration at the tumor site. The therapeutic efficiency of irinotecan loaded LB-MSNs in orthotopic PDAC mice showed a decrease in primary tumors as well as treating tumor metastases. This work demonstrated that the reduced leakage and controlled rate of irinotecan release due to the use of LB-MSNs dramatically decreased the systemic toxicity associated with irinotecan (120).

b. **Target-specific drug delivery**: c(RGCfE) is a peptide that shows high affinity to integrin ($\alpha_\gamma\beta_3$), which is overexpressed in the tumor blood vessels and cancer cells, including PDAC. Sun et al. developed c(RGDfE) conjugated multifunctional MSNs for the delivery of Gem. This target-specific MSN-based system includes a magnetic core for MRI imaging. The peptide conjugated nanoparticles increased the cellular uptake in human PDAC cells that overexpress integrin. Gem loaded MSNs resulted in efficient growth inhibition of PDAC cells (130).

c. **Combination therapy**: Meng et al. reported the use of lipid coated-mesoporous silica nanoparticle (MSNs) to co-deliver a synergistic combination of Gem and paclitaxel (PTX). The Gem drug was entrapped in the MSN pores, and the external surface of MSNs was subsequently sealed using a lipid bilayer (LB). The hydrophobic PTX was incorporated in the lipid bilayer in a ratiometric design. The Gem/PTX-loaded LB-MSNs were tested in mice carrying subcutaneous xenografts and the orthotopic model of PANC-1. The PTX/GEM-loaded LB-MSNs demonstrated effective

inhibition of primary tumor growth, as well as the elimination of metastasis. The authors demonstrated that the ratiometric co-delivery of PTX could suppress CDA expression resulting in increased concentration of active Gem in tumors compared to control groups (131).

d. **Combination therapy using MSNs for stroma remodeling**: Pericyte coverage of vascular fenestrations blocks the vascular access due to the dense stroma of PDAC, which also contributes as a barrier for nanoparticle delivery. In order to improve the vascular access and increase Gem delivery, Meng et al. developed a two-wave strategy to first decrease the pericyte coverage through interference in the TGF-β signaling pathway, followed by the delivery of Gem. The first-wave nanotherapy was accomplished using a polyethyleneimine (PEI)/polyethylene glycol (PEG)-coated MSNs to carry a small molecule TGF-β inhibitor, LY364947. The Gem was delivered using a PEGylated liposome as second-wave nanotherpay, which was administered sequentially after the administration of LY364947-carrying MSNs. This two-wave approach provided effective inhibition of the PDAC tumor in a xenograft model as compared with free drugs or Gem-loaded liposomes (132).

1.7 Preclinical models to evaluate PDAC treatment and/or diagnostic probes.

Preclinical models should reproduce critical features of PDAC disease and provide as an effective tool for developing strategies for early diagnosis, evaluating novel therapeutic drugs and nanomedicine (133). Human PDAC cell lines provide simple, low-cost, and easily replicable models with practical advantage for screening drugs. Nevertheless, they lack the complexity of PDAC tumors where various cells interact with each to guide the progression and growth of tumors. Therefore, clinically relevant *in vivo*

models within an increased level of complexity are being developed. These *in vivo* models include xenograft, orthotopic, patient-derived tumor xenograft (PDX), and genetically engineered mice (GEM) models (134). The simplest xenograft mice model involves the transplantation of human PDAC cells into immune-deficient mice. They are convenient, inexpensive and allow for rapid assessment of therapeutic safety and efficacy. Importantly, this model allows for easy assessment of tumor size (135).

Orthotopic mice models where the PDAC cells are transplanted in the pancreas is a more reminiscent model. Nevertheless, these models are costly, more difficult to discern the therapeutic response, due to the position of the pancreas. Xenograft and orthotopic mice models have predictive value, which helps to prioritize the biomarker selection, imaging, and/or therapeutic agents. However, cell line-based models lack genetic and phenotypic heterogeneity and hence, they limit the ability to predict the therapeutic responses in clinical settings (136). Human PDAC cell transplantation requires immune-deficient mice, which compromise the effect of immune system on the development of tumors and the effect of the immune system on the various aspects of therapeutic platform including nanoparticle circulation, tumor accumulation, and their performance. On the contrary, syngeneic transplant models are created by cancer cells derived from the same genetic strain. This model involves the use of immune-competent mice and tumor growth in the presence of a complete immune system (137).

Despite of the simplicity of the xenograft, syngeneic and orthotopic mice, models that recapitulate the progression of PDAC disease similar to that in humans are required for better understanding the disease and therapeutic studies of novel drugs and nanomaterials to obtain clinically relevant data. In this direction, genetically engineered

mice (GEM) models are created by introducing specific gene mutations in oncogenes and/or tumor suppressor genes that are important in human PDAC. GEM models have been recognized as more accurate predictors of drug response and better models for biomarker and therapeutic discovery (138).

PDAC arises from pancreatic ductal cells and progresses through a series of precursor lesions. Pancreatic intraductal neoplasia (PanIN) lesions are the most prevalent type of preinvasive lesions, which arise from small pancreatic ducts. They are morphologically classified into four grades, PanIN 1A, PanIN 1B, PanIN 2, and PanIN 3, where PanIN 3 is referred to as carcinoma *in-situ* and is characterized as stage 0 in humans before they give rise to invasive adenocarcinoma and metastasis (27, 139). Recently, the transgenic mouse model (KC or Cre-LSL-KRAS^{G12D}), which develops a full spectrum of PDAC, was developed and has been tested in various preclinical evaluations. Dr. Mukherjee has further crossed the KC mice with human tMUC1 (MUC1.Tg) mice and established a unique mouse model, PDA.MUC1 mice that expresses human tMUC1 in a tissue-specific manner and spontaneously develop pancreatic tumors (140-142). In this model, PanIN lesions develop from week 6-16, followed by adenocarcinoma by week 26 and invasive adenocarcinoma with metastases by week 36-40 after oncogenesis initiation (139, 143). PDA.MUC1 mouse is an ideal mouse model to evaluate the targeting and therapeutic capabilities of the MSN platform proposed in this Thesis to obtain clinically relevant outcomes.

1.8 Summary of the Thesis.

PDAC is one of the most devastating cancers with 5-year survival rate in single digits. Despite success in the genetic analysis, drug development, and novel therapeutic

strategies, PDAC still remains a challenging cancer to treat. Various factors are responsible for the poor prognosis of PDAC and investigations assessing combination therapies, addressing complex TME, and novel probes for bioimaging can benefit PDAC therapy. This thesis is focused on developing nanoparticle-based approaches to improve therapy and diagnosis in PDAC. Mesoporous silica nanoparticles (MSNs) are highly versatile nanocarriers and various applications of MSNs in the therapy and imaging of PDAC are presented in this Thesis.

Chapter 2 reports a target-specific combinatorial therapy using MSNs. The approach investigated consists of chemically conjugated gemcitabine and cisplatin prodrugs (Gem-cisPt-MSNs) at an optimized synergistic ratio that is released under the specific stimuli in the cancer cells. The MSN platform is further functionalized with a novel antibody (TAB004), which specifically recognizes tumor associated MUC1 (tMUC1). The chapter describes the synthesis and thorough characterization of the structural and chemical properties of the synthesized nanoparticles. Moreover, the *in vitro* evaluation of drug-conjugated MSNs including targeting ability, cytotoxicity, DNA damage, and apoptotic ability is also described to understand the detailed mechanism of our platform in PDAC cells. The study also illustrates preclinical investigation of our therapeutic MSN platform including safety, biodistribution, targeting ability, and therapeutic efficacy. Two mice models were used for this investigation, a syngeneic KCM model and a transgenic PDA.MUC1 model.

Next, chapter 3 reports on a sequential combination approach where Gem-cisPt-MSNs, described in chapter 2, are combined with a primary treatment that modulates tumor stroma. This chapter involves the design and synthesis of a tumor stroma

modifying agent (cyclopamine, CyP)-loaded MSN system. The chapter reports full structural and chemical characterization of the CyP-loaded MSNs. The *in vitro* evaluation of CyP-MSNs including cytotoxicity, and combination effect of CyP-MSNs plus Gem-cisPt-MSNs is described in PDAC cells. The preclinical *in vivo* evaluation of sequential combination of CyP-MSNs plus Gem-cisPt-MSNs is also illustrated in human PDAC HAPF II xenograft and PDA.MUC1 mice.

Chapter 4 presents a preliminary investigation of the potential use of TAB004-MSNs as a target-specific imaging probe for PDAC. The targeting ability and specificity of TAB004-MSNs was investigated in PDAC cells. The tumor targeting capability of TAB004-MSNs is reported in syngeneic KCM mice. We also investigated the bioimaging and early detection capacity of TAB004-MSNs in PDA.MUC1 mice.

Finally, Chapter 5 summarizes the main conclusions and contributions of this Thesis and describes future directions for the MSN-based platform for the therapy and imaging of PDAC.

CHAPTER 2: tMUC1-targeted combinatorial drug delivery using mesoporous silica nanoparticles for improved therapy of PDAC

2.1 Introduction

2.1.1 Gemcitabine-cisplatin combination for PDAC.

As mentioned in the previous chapter, Gem monotherapy suffers from drawbacks like Gem deactivation in the plasma and TME, development of intrinsic and extrinsic resistance by PDAC cells, and aberrant activation of molecular signaling pathways after prolonged exposure (144-146). To improve Gem efficacy, combination therapies have been investigated in preclinical and clinical settings (91, 124). Multiple chemo-agents including 5-FU, paclitaxel, oxaliplatin, and cisplatin (cisPt) have been added to Gem. The combination of cisPt and Gem therapy has been previously investigated for PDAC without significant improvements in the clinic. However, cisPt is currently investigated in combination with Gem plus nab-paclitaxel. One of the main drawbacks of cisPt-based therapies is their high off-target toxicity profile which further increases in combination therapies (147).

The synergistic benefit of the Gem/cisPt combination has been demonstrated in lung cancer and ovarian cancer (148-150). This effect is associated with the capacity of Gem to inhibit DNA repair of cisPt-induced DNA damage. Thereby, Gem potentiates the cytotoxic effect of cisPt. Nevertheless, the synergy between Gem/cisPt has not been thoroughly investigated in PDAC.

2.1.2 Mesoporous silica nanoparticles for the combinatorial delivery of Gem/cisPt.

Conventional combination therapies suffer from limitations of controlled spatiotemporal and ratiometric drug delivery due to the distinct physiochemical

properties of the participating drugs, different cellular uptake mechanisms, and increased off-target toxicities. Critically, exploiting the full potential of combination therapies requires the development of versatile delivery platforms that can simultaneously transport and release multiple drugs that exhibit different physicochemical properties (151-154). Nanocarriers provide a great opportunity in this direction for the improvement of combination therapies. MSN is a versatile delivery system that provides several unique advantages for the co-delivery of drugs. MSNs can encapsulate drugs at high capacity independent of the physicochemical properties of the drugs. Moreover, MSNs can be independently and selectively modified at interior and exterior surfaces for efficiently co-delivery of anticancer agents.

2.1.3 tMUC1 antibody for targeted drug delivery.

Active targeting mechanisms exploit and seek safe tumor homing through a target receptor that is specifically overexpressed in the cancer cells (76). Tumor-associated mucin1 (tMUC1) is a glycoprotein overexpressed in various human malignancies, including breast cancer and pancreatic cancer. tMUC1 differs from MUC1 expressed in normal cells, both in its biochemical features and its cellular distribution (155). Indeed, tMUC1 is ranked as second best target antigen among 75 tumor-associated antigens by NCI Translational Research Work Group (156). tMUC1 protein is detected in ~100% of PDAC tumors, making it an extremely valuable antigen for the targeted therapy for this disease (157, 158). tMUC1 is also associated with the poor prognosis, epithelial-mesenchymal transition (EMT), metastasis and chemoresistance in PDAC (155). TAB004 is a novel antibody developed by Dr. Mukherjee (UNC Charlotte) which recognizes an altered glycosylated epitope in the variable number tandem repeat (VNTR)

region of the extracellular segment of tMUC1 (159, 160). Importantly, TAB004 recognizes specific epitopes different from those recognized by other MUC1 antibodies and has unique complementary determinant regions (CDRs) of the heavy and light chains. TAB004 has been demonstrated to exhibit high specificity to tMUC1 in a spontaneous model of PDAC, and more relevant, in tumor samples from PDAC patients (158, 159).

2.1.4 Hypothesis and aims of the present study.

We hypothesized that a novel nanoparticle-based platform for the co-delivery of Gem and cisPt, with additional benefits of target-specific stimuli-responsive drug delivery can dramatically enhance the synergistic effect of Gem/cisPt, improve drug delivery to PDAC tumors and therapeutic efficacy, while reducing if not eliminating the of-target toxicities. To prove this hypothesis, we following aims are proposed:

a. Synthesis and characterization of TAB004-Gem-cisPt-MSNs.

b. In vitro evaluation of the synthesized MSN platform including targeting ability, cytotoxicity, DNA damage, and apoptotic ability is also described to understand the detailed mechanism of our platform in a panel of PDAC cells.

c. In vivo investigation of safety, biodistribution, targeting ability, and therapeutic efficacy of our therapeutic MSN platform in syngeneic KCM and transgenic PDA.MUC1 mice models.

2.2 Materials and Methods.

2.2.1 Materials.

Hexadecyltrimethylammoinum bromide (CTAB), Tetraethyl orthosilicate (TEOS), (3-aminopropyl)triethoxysilane (APTES), Diethanolamine (DEA), 3-

(Trihydroxylsilyl) propyl methylphosphonate monosodium salt (TPMP), poly(ethyleneimine) polymer (PEI; MW = 1.8kDa), N-succinimidyl-3-(2-pyridyldithio) propionate (SPDP), Gemcitabine hydrochloride, Cis-Diamineplatinum dichloride (Cisplatin), NIR-797-isothiocyanate, hydrogen peroxide (H_2O_2), O-(Benzotriazol-1-yl)-N,N,N',N'-tertamethyluronium tetrafluoro borate (TBTU), N,N-Diisopropylethylamine (DIPEA), 1- Ethyl-3-(3-dimethylaminopropyl) carbodiimide (EDC), Trifluoroacetic acid (TFA), succinic anhydride, S-trityl-mercaptopriopionic acid, triethylsilane (TEA), and Ninhydrin reagent were purchased from Sigma Aldrich. Methoxy polyethylene glycol N-hydroxysuccinimide (MeO-PEG-NHS; MW=2kDa) and MAL-PEG-SCM (MW=2 kDa) were purchased from Creative PEGWorks Inc. Sulfhydryl addition kit was purchased from Thermo scientific, Nano-W^{TM} (Nanoprobes), and TAB004 antibody was purchased from OncoTab.

Roswell Park Memorial Institute (RPMI 1640), fetal bovine serum (FBS), Dulbecco Modified Eagle Medium (DMEM), penicillin-streptomycin, phosphate buffer saline (PBS, 1X), and trypsin were purchased from Corning. Glutamax was purchased from Gibco and NEAA was purchased from Quality biologicals. Fetal bovine serum (FBS) was purchased from Atlanta Biologicals. CellTiter 96® AQueous Assay was obtained from Promega (Madison, WI, USA). BD Pharmingen™ Annexin V-FITC Apoptosis Detection Kit was purchased from BD Biosciences. Gamma H2A assay was purchased from Millipore Sigma. Buffered 10% Formalin purchased from VWR. *In situ* Apoptosis Detection Kit (ab206386) was purchased from Abcam Co LTD (USA).

A JEOL Transmission electron microscopy 2100 LaB6 was used for imaging nanoparticles. Malvern instrument Zetasizer Nano (red laser 633 nm) (Malvern

Instrument Ltd., Malvern, UK) was used for hydrodynamic size and zeta potential analysis. NOVA 2200e Quantachrome surface area and pore analyzer was used for MSN surface area and pore analysis. The IVIS® Spectrum imaging system (PerkinElmer) was used to determine the fluorescence of the nanoparticles for the *in vivo* studies. The excitation/emission was performed at 745/820 nm to image NIR dye. All tissue slides were visualized using an Olympus IX71 fluorescence microscope fitted with a DP70 camera and corresponding software (Olympus). CEM Mars microwave unit with Easyprep Teflon digestion vessels was used for the organ digestion. A PerkinElmer 8300 DV with autosampler inductively coupled plasma optical emission spectroscopy (ICP-OES) was used for the Si content analysis in the organs. A Thermo Electron X series inductively coupled plasma Mass spectroscopy (ICP-MS) was used for Pt content analysis.

2.2.2 Synthesis of cisPt and Gem prodrugs.

2.2.2.1 Synthesis and characterization of cisPt prodrug.

Cisplatin (IV) prodrug (disuccinotocisplatin) was synthesized via a two-step process following our previous procedure with slight modifications (161). The first step was the oxidation of cisplatin to afford dihydroxycisplatin. Briefly, cisplatin (200 mg, 0.67 mmol) was dissolved in nanopure water (9 mL, pH 7) followed by the addition of H_2O_2 (30 wt%, 1 mL). The mixture was allowed to react at 70 ºC under constant stirring for 5 h in nitrogen atmosphere in dark. The reaction mixture was cooled to room temperature and additionally stirred overnight at room temperature. The product was washed with ice-cold water and ethanol to afford dihydroxycisplatin **(1)**.

FT-IR (cm^{-1}): 3514 (O-H), 3261 (N-H)

The second step was the reaction of dihydroxycisplatin **(1)** with succinic anhydride to afford disuccinotocisplatin **(2)**. Dihydroxycisplatin (IV) (100 mg, 0.3 mmol) was dissolved in DMSO (4 mL). Succinic anhydride (120.4 mg, 1.2 mmol) was added to the solution and allowed to react for 24 h at 70 °C in dark. The product was dried under vacuum and washed with cold acetone to afford disuccinotocisplatin.

FT-IR (cm^{-1}): 3184 (O-H), 1736-1706 (C=O)

^{13}C NMR (300 MHz, DMSO-D$_6$, ppm): δ = 180.0 (**C**OOR), 174-172 (**C**OOH), 30.9 (CH$_2$**C**H$_2$COOH), 30.3 (**C**H$_2$COR). R= [PtCl$_2$(NH$_3$)$_2$]

2.2.2.2 Synthesis and characterization of Gem prodrug.

Gem prodrug **(4)** was synthesized following a two-step process reported in the literature with slight modifications (162). First, to synthesize 3-tritylthio-gemcitabine **(3)**, S-trityl-mercaptopropionic acid (136 mg, 0.4 mmol) and TBTU (143 mg, 0.44 mmol) was dissolved in anhydrous DMF (2 mL). To this solution, gemcitabine hydrochloride (200 mg, 0.64 mmol) was added and stirred until completely dissolved. Then, DIPEA (244 µL, 1.58 mmol) was added to the reaction mixture and allowed to react for 72 h under constant stirring at room temperature. The reaction mixture was cooled on ice, and the product was precipitated by adding excess cold brine water. The precipitate was vacuum filtered and dried under vacuum to afford compound **(3)**.

^{1}H NMR (300 MHz, CD$_3$OD, ppm): δ= 8.33 (d, 1H, C**H**=CH), 7.42-7.3 (m, 6H, Ar**H**), 7.3-7.1 (m, 10H, 9 Ar**H** and CH=C**H**), 6.27-6.21 (m, 1H, **H-1**), 4.4-4.28 (m, 1H, **H-3**), 4.0-3.9 (m, 2H, **H-5**), 3.82-3.75 (m, 2H, **H-4**), 2.5-2.4 (m, 2H, SC**H**$_2$ and 2H, NHCOC**H**$_2$).

For the synthesis of **(4)**, compound **(3)** (80 mg, 0.14 mmol) was dissolved in 2 mL

of TFA:DCM (1:1) mixture. To this solution, triethylsilane (0.5 mL, 3.0 mmol) was added. The reaction mixture was stirred for 1 h at room temperature. The product was dried under vacuum. The crude product with washed with diethyl ether (5 X 5 mL) and dried again to afford compound **(4)**.

^{1}H NMR (300 MHz, CD$_3$OD, ppm): δ= 8.34 (d,1H, C**H**=CH), 7.42 (d, 1H, CH=C**H**), 6.27-6.21 (m, 1H, **H-1**), 4.4-4.28 (m, 1H, **H-3**), 4.0-3.9 (m, 2H, **H-5**), 3.82-3.75 (m, 1H, **H-4**), 2.8-2.7 (m, 4H, SHC**H**$_2$ and NHCOC**H**$_2$).

2.2.3 Synthesis of TAB004-Gem-cisPt-MSNs.

2.2.3.1 Synthesis of AP-MSNs.

AP-MSNs were synthesized following our previous procedure with slight modifications (163, 164). Briefly, the surfactant CTAB (0.78 g, 2.14 mmol) was dissolved in a mixture of ethanol (3.32 mL) and nanopure water (21.6 mL), followed by the addition of DEA (41.4 µL, 0.428 mmol). This surfactant mixture was stirred for 30 min at 60 ℃. To this solution, APTES (7.64 µL, 32.6 µmol) was added, followed by the dropwise addition of TEOS (2.19 mL, 9.80 mmol) over a period of 5 minutes. The resulting suspension was stirred for 18 h at 60 ℃. Finally, the nanoparticles were collected via centrifugation at 13,000 rpm for 15 minutes, washed three times with ethanol and stored in ethanol.

The surfactant template was extracted by washing the MSNs in 1M HCl methanolic solution (10 mg of MSNs in 1 mL of the acidic solution). The MSNs were dispersed in the acidic solution and stirred for 10 h at 60 ℃. The MSNs were then collected via centrifugation and washed with ethanol three times. A second acid wash was performed under the same conditions for 6 h to warrant complete surfactant

extraction. Finally, the surfactant-free AP-MSNs were washed with ethanol three times and stored in ethanol.

2.2.3.2 Synthesis of cisPt-MSNs.

Cisplatin (IV) prodrug (disuccinotocisplatin) **(2)** was conjugated to AP-MSNs via coupling reaction mediated by EDC to afford cisPt-MSNs (161). AP-MSNs (1,000 mg) were dispersed in 30 mL of DMSO, followed by the addition of TEA (210 µL, 151.8 mg, 1.5 mmol). The MSN dispersion was stirred for 30 minutes. Meanwhile, compound **(2)** (400 mg, 0.75 mmol) and EDC (720 mg, 3.75 mmol) was dissolved in 20 mL of DMSO. This solution was added slowly to the MSN dispersion under constant stirring. The reaction mixture was stirred for 24 h at room temperature in dark. After the conjugation process, the nanoparticles were collected via centrifugation, washed once with DMSO, twice with ethanol and stored in ethanol. The supernatants obtained from the reaction and each washing solution were used to determine the amount of cisPt conjugated to the MSNs. The Pt content was analyzed using atomic absorption spectroscopy (Analyst 200).

2.2.3.3 Synthesis of phosphonate-grafted and NIR-labeled MSNs.

2.2.3.3.1 Synthesis of Phos-MSNs or Phos-cisPt-MSNs.

To functionalize the surface of MSNs with phosphonate groups, post-synthetic grafting of TPMP was carried out following the previously reported procedure with slight modifications (165). AP-MSNs or cisPt-MSNs (200 mg) were dispersed in 13 mL of nanopure water. An aqueous solution of TPMP (113.5 µL, 0.2 mmol in 13 mL water, pH adjusted to 6-7) was added to the MSN dispersion. The mixture was stirred for 3 h at 40 ºC. Finally, the nanoparticles were collected via centrifugation, washed thrice with ethanol to afford Phos-MSNs or Phos-cisPt-MSNs.

2.2.3.3.2 Synthesis of NIR silane derivative.

NIR silane derivative was synthesized following our previous procedure (163). Briefly, NIR-797 isothiocyanate (1.65 mg, 1.87 µmol) was dissolved in 1 mL of anhydrous DMF. To this solution, APTES (3.9 µL, 16.6 µmol) was added and allowed to react for 3 h at room temperature under slow stirring in dark. The as-synthesized NIR-silane derivative was used without any further purification.

2.2.3.3.3 Synthesis of NIR-labeled MSNs.

To synthesize MSNs labeled with NIR-797, AP-MSNs or cisPt-MSNs (200 mg) were dispersed in 13 mL of nanopure water. An aqueous solution of TPMP (113.5 µL, 0.2 mmol in 13 mL water, pH adjusted to 6-7) was added to the MSN dispersion. The mixture was stirred for 3 h at 40 ℃. Then 1 mL of the as-synthesized NIR silane derivative (described in the previous section) was added to the MSN reaction under stirring. The mixture was stirred for an additional 3 h at 40 ℃ covered from light. After the grafting reaction was complete, the nanoparticles were collected via centrifugation, washed thrice with ethanol and stored in ethanol. NIR-labeled MSNs were used for *in vivo* targeting ability and therapeutic efficacy studies.

2.2.3.4 Synthesis of PEI-coated MSNs.

MSNs were coated with PEI polymer using a procedure previously reported (132). Phosphonate-grafted MSNs (Phos-MSNs or Phos-cisPt-MSNs, 100 mg) were dispersed in 40 mL of ethanol. A PEI solution (1.8 KDa, 10 mL, 2.5 mg/mL in ethanol) was added to the MSN dispersion and stirred for 1 h at room temperature. The nanoparticles were collected via centrifugation and washed thrice with ethanol to afford PEI-MSNs or PEI-cisPt-MSNs.

The amount of PEI coated on the MSN surface was determined using the ninhydrin assay, which is commonly used for the quantification of primary amines (166). Briefly, PEI-MSNs (1 mg) were dispersed in ethanol (4 mL). To the nanoparticle dispersion, 1 mL of ninhydrin reagent (15 mg/mL in ethanol) was added. The suspension was stirred for 24 h at room temperature. The MSNs were centrifuged, and the supernatant was collected. The absorbance of the supernatant was measured at 575 nm using UV-vis spectroscopy. The assay was calibrated using the same procedure for the various concentration of free PEI polymer.

2.2.3.5 Synthesis of Gem- and Gem-cisPt-MSNs.

Conjugation of Gem prodrug (4) to MSNs was carried out in a two-step process. Firstly, PEI coated MSNs were reacted with heterobifunctional linker via NHS coupling reaction to afford SPDP-MSNs (167). PEI-MSNs or PEI-cisPt-MSNs (30 mg) were dispersed in 15 mL of anhydrous acetonitrile. To this nanoparticle dispersion, SPDP (15 mg, 48 µmol) was added. The mixture was stirred for 24 h at room temperature. The MSNs were collected via centrifugation, washed thrice with ethanol, and stored in ethanol.

Secondly, compound (4) was conjugated to SPDP-MSNs via a disulfide exchange reaction to produce Gem-MSNs. SPDP-MSNs or SPDP-cisPt-MSNs (30 mg) were dispersed in 10 mL of methanol. To this nanoparticle dispersion, a 5 mL solution of compound (4) (30 mg, 85.4 µmol) in methanol was added. The mixture was stirred for 48 h at room temperature. After the conjugation reaction, the MSNs were collected via centrifugation, washed once with methanol, once with ethanol to obtain Gem-MSNs or Gem-cisPt-MSNs.

The amount of Gem conjugated to MSNs was determined by measuring the amount of 2-thiopyridine, which is the byproduct released after disulfide exchange reaction between compound **(4)** and SPDP-MSNs (167). The supernatants obtained from the reaction and washing solutions were used to determine the amount of byproduct by using the absorbance at 375 nm.

2.2.3.6 Synthesis of PEG-Gem-cisPt-MSNs or Mal-PEG-Gem-cisPt-MSNs.

Gem-cisPt-MSNs (30 mg) was dispersed in 15 mL of anhydrous acetonitrile. To this dispersion, MeO-PEG-SCM or Mal-PEG-SCM (30 mg) was added and stirred for 5 days at room temperature. Finally, the MSNs were collected via centrifugation, washed thrice with ethanol to afford PEG-Gem-cisPt-MSNs or Mal-PEG-Gem-cisPt-MSNs.

2.2.3.7 Synthesis of TAB004-Gem-cisPt-MSNs.

2.2.3.7.1 Modification of TAB004 antibody to afford TAB004-SH.

TAB004 antibody was firstly modified to achieve free sulfhydryl groups using the sulfhydryl addition kit (Thermo scientific, 23460). Briefly, TAB004 (1 mg) was diluted in PBS buffer (1 mL). SATA solution (6 µL, 4 mg/mL in anhydrous DMF) was added to the TAB004 solution. This solution was allowed to incubate for 30 min at room temperature to afford SATA modified antibody. For the deprotection step, hydroxylamine-HCl (5 mg) was dissolved in 100 µL of conjugation buffer provided in the kit. The hydroxylamine solution was added to the TAB004 solution and incubated for 2 h at room temperature with occasional slow mixing. Sulfhydryl-modified TAB004 (TAB004-SH) was applied to the dextran desalting column to remove the unreacted reagents. The fractions (1 mL each) were collected and the absorbance of the fractions was measured at 280 nm, which indicates the presence of antibody. Finally, all the

fractions containing the antibody were pooled together and stored at 4 ºC.

2.2.3.7.2 Synthesis of TAB004-Gem-cisPt-MSNs.

The Mal-PEG-Gem-cisPt-MSNs were functionalized with sulfhydryl-modified TAB004 via maleimide-thiol conjugation reaction to afford TAB004-Gem-cisPt-MSNs. Mal-PEG-Gem-cisPt-MSNs (15 mg) were dispersed in 10 mL of conjugation buffer (Thermo scientific, 23460). TAB004-SH described in the previous section was added to the nanoparticle dispersion. The solution was stirred for 48 h at 4 ºC covered from light. Finally, the nanoparticles were collected via centrifugation, washed with autoclaved water three times, and stored in autoclaved water at 4 ºC.

2.2.4 Synthesis of physically loaded Gem-cisPt-MSNs (PL-Gem-cisPt-MSNs).

For the synthesis of PL-Gem-cisPt-MSNs, Phos-MSNs (10 mg) were dispersed in 5 mL of methanol. A 2 mL solution of Gem/cisPt (6.17/1.33 mg) was added to the MSN dispersion and stirred slowly for 48 h at room temperature. The MSNs were collected via centrifugation and re-dispersed in ethanol. After that, the PEI solution (1 mL, 2.5 mg/mL) was added to the drug-loaded MSNs (10 mg in 4 mL ethanol) and then stirred for 1 h at room temperature. The MSNs were then collected via centrifugation, washed three times with ethanol to afford PL-Gem-cisPt-MSNs. The supernatants and washing solutions were used to determine Gem and cisPt content using UV-Vis and AAS, respectively.

2.2.5 Characterization of synthesized MSNs.

2.2.5.1 Transmission electron microscopy (TEM).

TEM images were obtained by JEOL TEM 2100 LaB6 with 200 kV acceleration voltage to visualize the size and morphology of MSNs. The MSNs were dispersed in ethanol and sonicated before a drop was placed on the lacey carbon grid. The samples

were air-dried before imaging. For the negative staining with Nano-W^{TM} (Nanoprobes, Inc.), a drop of TAB004-Gem-cisPt-MSNs dispersed in PBS was placed on the grid. Before the sample was completely dried, a drop of the Nano-W^{TM} was added, followed by a second drop after a minute. The sample was finally air-dried on the grid before imaging.

2.2.5.2 Dynamic light scattering (DLS).

Hydrodynamic sizes of MSNs and zeta potential measurements were performed in a Malvern Instrument Zetasizer Nano. MSNs (0.1 mg/mL) were dispersed in water or PBS (1 mM), sonicated for 10 minutes and analyzed for hydrodynamic size and surface charge.

2.2.5.3 Surface area and pore size analysis.

The MSNs (10-20 mg) were dried under vacuum and degassed overnight to remove any physiosorbed contaminants. The dried MSNs were used to determine the N_2 isotherms. The N_2 sorption isotherms were determined in a NOVA 2200e Quantachrome surface area and pore size analyzer. The surface area of the MSNs was determined using the BET method, and the pore size and pore volume were determined using the BJH method.

2.2.5.4 Thermogravimetric analysis (TGA).

Vacuum dried MSN sample (4-5 mg) was used to evaluate organic content analysis. TGA was carried out using a Mettler Toledo TGA/SDTA851 instrument equipped with a platinum pan and a heating rate of 1 °C/min from 25 to 800 °C under a nitrogen atmosphere. The sample was held at 800 °C for 3 h to make sure that all the organic material had been calcined.

2.2.6 *In vitro* studies.

2.2.6.1 *Cell culture.*

KCM cells were generated from the PDAC tumors in spontaneous transgenic PDA.MUC1 mice and were generously provided by Dr. Mukherjee (UNC Charlotte) (140). Human PDAC cells, including AsPC1, Capan-1, and HPAF II, and normal pancreatic ductal cells (HPDE) were purchased from ATCC. KCM, Capan-1 and HPDE cells were cultured in DMEM supplemented with 10% FBS, 1% penicillin and streptomycin, 1% Glutamax, and 1% NEAA. AsPC1 cells were cultured in RPMI supplemented with 10% FBS and 1% penicillin and streptomycin. HPAF II cells were cultured in EMEM supplemented with 10% FBS, 1% penicillin and streptomycin, 1% Glutamax, and 1% NEAA. All the cells were maintained at 37 °C under a 5% CO_2 atmosphere. The cell culture and incubation conditions for all *in vitro* experiments are as indicated above unless otherwise mentioned. The media volume for each well in 96-well plate is 100 μL, 24-well plate is 500 μL and the 6-well plate is 2 mL.

2.2.6.2 *Determining combination index (CI) of Gem/cisPt in PDAC cells.*

KCM and HPAF II cells were seeded in 96-well plates at a cell density of 500 and 2000 cells per well, respectively. After 24 h of incubation, the cells were inoculated with increasing concentrations of various molar ratios of Gem:cisPt (100:0, 50:50, 75:25, 80:20, 85:15, 90:10 and 0:100). The drugs were directly dissolved in cell culture media at different concentrations. Cells were treated with the drugs for 48 h. The cells were then washed once with PBS, replaced with fresh media and incubated for another 24 h for recovery. Finally, the cells were washed once with PBS, and cell viability was evaluated using MTS assay.

For MTS assay, 20 µL of the CellTiter 96® solution was added to each well containing 100 µL media. The cells were incubated for 2.5-3.5 h depending on the cell type, and the absorbance was measured at 490 nm using a Multiskan FC plate reader.

Non-regression fit of the dose-response data was used to determine the IC_{50} values using Graphpad Prism. These IC_{50} values at each Gem:cisPt ratio were used to calculate the combination index values using the following formula:

$$CI = \frac{(D_m)a}{(D)a} + \frac{(D_m)b}{(D)b} + \alpha \left[\frac{(D_m)a}{(D)a} * \frac{(D_m)b}{(D)b} \right] \qquad \text{Equation (1)}$$

where $(D_m)a$ and $(D_m)b$ is the concentration of drug a and b in the combination that yields 50% growth inhibition (IC_{50} for the combination), $(D)a$ and $(D)b$ are the concentrations of the drugs a and b alone that yields 50% growth inhibition (IC_{50} for individual drugs), and $\alpha = 1$ is chosen for mutually non-exclusive drugs. CI values >1.0 are considered additive, <0.9 are synergistic, and <0.4 are strongly synergistic (168).

2.2.6.3 Cytotoxicity of Gem-cisPt-MSNs in PDAC cells.

The following PDAC cells were used for the cytotoxicity analysis: KCM, HPAF II, AsPC1, and Capan-1, and HPDE cells were used as control. KCM cells were seeded at a cell density of 500 cells per well and Capan-1 cells at 1000 cells per well. HPAF II, AsPC1 and HPDE cells were seeded at a density of 2000 cells per well. The cells were seeded in 96-well plates and then incubated for 24 h. The cells were then inoculated with different MSN materials (**Table 2.1**) at a range of concentrations, 1 to 100 µg/mL. The MSNs were prepared in complete cell culture media and cells were treated with MSNs for 48 h. Then the cells were washed once with PBS, replaced with fresh media and incubated for another 24 h for recovery. Post-treatment, the cell viability was evaluated using MTS assay as described in the previous section. The results are reported as average

IC$_{50}$ values for three independent experiments (n=3).

Table 2.1. MSN materials used for the *in vitro* studies.

Sample	Details	Drug concentration in 1 mg/mL MSNs	
		cisPt (μM)	Gem (μM)
PEI-MSNs	Control MSNs with no drugs	-	-
cisPt-MSNs	MSNs conjugated with cisPt only	0.17	-
Gem-MSNs	MSNs conjugated with Gem only	-	0.91
Gem-cisPt-MSNs	MSNs conjugated with both Gem and cisPt	0.17	0.91
Physical mixture of Gem-MSNs plus cisPt-MSNs	MSNs conjugated with single drug, but physically mixed	0.17	0.91

2.2.6.4 H2A.X phosphorylation in KCM cells.

KCM cells were seeded in 24-well plates at a density of 20,000 cells and incubated for 48 h. The cells were treated for 24 h with the MSN materials listed in **Table 2.1**. The cells were washed once with PBS, detached using trypsin, and centrifuged to collect the cell pellet. The cells were washed once with PBS and resuspended in the fixative solution (Sigma Aldrich, 17-344) and incubated on ice for 20 min. The cells were then washed twice with PBS, mixed with the 100 μL permeabilizing solution (Sigma Aldrich, 17-344) and incubated for 5 min. Following addition of the FITC-conjugated anti-phosphorylated H2A.X antibody (3.5 μL), cells were incubated on ice for 20 min. After the final wash, the cell pellet was resuspended in PBS. The cells were immediately analyzed by flow cytometry. The results are reported as the percentage of FITC positive cells (average ± SD) obtained from three independent experiments (n=3).

2.2.6.5 DNA damage protein analysis using western blot.

KCM cells were seeded at a density of 100,000 cells and incubated for 48 h. The cells were treated for 24 h with the MSN materials listed in **Table 2.1**. The cells were

washed with PBS, detached using trypsin, centrifuged, and the cell pellet was collected. The cells were washed once with cold PBS lysed with 100 μL lysis buffer. The cell lysates were isolated by centrifugation at 13,000 rpm for 30 min at 4 ℃. 1 μL from the cell lysate was taken used for protein quantification (BIORAD). The cell lysate was mixed with sample buffer (Sigma, Laemmli 2X concentrate), boiled at 100 ℃ for 5-7 mins, then cooled down on ice for 1 min and then centrifuged at 13,000 rpm for 45 seconds. The cell lysates were then stored in -80 ℃ and used for the western blot analysis.

For western blotting analysis, cell lysates (10 μg of total protein per lane) was loaded for each sample and Pageruler[TM] Prestained protein ladder (Thermo Scientific, 26616) was used as the Protein Ladder to carry out the SDA-PAGE run. After the SDS-PAGE run, PVDF membrane was used to transfer the proteins from the gel onto PVDF membranes. Then, after 2 h of transferring, membranes were blocked with 6-7% Milk-TBST (1:10 TBS buffer: Di H2O + 0.1%Tween20) buffer. After milk blocking, membranes were washed 3 times, 10 mins each. Then appropriate antibodies were added and incubated overnight at 4 ℃ under slow rocking. Next day, secondary antibodies (Cell Signaling, HRP-linked conjugate Anti-Mouse-IgG, 707S and Anti-rabbit-IgG, 7074S) were added to the membranes after washing them 3 times with TBST buffer, 10 min each. Secondary antibody incubation period was 1 hour in room temperature rocker. Then the membranes were washed again 3 times with TBST buffer, 10 mis each. Then the membranes were stained with ECL reagents (ADVANSTA, Western Bright ECL, K-12045-D50) for 5-10 min. Antibody Tubulin was used for loading control. Experimental protein of interest level quantification was normalized against Tubulin. Antibodies

against RPA32 phosphorylation at Ser33 (Bethyl Laboratories, A300-246A), Chk1 phosphorylation at Ser345 (Cell Signaling Technology, 2348), Chk1 (Santa Cruz Biotechnology, sc7898), YH2AX phosphorylation at Ser139 (Cell Signaling, 25775), H2AX (Cell Signaling, H2AX-D17A3-XP, 76315), and Tubulin (Santa Cruz Biotechnology, sc-8035) were used. Antibodies against human RPA32 (Thermo Fisher Scientific) and Chk1 (Cell Signaling Technology, 2360) were used.

2.2.6.6 Cell apoptosis in KCM cells using annexin V-FITC/PI assay.

KCM cells were seeded in 24-well plates at a density of 20,000 cells and incubated for 48 h. The cells were inoculated for 24 h with MSNs (**Table 2.1**) prepared in complete cell culture media. The cells were then washed once with PBS, detached using trypsin, and centrifuged to collect the cell pellet. The cell pellet was gently mixed in 1 mL of 1X binding buffer (BD pharmingen, 556547) and washed once. The cells were resuspended in 200 µL of binding buffer followed by the addition of 5 µL of Annexin V-FITC solution. The cell suspensions were incubated for 15 min at room temperature in dark. Then, 700 µL of the binding buffer was added and the cells were washed again. The cell pellet was resuspended in 200 µL of binding buffer and transferred to flow cytometry tubes. Then, 5 µL of propidium iodide (PI) solution was added to each tube and incubated for 5-10 min at room temperature in dark. The cells were immediately analyzed using low cytometry (Fortessa FACS). Cells negative for both Annexin V-FITC and PI (FITC-/PI-) are considered healthy; Annexin V-FITC positive and PI negative (FITC+/PI-) cells are considered early apoptotic; positive for both Annexin V-FITC and PI (FITC+/PI+) cells are considered late apoptotic; finally, Annexin V-FITC negative and PI positive (FITC-/PI+) cells are considered necrotic. Data is presented as apoptotic cells (early plus

late apoptotic cells) and the results are reported as the average ± SD of three independent experiments (n=3).

2.2.6.7 In vitro targeted cytotoxicity of TAB004-Gem-cisPt-MSNs.

KCM, HPAF II, and HPDE cells were seeded in 96-well plate at a cell density of 500, 2000 and 2000 cells per well, respectively and then incubated for 24 h. PEG-Gem-cisPt-MSNs and TAB004-Gem-cisPt-MSNs prepared in complete cell culture media were added to the cells at concentrations ranging from 1 to 100 µg/mL and the cells were treated for 48 h. The cells were then washed once with PBS, replaced with fresh media and incubated for another 24 h for recovery. Finally, the cell viability was determined using the MTS assay following the procedure described in the previous section.

2.2.7 In vivo targeting ability and therapeutic efficacy of TAB004-Gem-cisPt-MSNs in subcutaneous syngeneic KCM mice model.

All animal experiments were reviewed and approved by the University of North Carolina Charlotte (Charlotte, NC) Institutional Animal Care and Use Committee (IACUC) under protocols 14-015 and 17-015. Immune-competent C57BL/6 mice used this study were purchased from Jackson Laboratory.

2.2.7.1 Establishing the subcutaneous syngeneic KCM tumor model.

KCM cells derived from the pancreatic tumors of PDA.MUC1 mice are transplanted in C57BL/6 mice to develop syngeneic KCM mice (140). To establish the KCM tumors, mice were implanted subcutaneously (s.c, right flank) with KCM cells ($1x10^6$) mixed in Matrigel (1:1 dilution in PBS). Tumor growth was monitored by caliper measurements every alternate day, and the tumor volume was calculated using the following formula:

$$\text{Tumor volume} = (L*(W)^2)/2 \qquad\qquad \text{Equation (2)}$$

where L is the length and W is the width of the tumor (169).

In vivo targeting ability and therapeutic efficacy studies were initiated 7 days post KCM cell implantation with tumor volumes reaching approximately 100 mm^3.

2.2.7.2 In vivo targeting of TAB004-Gem-cisPt-MSNs.

The targeting ability of the TAB004-Gem-cisPt-MSNs was evaluated in the syngeneic KCM mice 7 days post KCM cell implantation. The KCM tumor-bearing mice were injected intravenously with NIR-labeled TAB004-Gem-cisPt-MSNs or PEG-Gem-cisPt-MSNs (40 mg/Kg). The mice were imaged prior to the administration of the MSN material and at 30 min, 1, 4, 24, 48 and 96 h post injection using the IVIS$^®$ Spectrum imaging system (PerkinElmer). The images were analyzed using the Living Image® Software (version 4.5.5, PerkinElmer). The mice were euthanized after 96 h and the major organs including liver, lungs, kidneys, spleen and tumor, were collected. The *ex vivo* fluorescence associated with the organs was also measured using the IVIS imaging system.

2.2.7.3 Therapeutic efficacy of TAB004-Gem-cisPt-MSNs.

To determine the therapeutic efficacy of TAB004-Gem-cisPt-MSNs, mice bearing KCM tumors were randomly divided into 4 groups (n=5); PBS, free Gem/cisPt, PEG-GEM-cisPt-MSNs and TAB004-Gem-cisPt-MSNs. Tumors reached approximately 100 mm^3 7 days after KCM cell implantation. Mice were then intravenously injected with PBS, free Gem/cisPt (9.52/2.05 mg/Kg), PEG-Gem-cisPt-MSNs (40 mg/Kg) and TAB004-Gem-cisPt-MSNs (40 mg/Kg). The treatment consisted of a total of 6 injections with a 4 days-interval between each injection. Tumor growth was monitored every other

day using calipers. On day 34 post KCM cell implantation, mice were euthanized, and the major organs were collected including liver, lungs, kidneys, spleen, heart, and tumor. The fluorescence associated with each organ was evaluated using the IVIS imaging system. Tumors were weighed to determine the therapeutic effect on the tumor weight and size. Portions of the organs and tumors were fixed in formalin for histological analysis. Also portions of the organs and tumors were frozen for Si and Pt content analysis.

2.2.7.4 Post treatment analysis of blood and tissues.

2.2.7.4.1 Blood serum analysis.

Blood was collected by cardiac puncture following the recommendations of the IACUC. The blood of each mouse was stored in microcentrifuge vials at 4 ºC. The serum was obtained following centrifugation and stored at -80 ºC. Serum samples were evaluated for markers of liver and kidney functions (IDEXX).

2.2.7.4.2 Ex vivo fluorescence imaging and analysis.

The harvested organs were placed in Petri dishes and imaged using the IVIS® Spectrum imaging system. The fluorescence images were analyzed, and fluorescent intensity was quantified using the ROI tool of the Living Image® software. The data is presented as the average radiant efficiency associated with each organ. The results are reported as the mean ± SD (n=3mice per treatment group).

2.2.7.4.3 Analysis of organ Si and Pt content.

Samples from different organs, including the liver, lungs, heart, spleen, kidneys, and tumor, were weighed and thoroughly dried in an oven at 60 ºC for 3 days. The dried organs were weighed again and digested using a mixture of HNO_3:HCl:HF (10:2:1). The samples were placed in the digestion vessels with the acid mixture for a 20 min pre-

digestion at room temperature. The samples were then further digested in a CEM Mars microwave system under the following conditions: ramp to 200 ℃ for 20 minutes, hold at 200 ℃ for 20 minutes and cool down to room temperature. The digested samples were then diluted to 50 mL using DI water.

The Si content was analyzed using an ICP-OES (PerkinElmer 8300 DV). Calibration standards were prepared by diluting the Si element PlasmaCAL (SCP Science) standard in 0.1 M HNO_3. The wavelength of 251.66 nm was selected for Si analysis and the concentrations was determined using Syngistix software. The data are represented as the mg of Si per g of tissue. For each organ tested, the results are reported as the average ± SD (n=5 mice per group).

The Pt content was analyzed using an ICP-MS (Thermo Electron X series). The Pt analysis was performed by monitoring the signal of the [195]Pt isotope. Calibration standards were prepared by diluting Pt standard in 5% HCl matrix. The data are represented as µg of Pt per g of tissue. For each organ tested, the results are reported as the average ± SD (n=5 mice per group).

2.2.7.4.4 Histology and Immunohistochemistry.

a. <u>Hematoxylin and eosin (H&E) staining</u>. Major organs such as liver, lungs, spleen, kidneys, heart, and tumors were collected after *in vivo* experiments. For each tissue, a small portion was fixed in a 10% buffered formalin for 24 h at 4 ℃. The fixed tissues were stored in transferred and stored 70 % ethanol. The organs were paraffin-embedded, sectioned (4 µm thick), and stained with Hematoxylin and Eosin (H&E). The H&E stained tissue sections were imaged using a fluorescent microscope (IX71,

Olympus) at 4x and 10x magnification. Histological signs of toxicity i.e., changes in normal tissue structures were investigated.

b. Immunohistochemistry (IHC) for apoptotic cells in tumor tissue. Tumor sections (10 μm) were used to determine apoptotic cells using the "*In situ* Apoptosis Detection Kit (ab206386, Abcam)" as per the manufacturer's instructions. The tissue sections stained for apoptosis were imaged using a fluorescent microscope at 10x magnification (IX71, Olympus).

2.2.8 *In vivo* therapeutic efficacy in spontaneous transgenic PDA.MUC1 mice model.

2.2.8.1 Establishing PDA.MUC1 mice.

PDA.MUC1 mice were generated and the mice colonies are maintained by Dr. Mukherjee Lab (UNC Charlotte). PDA.MUC1 mice are a triple transgenic cross of LSL-KRAS^{G12D} x P48-Cre x Human MUC1.Tg where the P48-Cre mice have a tamoxifen-inducible promoter; and therefore, oncogenesis is initiated only when mice are treated with tamoxifen (75 mg/kg in 100 μL of corn oil, 1 injection per day for 2 weeks. Following tamoxifen treatment, the mice develop pancreatic tumors spontaneously and express human MUC1 similar to that in humans (170).

2.2.8.2 Therapeutic efficacy of TAB004-Gem-cisPt-MSNs.

To determine the therapeutic efficacy of TAB004-Gem-cisPt-MSNs, PDA.MUC1 mice approximately 30 weeks post tamoxifen induction were used. Mice were injected with TAB004-Gem-cisPt-MSNs at a dose of 40 mg/Kg. The therapeutic regimen consisted of a total of 6 injections (every 15 days). After the treatment, mice were euthanized, and the major organs were collected including liver, lungs, kidneys, spleen and tumor. The fluorescence associated with each organ was measured using the IVIS

imaging system. The pancreas was weighed and fixed in formalin. The pancreas was sectioned at 4 μm thickness at various depths of the tissue. A total of 4 sections were stained with H&E and imaged to determine the grade of PanIN lesions and extent of invasive PDA.

2.2.9 Statistical analysis.

All the data in this chapter is represented as mean ± SD unless mentioned otherwise. The hydrodynamic size and ζ-potential analysis using DLS were performed in triplicates. The amount of drug conjugated to MSNs is reported as average of 5 independent batches (n=5). For the cell viability studies, the GraphPad prism was used to calculate the IC_{50} values (n=6). The DNA damage, DNA damage response markers and apoptosis studies were performed in triplicates (n=3). The statistical analysis for DNA damage and apoptosis studies was performed with One-way ANOVA using Tukey's multiple comparison test. The *in vivo* therapeutic experiments were evaluated using n=5 mice per group. The tumor volumes were reported as mean ± SEM, and two-way ANOVA with Tukey's multiple comparison test was used for statistical analysis. For tumor weights, unpaired t-test was performed to analyze the statistical difference of each group. The NIR fluorescence, Si and Pt content in organs were evaluated using n=5 mice per group. All the statistical analysis were performed using GraphPad Prism (v8.2.0 for Windows, La Jolla California, CA, USA) with α=0.05 and reported as stars assigned to the p values; ****$p \leq 0.0001$, ***$p \leq 0.001$, ** $p \leq 0.01$, * $p \leq 0.05$ and ns $p > 0.05$.

2.3 Results and discussions.

2.3.1 Synergistic ratio of Gem/cisPt combination in PDAC cells.

Primary requirement of combination therapy is to identify the drug combinations

that exhibit ratio-dependent synergy. Thus, combined effect of Gem/cisPt was determined using the most common approach, by calculating the combination index (CI) value determined using the Chou and Tallay method (168). The combination of drugs at a specific ratio is antagonistic and additive at CI values of >1 and =1, respectively. The combination is synergistic at CI values <1 and in particular, the CI values of <0.4 depict strong synergism between the drugs.

PDAC cells, KCM and HPAF II, were treated with various molar ratios of Gem:cisPt (100:0, 50:50, 75:25, 80:20, 85:15, 90:10 and 0:100) for 48 h. The mean drug concentration required to obtain 50% of growth inhibition (IC_{50}) was determined at every ratio of Gem:cisPt. The IC_{50} values were further used to determine the CI value at each specific ratio of Gem:cisPt tested. As depicted in **Figure 2.1**, with KCM cells, all Gem/cisPt ratios tested led to strong synergy with CI values lower than 0.4 and the strongest synergy was observed at the Gem:cisPt ratio of 85:15 with a CI value of 0.26. Treated similarly, HPAF II cells also exhibited the lowest CI value of 0.42 at the Gem:cisPt ratio of 85:15. For both cell types, the second-lowest CI value was observed with the Gem:cisPt ratio of 80:20. Previous reports of Gem/cisPt combination against bladder cancer cells demonstrated similar synergistic ratio, nevertheless such studies have not been reported for PDAC (171). Hence, we used the synergistic window of 85:15 to 80:20 (Gem:cisPt), as the reference ratio to design drug in MSNs.

Ratio	KCM		HPAF II	
Gem:cisPt	IC_{50} (nM)	CI	IC_{50} (nM)	CI
100:0	42		217	
0:100	6600		4010	
50:50	25	0.30	218.6	0.54
75:25	17	0.34	144.4	0.51
80:20	15	0.28	136.5	0.51
85:15	13	0.26	106.0	0.42
90:10	32	0.35	122.0	0.51
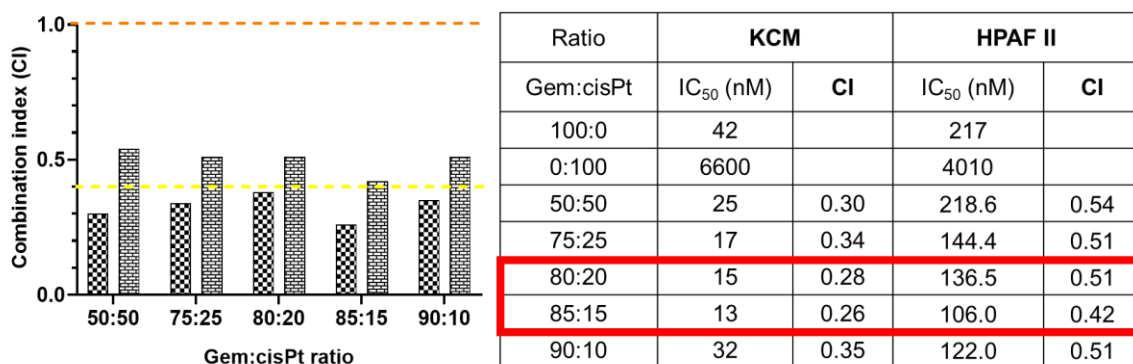
Figure 2.1. Combination index (CI) values of Gem:cisPt in KCM and HPAF II cells. **(a)** CI values determined at various ratios of Gem:cisPt, in KCM (checkered pattern) and HPAF II (brick pattern) cells. The limit defining the synergism at CI = 1 (orange dotted line) and strong synergism at CI < 0.4 (yellow dotted line). **(b)** Tabulated IC_{50} and CI values observed in KCM and HPAF II cells upon treatment with various molar ratios of Gem:cisPt. The lowest CI values in each cell line were observed at the ratios 80:20 and 85:15 (red box).

2.3.2 Synthesis and characterization of cisPt and Gem prodrugs.

Combination therapies require strategic synthetic and delivery design to fix or maintain the synergistic ratio, control release and prevent systemic leakage of drugs. Usage of nanocarriers along with chemical conjugation of drugs provides an excellent approach to meet these criteria as well as prevent batch-to-batch disparity observed in physical encapsulation, maintain the synergistic ratio, impart stimuli-responsive and controlled drug release at the target site, and eliminate off-target toxicities (172). In this direction, we firstly synthesized the chemotherapeutic prodrugs, bio-reversible derivatives of drug molecules in which chemical moieties are covalently attached to the drugs (173). These chemical moieties provide as handles for conjugation to nanocarriers as well as stimuli-responsive binds for controlled drug delivery.

The cisplatin prodrug was synthesized in a two-step procedure. The first step involved the oxidation of cisplatin using hydrogen peroxide to afford dihydroxycisplatin (IV) **(1)**. In the second step, the esterification reaction of compound **(1)** with succinic

anhydride afforded dissucinotocisplatin (IV) **(2)** (**Figure 2.2**). The successful synthesis of compound **(1)** was confirmed by FTIR, which showed the characteristic stretching vibrations at 3,514 cm^{-1} associated to O-H bond. Compound **(2)** was characterized using both FTIR and ^{13}C NMR techniques. The FTIR spectrum of compound **(2)** showed the characteristic stretching vibrations at 3184 cm^{-1} and 1736-1706 cm^{-1} corresponding to O-H and C=O bonds, respectively, which are associated to the carboxylic acid group. The ^{13}C NMR spectra of compound **(2)** showed peaks at 180.1 ppm, 174-172 ppm, 30.9 ppm, and 30.3 ppm, corresponding to ester **C**OOR, carboxylic acid **C**OOH, CH$_2$**C**H$_2$COOH, and **C**H$_2$COR, respectively, where R represents [PtCl$_2$(NH$_3$)$_2$]. These values were similar to the precious reports (161). The cisplatin (IV) prodrug **(2)** provides carboxylic groups as chemical handles for the chemical conjugation with the amino-propyl functional groups on the AP-MSNs. The prodrug conjugated to MSNs (cisPt-MSNs) leads to the stimuli-responsive release of cisPt under the reductive conditions present in cancer cells, as demonstrated by our group and others (161).
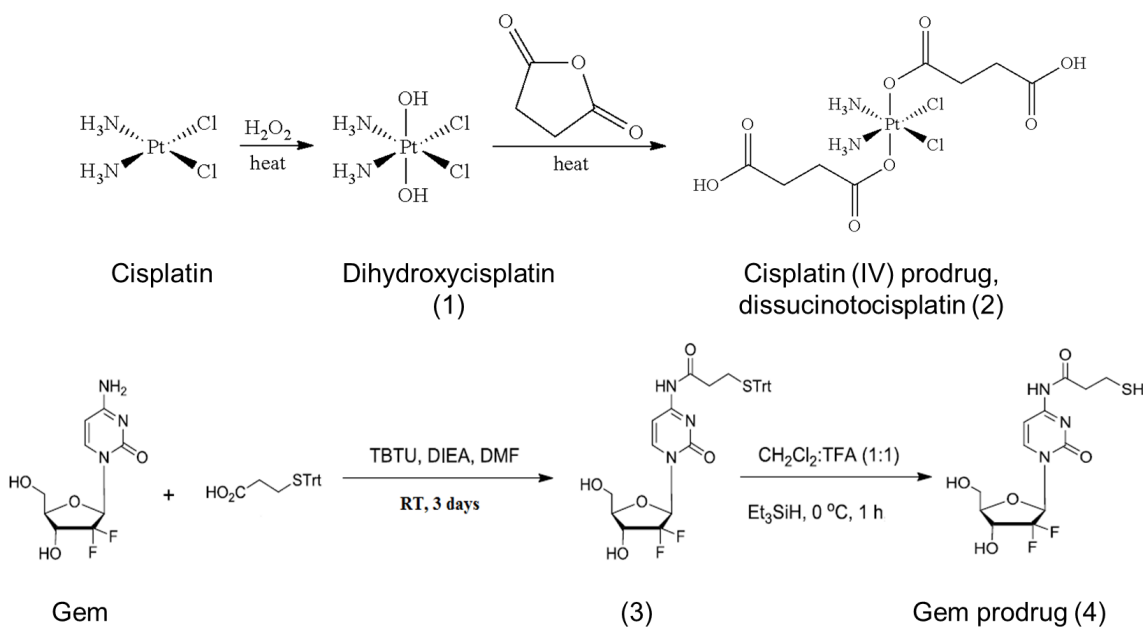
Figure 2.2. Schematic reaction steps and conditions involved in the synthesis of cisPt and Gem

prodrugs.

Gem prodrug **(4)** was synthesized following a two-step procedure previously reported (162) with slight modifications. The acylation of Gem with 3-(tritylthio) propionic acid mediated by TBTU was performed as the first step to afford compound **(3)** (**Figure 2.2**). Further, compound **(3)** was deprotected under acidic conditions using triethylsilane to afford the Gem prodrug **(4)**. The successful synthesis of compound **(3)** was confirmed by ^{1}H NMR, showing the presence of characteristics peaks at 7.41-7.37 ppm (6H) and 7.28-7.20 ppm (9H) corresponding to aromatic protons associated to the trityl group in the compound **(3)**. The successful synthesis of compound **(4)** was also confirmed by ^{1}H NMR by the absence of the aromatic protons' peaks.

Various Gem prodrugs have been used to overcome limitations associated with Gem (174). Importantly, coupling at the N-4 position of Gem is a widely utilized strategy to confer protection from enzymatic degradation by cytidine deaminase (CDA) (175). In our work, the Gem prodrug compound **(4)** is protected against deamination due to the modification at N-4 position via protection with an amide bond. Moreover, the SH functional group aids the conjugation to MSNs and imparts stimuli-responsive properties via the redox-responsive disulfide bonding between Gem and MSNs.

2.3.3 Synthesis and characterization of TAB004-Gem-cisPt-MSNs.

Nanocarrier design is critical to achieve maximum and controlled drug loading for efficient co-delivery of multiple drugs. To achieve optimal chemical conjugation of Gem/cisPt prodrugs at the synergistic ratio, we followed a multi-step procedure (**Figures 2.3 and 2.5a**). Our rational design consisted of localizing cisPt and Gem prodrugs at the internal porous and external surface of the MSNs, respectively. This novel approach will take advantage of the unique structural features of MSNs for maximum drug loading,

drug protection and controlled drug release.

AP-MSNs were synthesized using the surfactant template-based, co-condensation approach to graft APTES affording even distribution of the amino-propyl (AP) groups in the interior walls of MSNs. After CTAB surfactant removal, the amine groups in AP-MSNs were used for the chemical conjugation of cisPt prodrug (**2**) to afford cisPt-MSNs (**Figures 2.3 and 2.5a**). The cisPt prodrug was conjugated via a coupling reaction between the carboxylic acid of compound (**4**) and the amino groups of AP-MSNs mediated by EDC as the coupling agent.

Synthesis of AP-MSNs
- APTES was co-condensated in the interior surface of MSN framework to afford AP-MSN

Chemical conjugation of cisplatin prodrug
- EDC coupling reaction between cisPt prodrug and amine groups in AP-MSN mediated by EDC
- **5.1 ± 0.9** wt% cisPt

Grafting of phosphonate and NIR dye
- Phosphonate groups were grafted on exterior surface MSN
- NIR-797 dye was conjugated to MSNs for *in vivo* imaging

Functionalization of PEG and TAB004
- PEG conjugation via NHS coupling
- Functionalization of TAB004 via Maleimide-thiol chemistry
- **5.7-9.2** μg of TAB004 per mg of MSN

Chemical conjugation of Gemcitabine prodrug
- Gem prodrug was chemically attached using SPDP linker
- **23.9 ± 2.6 wt% Gem**

PEI coating of MSNs
- PEI was electrostatically bound to the phosphonate groups grafted on MSN surface
- **1.1± 0.2 μmoles** of NH$_2$

Figure 2.3. Detailed flowchart describing the multistep procedure followed for the synthesis of TAB004-Gem-cisPt-MSNs.

The cisPt-MSNs were post-synthetically grafted with TPMP to afford Phos-cisPt-MSNs. The phosphonate groups on the external surface of MSNs impart an overall negative charge. Next, polyethyleneimine polymer (PEI, 1.8 kDa) was bound to the MSNs surface through electrostatic interaction of the phosphonate groups with the amines of the PEI polymer. PEI-cisPt-MSNs were then derivatized using a

heterobifunctional linker, succinimidyl 3-(2-pyridyldithio)propionate (SPDP), to afford an intermediate SPDP-cisPt-MSNs. The NHS functional site on the SPDP reacts with the amines from the PEI polymer forming an amide bond (176). Moreover, SPDP introduced the pyridyldithio group, which further reacted with the Gem prodrug **(4)** forming the redox-responsive disulfide bond to afford Gem-cisPt-MSNs.

Gem-cisPt-MSNs were modified with PEG polymer to increase the blood circulation time of the nanoparticles *in vivo*, decrease non-specific cellular uptake, and provide reactive sites for further functionalization with TAB004. The MeO-PEG-NHS or Mal-PEG-NHS heterobifunctional polymers were conjugated to Gem-cisPt-MSNs via the NHS coupling reaction to residual amines on the PEI polymer. The Mal-PEG-Gem-cisPt-MSNs were finally functionalized with TAB004 antibody, via maleimide-thiol chemistry. The TAB004 was previously modified to incorporate free sulfhydryl groups (TAB004-SH).

The structural properties of MSN materials were characterized for hydrodynamic size (D_h) and surface charge, TEM, N_2 isotherms, organic content analysis, and drug content in MSNs (**Figure 2.5 and Table 2.2**). The as-synthesized AP-MSNs were found to be spherical with a diameter of 47.2 ± 3.9 nm according to TEM images (n=50 particles analyzed using image J) (**Figure 2.4a**). Based on the analysis of N_2 sorption isotherms using the BET method, the surface area of AP-MSNs was calculated to be 738.4 m^2/g. The pore size and pore volume of AP-MSNs were determined to be 2.3 nm and 1.30 cc/g, respectively according to the BJH method (**Figure 2.4b**).
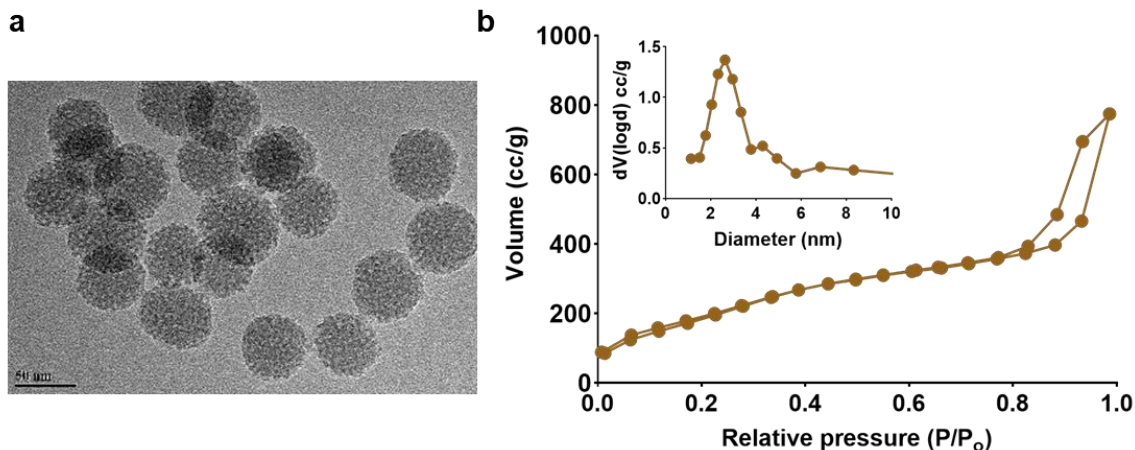
Figure 2.4. Structural characterization of AP-MSNs. **(a)** TEM image of AP-MSNs (Scale bar = 50 nm). **(b)** N_2 sorption isotherm and pore size distribution of AP-MSNs.

The D_h of MSNs was measured in the cell culture media supplemented with serum and the surface charge in PBS (1 mM). The AP-MSNs exhibited D_h of 118 ± 13 nm, which is higher than the solid diameter observed with TEM (**Figure 2.4a**), most likely due to the protein corona formation by the proteins present in cell culture media. The surface charge of AP-MSNs was observed to be negative (-31.2 mV), which can be attributed to the silanol groups on the surface of the MSNs. This also corroborated that the AP functional groups are localized to the inner walls of the MSNs. The TGA data showed that AP-MSN material contains 8.8 wt % organic content, which is attributed to AP functional groups grafted in MSNs.

After conjugation of AP-MSNs with cisPt prodrug, the amount of cisPt loaded was 5.13 ± 0.9 wt% (n=5) as determined by AAS. In addition, the D_h of cisPt-MSNs slightly increased to 134 ± 3 nm with minimal variation in the surface charge (-33 mV) (**Figure 2.5b and Table 2.2**). The organic content of cisPt-MSNs increased to 11.2 wt% based on the TGA. Next, the post-grafting modification of cisPt-MSNs were carried out to add phosphonate groups. The phosphonate groups on the surface of MSNs impart

overall negative charge, which is used for the coating with PEI polymer through electrostatic interactions. PEI-cisPt-MSNs showed an increase in zeta potential (+30.2 mV) and D_h (454 ± 3 nm). The PEI coating caused slight aggregation of the nanoparticles, which resulted in an increase in the D_h. The amount of PEI on the surface of MSNs was determined using the ninhydrin assay which showed 137 ± 25 µg of PEI per mg of MSNs. This is equivalent to 1.1 ± 0.2 µmoles of NH_2 available per mg of MSNs, according to the ninhydrin test. Importantly, PEI acts as a backbone for the chemical conjugation of Gem prodrug and enhance the endosomal escape of nanoparticles via proton sponge effect (177).
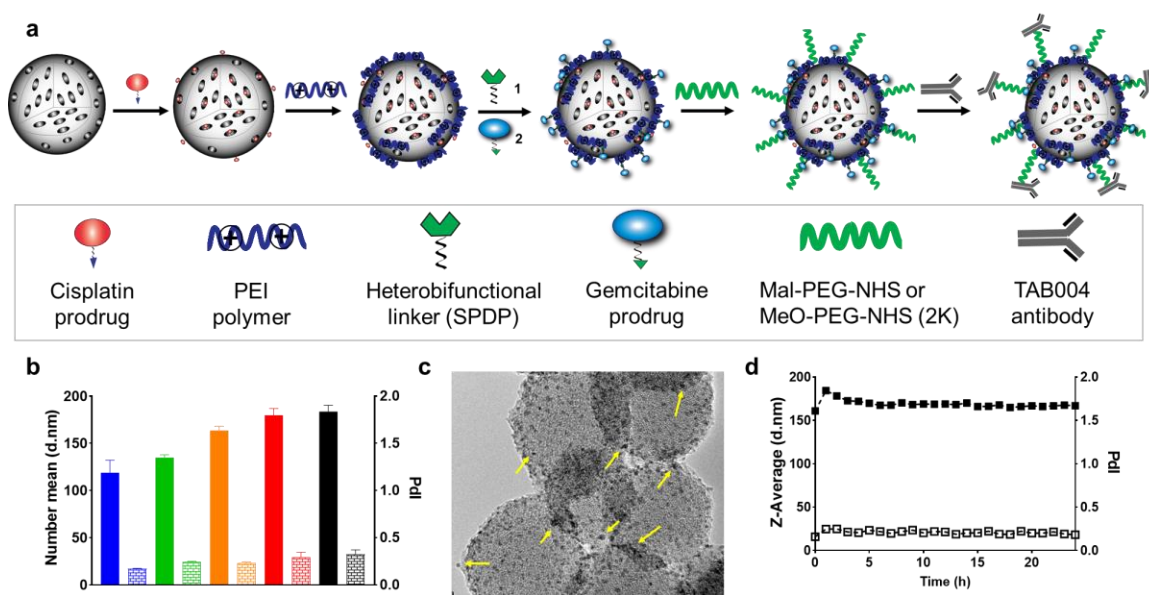
Figure 2.5. Physicochemical characterization of TAB004-Gem-cis-MSNs. **(a)** Schematic representation of the multistep procedure followed for the synthesis of TAB004-Gem-cispt-MSNs. **(b)** Hydrodynamic sizes (D_h) and polydispersity index (PdI) of AP-MSNs (blue), cisPt-MSNs (green), Gem-cisPt-MSNs (orange), PEG-Gem-cisPt-MSNs (red), and TAB004-Gem-cisPt-MSNs (black) in complete media supplemented with serum. Data represents the mean ± SD of three independent experiments. **(c)** TEM image of TAB004-Gem-cisPt-MSNs with negative staining to visualize the functionalized antibody (yellow arrows). **(d)** Colloidal stability of TAB004-Gem-cisPt-MSNs in complete cell culture media supplemented with serum for 24 h depicted by consistent Z-average (solid black squares) and PdI (hollow black squares) for 24 h using DLS.

The chemical conjugation of Gem prodrug to PEI-cisPt-MSNs resulted in a drug

loading of 23.9 ± 2.6 wt% (n=5). Gem-cisPt-MSNs showed a further increase in the D_h (162 ± 4 nm) with a surface charge of (24.3 mV). Gem-cisPt-MSNs were chemically modified with PEG polymer (MW=2 KDa). This material showed a slight increase in the D_h (179 ± 7 nm) with no significant change in the surface charge (24.0 mV) (**Figure 2.5b and Table 2.2**). The organic content of PEG-Gem-cisPt-MSNs further increased to 29.4 wt%. In addition, the quantification of amount of PEG coupled to MSNs resulted in approximately 0.23 μmol of PEG per mg of Gem-cisPt-MSNs. Finally, Gem-cisPt-MSNs were functionalized with the TAB004 antibody. The amount of antibody chemically attached to the surface of MSNs was 5.7 - 9.2 μg of antibody per mg MSNs, which accounts for 3-5 molecules of TAB004 antibody per nanoparticle. TAB004-Gem-cisPt-MSNs exhibited a D_h of 184 ± 6 nm. To corroborate the presence of antibody, TEM was used after negative staining of the samples. TEM images of TAB004-Gem-cisPt-MSNs confirmed the presence of the TAB004 antibody (**Figure 2.5c**). Colloidal stability of the TAB004-Gem-cisPt-MSNs was also investigated using DLS. The material was colloidally stable over a period of 24 h in cell culture media supplemented with FBS as depicted by the consistent D_h and PdI values (**Figure 2.5d**).

Table 2.2. Structural properties of MSNs.

Material	DLS Size (d, nm) (n=5)	ζ- potential (mV) (n=5)	Organic content (% wt.)/TGA (n = 3)	Drug content (% wt.) (Gem/cisPt)
AP-MSNs	118 ± 13	-31.3	8.8	NA
cisPt-MSNs	134 ± 3	-33	11.2	5.1 ± 0.9
PEI-cisPt-MSNs	454 ± 3	30.2	23.7	5.1 ± 0.9
Gem-cisPt-MSNs	164 ± 4	24.3	26.6	$23.9 \pm 2.6/$ 5.1 ± 0.9
PEG-Gem-cisPt-MSNs	179 ± 7	24.0	29.41	$23.9 \pm 2.6/$ 5.1 ± 0.9
TAB004-Gem-cisPt-MSNs	184 ± 6		-	5.7-9.2 ug of TAB004 per mg MSN

Overall, as envisioned, the stepwise process resulted in highly efficient drug conjugation with cisPt confined to the inner pores of the MSNs and Gem conjugated to the external surface with redox-responsive linkages. Our stepwise procedure provided high drug loading of two drugs with different physiochemical properties, and batch-to-batch consistency. Besides, the chemical conjugation imparts stimuli-responsive drug delivery. The cisPt prodrug conjugation results in the release of cisPt under the reductive conditions present in cancer cells, as demonstrated by our group and others (161). Gem conjugation results in two cleavable linkages a) aromatic amide and b) disulfide linkage. The aromatic amide can undergo hydrolytic cleavage to release free Gem. The disulfide linkage releases the Gem-SH, which has shown toxic effects compared to free Gem by previous reports (162, 178). It is worth pointing that our novel synthetic procedure of spatial localization of cisPt and Gem in the interior and exterior surfaces of MSNs, respectively intrigued the question of *in situ* delay in the release of two drugs. As Gem is on the external surface of the MSNs, the disulfide bonds are easier to break and release

the Gem in cells. Hence, we are currently exploring the drug release under reductive environment and reduced pH to test this hypothesis.

2.3.4 *In vitro* cytotoxicity of Gem-cisPt-MSNs.

After the successful synthesis and thorough characterization, we evaluated the *in vitro* cytotoxicity of our nanoplatform. Our investigations were based on the hypothesis that co-delivery of Gem/cisPt using a single nanocarrier will improve their drug delivery and therapeutic performance; due to the spatiotemporal controlled release of Gem/cisPt in cancer cells, which would not be possible with drugs physically loaded in nanocarriers or each drug conjugated of two different nanocarriers. In order to prove our hypothesis, we synthesized and used control MSN materials accordingly.

The cytotoxicity of Gem-cisPt-MSNs was evaluated in a panel of PDAC cells, including KCM, AsPC1, HPAF II, and Capan-1. The following materials were used as controls: PEI-MSNs, MSNs conjugated with single drugs (cisPt-MSNs or Gem-MSNs) or the physical mixture of Gem-MSNs plus cisPt-MSNs (see details in **Table 2.1**). No cytotoxicity was observed from the treatment of PEI-MSNs in any PDAC cells at the tested concentrations (1-100 µg/mL) (**Figure 2.6a**). Cell viability analysis after treatment with increasing doses of MSNs were assessed. Dose-response curves and the mean concentration required for 50% growth inhibition (IC_{50}) was determined for each cell line after 48 h treatment with each MSN material (**Table 2.3**).
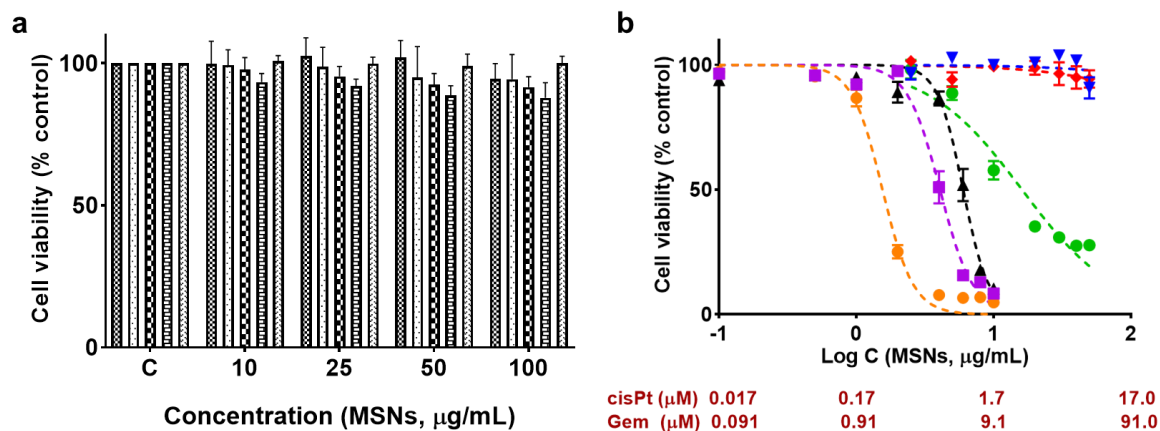
Figure 2.6. *In vitro* cytotoxicity analysis of Gem-cisPt-MSNs **(a)** Cell viability analysis showing the biocompatibility and safety of PEI-MSN in PDAC cells at various concentrations for KCM (dots pattern), HPAF II (brick pattern), Capan-1 (small checkered pattern), AsPC1 (large checkered pattern), and HPDE (heart pattern). Data represents the mean ± SD of three independent experiments. **(b)** Dose-response curve for KCM cells treated with various MSN materials; AP-MSNs (blue), PEI-MSNs (red), cisPt-MSNs (green), Gem-MSNs (purple), Gem-cisPt-MSNs (orange) and the physical mixture of Gem-MSNs plus cisPt-MSNs (black). Data represents the mean ± SD of three independent experiments.

The cytotoxicity data as depicted in **Figure 2.6b and Table 2.3**, demonstrate that Gem-cisPt-MSNs treatment led to higher cytotoxic effects in KCM cells compared to Gem-MSNs or cisPt-MSNs. Specifically, the concentration of drugs required to kill 50% of KCM cells was reduced to 1.46/0.27 (Gem/cisPt, μM) when the cells were treated with Gem-cisPt-MSNs compared to 3.2 μM (Gem) and 2.7 μM (cisPt) when treated with Gem-MSNs and cisPt-MSNs, respectively. Interestingly, the cytotoxicity of Gem-cisPt-MSNs was higher (about 3.5 times) than the physical mixture of Gem-MSNs plus cisPt-MSNs (IC_{50} = 6.18 (5.20/0.98)) (**Figure 2.6b**).

Since PDAC is a highly heterogeneous cancer, we investigated the cytotoxicity of Gem-cisPt-MSNs in additional PDAC cells, including AsPC1, Capan-1, and HPAF II cells to confirm the observation made in KCM cells. Indeed, as with KCM cells, Gem-cisPt-MSNs treatment caused higher cytotoxicity in all PDAC cells, compared to the control materials (**Table 2.3**). Results highlight that Gem-cisPt-MSNs exhibit 2.5-3.0 fold

lower IC_{50} values when compared to the IC_{50} values of the physical mixture of Gem-MSNs plus cisPt-MSNs (**Table 2.3**).

Table 2.3. Cytotoxicity data for cisPt-MSNs, Gem-MSNs, Gem-cisPt-MSNs, and physical mixture of Gem-MSNs plus cisPt-MSNs in a panel of PDAC cells. Cytotoxicity data is reported as IC_{50} values in terms of drug concentrations, where a=Gem, b=cisPt, and a/b =Gem/cisPt (µM).

Cells	cisPt-MSN (µM)[b]	Gem-MSN (µM)[a]	Gem-cisPt-MSN (µM)[a/b]	Gem-MSN + cisPt-MSN (µM) [a/b]
KCM	2.73	**3.21**	**1.73** (1.46/0.27)	**6.18** (5.20/0.98)
AsPC1	>17.0	**10.74**	**5.11** (4.30/0.81)	**13.0** (10.95/2.05)
HPAF II	>17.0	**15.76**	**9.56** (8.05/1.51)	**28.27** (23.81/4.46)
Capan 1	>17.0	**48.62**	**23.85** (20.08/3.76)	**62.82** (52.90/9.92)

We also synthesized control material where the Gem/cisPt drugs were physically encapsulated into the MSNs (PL-Gem-cisPt-MSNs). The characterization of the material showed very low drug loading (<2.0 wt%). Upon cytotoxic evaluation in KCM cells, we observed 35% decrease in cell viability even at high concentration of 100 µg/mL of PL-Gem-cisPt-MSNs.

Collectively, the *in vitro* cytotoxicity results demonstrated that firstly the synergy of Gem/cisPt combination remains intact when the drugs are conjugated to MSNs at the ratio of 5.3 ± 0.8, in the window determined from the CI studies. Secondly, the chemical conjugation of dual drugs Gem/cisPt improved drug loading and dramatically increased their *in vitro* performance compared to physical encapsulation method. Thirdly, we were able to demonstrate that dual-drug conjugated MSNs performed highly compared to single-drug conjugated MSNs and their physical mixture. In light of the data above, we believe that multiple drugs conjugated to the same nanocarrier are delivered into the cells

at same time and space (spatiotemporal release) and this controlled drug delivery while maintaining the specific ratio dramatically improves the combination therapy.

2.3.5 Mechanisms involved in Gem-cisPt-MSNs cytotoxicity in PDAC cells.

Though Gem/cisPt combination has been evaluated previously for PDAC and continue to be evaluated in various clinical trials currently, the mechanistic evaluation of Gem/cisPt combination in PDAC cells has never been reported to the best of our knowledge. Hence, we sought out to investigate the mechanism involved in the therapeutic performance of Gem-cisPt-MSNs, provoked by the remarkable cellular cytotoxicity observed. Since, Gem and cisPt are both DNA damaging agents; Gem is incorporated into the DNA as a deoxycytidine analog whereas cisPt forms intra-strand and inter-strand DNA crosslinks (176), the treatment of Gem-cisPt-MSNs causes DNA damage resulting from the controlled and synergistic delivery of Gem/cisPt. The DNA damage triggers a series of DNA damage response pathways (DDR), key signal transducers which determine the cell fate culminating in DNA damage repair or cell apoptosis (**Figure 2.7a**).

The rapid phosphorylation of the histone protein H2A.X at serine 139 near the DNA damage site, marks the early response for cells to DNA damage (179). Hence, we investigated the extent of DNA damage caused by Gem-cisPt-MSNs treatment using a FITC-labeled anti-Phos-H2A.X antibody. After treatment with Gem-cisPt-MSNs, KCM cells were highly phos-H2A.X positive (73.3 ± 3.8 %) and less phos-H2A.X positive when incubated with Gem-MSNs (37.3 ± 0.7 %) ($p<0.001$; **Figure 2.7b**). Interestingly, the incubation with mixture of cisPt-MSNs and Gem-MSNs led to even lower phos-H2A.X positive cells (27.3 ± 7 %).

Initiated by the cellular DNA damage, various relay markers participate in the cellular decision-making (or cell cycle regulators) including, replication protein A (RPA), checkpoint kinase 1/2 (ChK1/Chk2), and P53 which act as critical sensors at different stages to stop cell-cycle progression, determine cell fate depending of the level of damage and/or DNA-repair efficiency of the cells (180, 181). Hence, we evaluated the expression of DNA damage effectors like RPA, ATM/ATR-Chk1 using cell protein analysis. Based on the western blot studies, we observed increased RPA and Chk1P expression in the cells treated with Gem-cisPt-MSNs compared to the treatment with other materials. In addition, we also tested the level of DNA repair proteins in KCM cells after treatment with Gem-cisPt-MSNs, which did not show any increase compared to no treatment (**Figure 2.6b**).

In order to confirm if the increased DNA damage associated with Gem-cisPt-MSN treatment resulted in cell apoptosis, we evaluated the percentage of apoptotic cells using the Annexin V-FITC/PI double staining assay. The appearance of phosphatidylserine residues on the surface of the cell is an early event in apoptosis. Annexin V has a strong affinity for phosphatidylserine, and it is used as a probe for staining apoptotic cells (182). Propidium iodide (PI) is a cell impermeable nuclear dye that does not stain early apoptotic or live cells due to the intact membrane. However in late apoptosis and necrosis, the impermeability of the cell membrane is compromised, allowing PI to enter the cells and intercalate with the DNA (183). After the treatment of KCM cells with Gem-cisPt-MSNs and control MSN materials (see **Table 2.1**), the highest percent of apoptotic cells were observed following treatment with Gem-cisPt-MSNs ($70 \pm 1.6\%$ apoptotic cells; $p<0.001$; **Figure 2.7d**). In comparison, less apoptotic

cells were detected following treatment with Gem-MSNs (24.6 ± 9.3% apoptotic cells).

Incubation with the physical mixture (cisPt-MSNs plus Gem-MSNs) led to significantly

less apoptotic cells (16.7 ± 7.2 %; p<0.001).
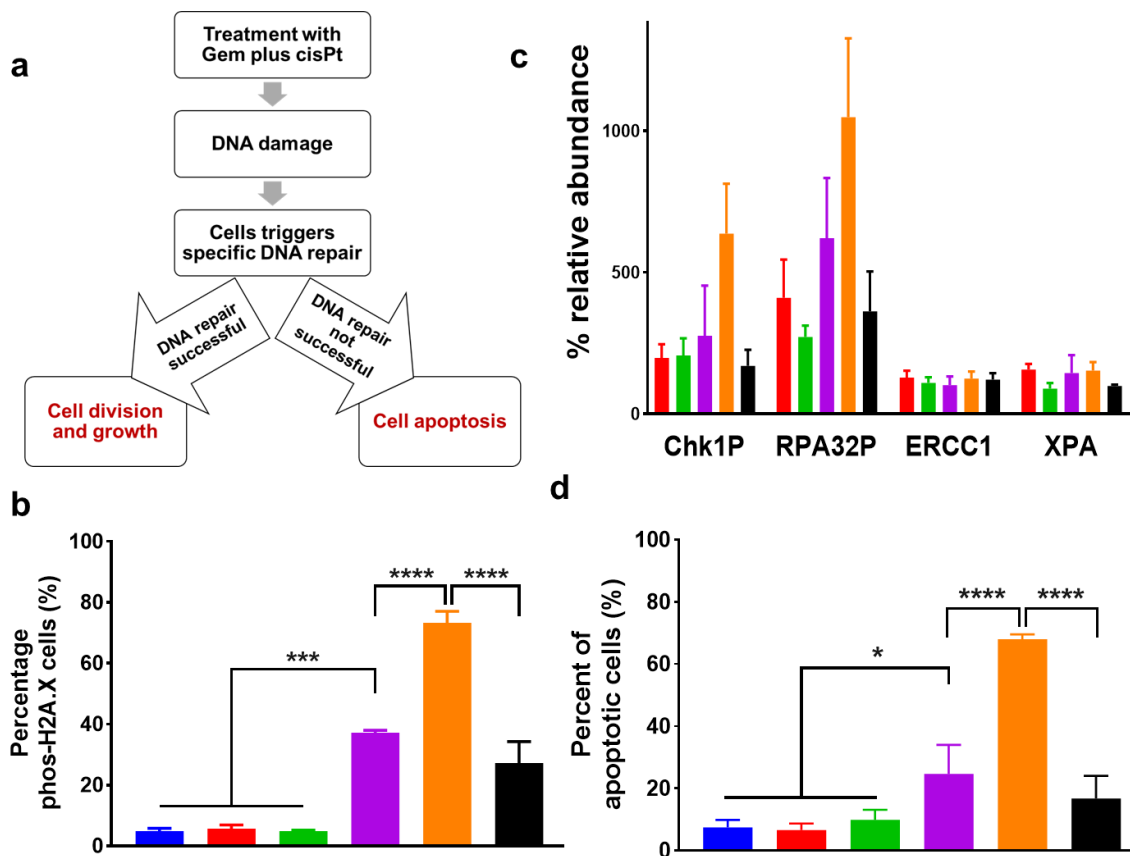
Figure 2.7. Mechanistic investigation of Gem-cisPt-MSNs. **(a)** Overview of the cellular events after the treatment with Gem-cisPt-MSNs. Percentage of Phos-H2A.X positive cells **(b),** expression of DDR markers (RPA and Chk1P) and repair proteins (ERCC1 and XPA) **(c),** and percentage of apoptotic cells **(c)** after KCM cells were treated with PEI-MSNs (red), cisPt-MSNs (green), Gem-MSNs (purple), Gem-cisPt-MSNs (orange) and physical mixture of Gem-MSNs plus cisPt-MSNs (black) and no treatment (blue).

From these mechanistic studies, we could confirm that the Gem-cisPt-MSNs

caused increased DNA damage as well as triggered the expression of effector proteins

including RPA and Chk1P in the DDR pathways. More importantly the DNA damage

and expression of relay markers culminated in the extensive apoptosis proving that the

cellular machinery failed to repair the DNA damage most likely due to the high levels of

damage and/or ineffective repair.

Our analysis still lacks some of the aspects required to fully understand the performance of Gem-cisPt-MSNs. It is documented that the synergy between Gem/cisPt is due to the capacity of Gem to inhibit the repair of cisPt adducts via multiple actions. Primarily, by the inhibition of RRM1 enzyme which is responsible for maintaining/synthesizing the dNTP pool in the cells required for DNA synthesis and repair (148). Evidence also suggests that Gem prevents the repair of cisPt-induced DNA damage by incorporating into cisPt induced adduct repair patch. These preceding roles of Gem in the Gem/cisPt combination lead to decreased Pt-adduct repair and increased Pt-adduct formation in the cells. Hence, our future experiments evaluating the expression of RRM1 and Pt-adduct formation after Gem-cisPt-MSN treatment in comparison to the effect of single drug-conjugated MSN and their physical mixture, would provide deeper and complete understanding of the therapeutic performance of our platform.

2.3.6 Targeted cytotoxicity and specificity of TAB004-Gem-cisPt-MSNs.

The specific accumulation of TAB004-MSNs in tMUC1 expressing PDAC cells, KCM and HPAF II were evaluated using flow cytometry and confocal microscopy. The cellular internalization data obtained demonstrated higher cellular uptake in cells treated with TAB004-MSNs compared to the PEG-MSNs (see **Figures 4.3 and 4.4**). In addition, the specificity of the TAB004-MSNs to recognize tMUC1 was evaluated by determining their differential uptake in KCM and KCKO cells. KCM cells express human tMUC1 whereas KCKO cells lack the tMUC1 expression (140). The cellular uptake data demonstrate that the TAB004-MSNs were taken up by the KCM cells at increased levels compared to the KCKO cells. Hence, the increased cellular uptake of TAB004-MSNs in

tMUC-expressing PDAC cells is attributed to the receptor-mediated endocytosis due to the specific interaction of TAB004 with tMUC1 on the cell surface (184).

Further, we investigated the benefit of TAB004 functionalization on the cytotoxicity in PDAC cells; KCM and HPAF II cells. Normal pancreatic ductal cells HPDE cells were used as control to gauge the safety of our platform on the healthy tissue surrounding the tumors. As depicted in **Figure 2.8**, TAB004-Gem-cisPt-MSNs led to increased cytotoxicity in both KCM and HPAF II cells, when compared to untargeted PEG-Gem-cisPt-MSNs. The IC_{50} of targeted nanoparticles was approximately 2-fold lower compared to that of untargeted nanoparticles. This data strongly suggest that the targeted MSNs selectively interact with the tMUC1 expressed on the PDAC cells leading to increased cellular uptake and their increased cytotoxicity in tMUC1 expressing PDAC cells. Notably, very low cytotoxicity was observed in the normal pancreatic ductal cells HPDE following treatment with either TAB004-Gem-cisPt-MSNs and PEG-Gem-cisPt-MSNs (**Figure 2.8a**). This may reflect the well-established higher cellular uptake of nanoparticles by cancerous cells compared to non-cancerous cells due to cancer cells higher metabolism and cell division rate (185).

Cell line	PEG-Gem-cisPt-MSN, μg/mL (Gem/cisPt, μM)	TAB004-Gem-cisPt-MSN, μg/mL (Gem/cisPt, μM)
KCM	6.4 (5.8/1.1)	**3.8** (3.4/0.65)
HPAF II	10.4 (9.5/1.8)	**4.8** (4.4/0.8)
HPDE	> 100 (91.2/17.0)	> 100 (91.2/17.0)
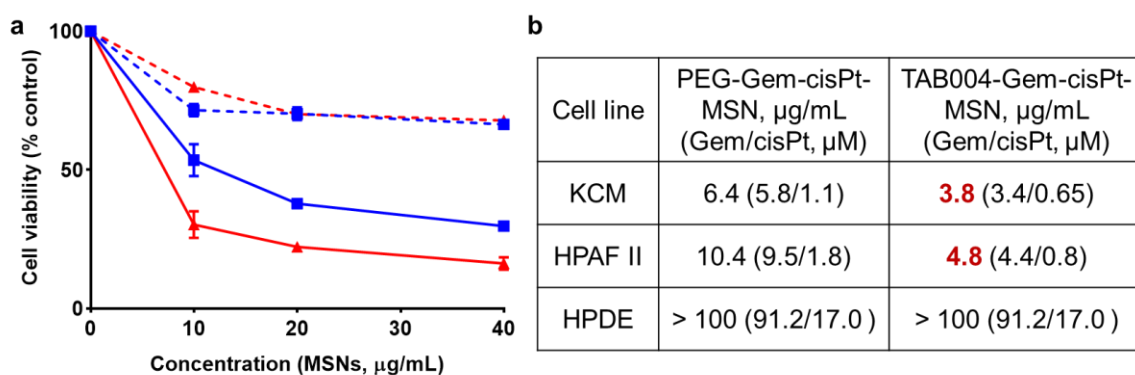
Figure 2.8. Targeted cytotoxicity and specificity of TAB004-Gem-cisPt-MSNs. **(a)** Cytotoxicity data of HPAF II (solid lines) and HPDE cells (dotted lines) when treated with TAB004-Gem-

cisPt-MSNs (red) and PEG-Gem-cisPt-MSNs (blue). **(b)** IC_{50} data obtained from KCM, HPAF II, and HPDE cells treated with TAB004-Gem-cisPt-MSNs and PEG-Gem-cisPt-MSNs.

2.3.7 *In vivo* targeting ability of TAB004-Gem-cisPt-MSNs in the syngeneic KCM mouse model.

KCM cells derived from PDA.MUC1 mice were used for establishing the syngeneic mice model (170). This model provides the advantage of using immune-competent mice allowing the evaluation of nanoparticle circulation, tumor accumulation and efficacy without neglecting the essential roles of the immune system in tumor progression (186). In addition, the KCM cells express human tMUC1 which are an ideal tumor model for the TAB004 targeted delivery of nanoparticles. Hence, the syngeneic KCM mice were used as a primary model for targeting and therapeutic efficacy studies of TAB004-Gem-cisPt-MSNs.

The enhanced accumulation of the active targeted nanoparticles in tumors is key to therapeutic efficacy. The ability of the TAB004-Gem-cisPt-MSNs to target KCM tumors was assessed following one-time intravenous injection of 40 mg/kg NIR-labeled material: TAB004-Gem-cisPt-MSNs or PEG-Gem-cisPt-MSNs. The MSN materials were injected 7 days post cell-implantation in KCM syngeneic mice (i.e., when the tumors reached approximately reached 100 mm^3). The presence of NIR fluorescence was detected using the IVIS imaging system prior to material injections and 30 min, 1 h, 4 h, 24 h, 48 and 96 h post-injection (**Figure 2.9a**). The data indicate an increase in the NIR-signaling intensity at the tumor site for the mice administered with TAB004-Gem-cisPt-MSNs compared to the control mice injected with PEG-Gem-cisPt-MSNs (**Figure 2.9b**).

The mice were euthanized 96 h post-injection, and organs including tumors were excised. The *ex vivo* fluorescence associated with tumors was quantified using the ROI

tool of the Living Image® software. Higher NIR signaling intensity in tumors injected with TAB004-Gem-cisPt-MSNs is observed in comparison to the PEG-Gem-cisPt-MSNs (**Figure 2.9c**). To corroborate the enhanced accumulation of TAB004-Gem-cisPt-MSNs in the tumors, Si content was determined after tumor digestion. Inductively coupled plasma optical emission spectroscopy (ICP-OES) was used for the quantification of Si content. **Figure 2.9d** highlights a significant increase in the Si content (0.26 mg/g of tissue) for the tumors of mice treated with TAB004-Gem-cisPt-MSNs as compared to the tumors of mice treated with PEG-Gem-cisPt-MSNs (0.12 mg/g; $p<0.05$). Taken together, these result underline that the functionalization of MSNs with the TAB004 antibody, enhanced the accumulation of the nanoparticles in tumor tissue (163).
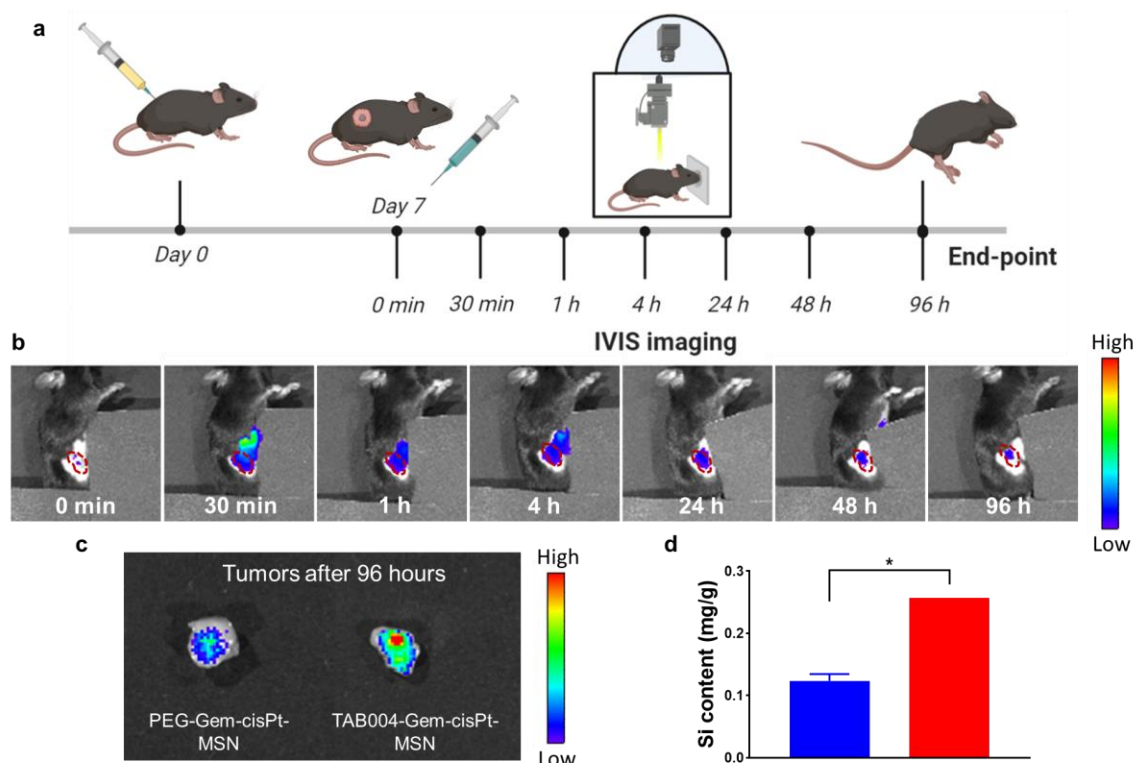
Figure 2.9. *In vivo* targeting of TAB004-Gem-cisPt-MSNs in syngeneic KCM mice. **(a)** IVIS images of mice at 0 min, 30 min, 1 h, 4 h, 24 h, 48 h, and 96 h after mice were injected with TAB004-Gem-cisPt-MSNs (region outlined in red denotes the tumor). **(b)** NIR fluorescence images of tumors harvested from mice 96 h after injected with TAB004-Gem-cisPt-MSNs

compared to PEG-Gem-cisPt-MSNs. **(c)** Si content analysis in tumors from mice injected with TAB004-Gem-MSNs (green) and PEG-Gem-cisPt-MSNs (red).

2.3.8 *In vivo* therapeutic efficacy of TAB004-Gem-cisPt-MSNs in syngeneic KCM mice.

To evaluate the therapeutic efficacy of TAB004-Gem-cisPt-MSNs in syngeneic KCM mice, four experimental treatment groups were assessed; PBS, Free Gem/cisPt, PEG-Gem-cisPt-MSNs, and TAB004-Gem-cisPt-MSNs. Briefly, KCM tumor-bearing mice received intravenous injections of MSN materials or free Gem/cisPt at a concentration of 40 mg/Kg or the equivalent drug dose of 9.52 mg Gem and 2.05 mg cisPt per Kg. The treatment started 7 days after the implantation of 10^6 KCM cells, i.e., the tumors reached approximately 100 mm^3. Injections were repeated every 4 days for a total of 6 injections (**Figure 2.10a**).

Tumor growth was measured throughout the treatment, and the tumor volume was calculated and plotted to evaluate the therapeutic benefit of the treatment groups tested. TAB004-Gem-cisPt-MSNs injections led significant tumor growth inhibition compared to the PBS group (p<0.0001), free Gem/cisPt (p<0.0001) and untargeted PEG-Gem-cisPt-MSNs (p<0.05; **Figure 2.10b**). Moreover, PEG-Gem-cisPt-MSNs injections led to a therapeutic improvement when compared to free Gem/cisPt injections. At the end-point, mice were euthanized and the tumors were excised. Tumor weights were measured and confirmed the improved therapeutic efficacy of the TAB004-Gem-cisPt-MSNs treatment when compared the other treatment groups (**Figure 2.10c**). The KCM tumors in mice treated with TAB-Gem-cisPt-MSNs showed 79% tumor inhibition compared to the PBS group whereas 58% in PEG-Gem-cisPt-MSNs group and 15% in free drugs group. Tumor tissues after treatment were assessed for apoptotic cells using an *in-situ* apoptosis

assay. Tumors collected from mice treated with TAB004-Gem-cisPt-MSNs contained an increased amount of apoptotic cells compared to the tumors collected from the other groups tested (**Figure 2.10d**). The enhanced therapeutic ability of the TAB004-Gem-cisPt-MSNs treatment was confirmed by an increased inhibition of tumor growth and increased apoptosis in tumors when compared to the control groups, PEG-Gem-cisPt-MSNs and free Gem/cisPt.
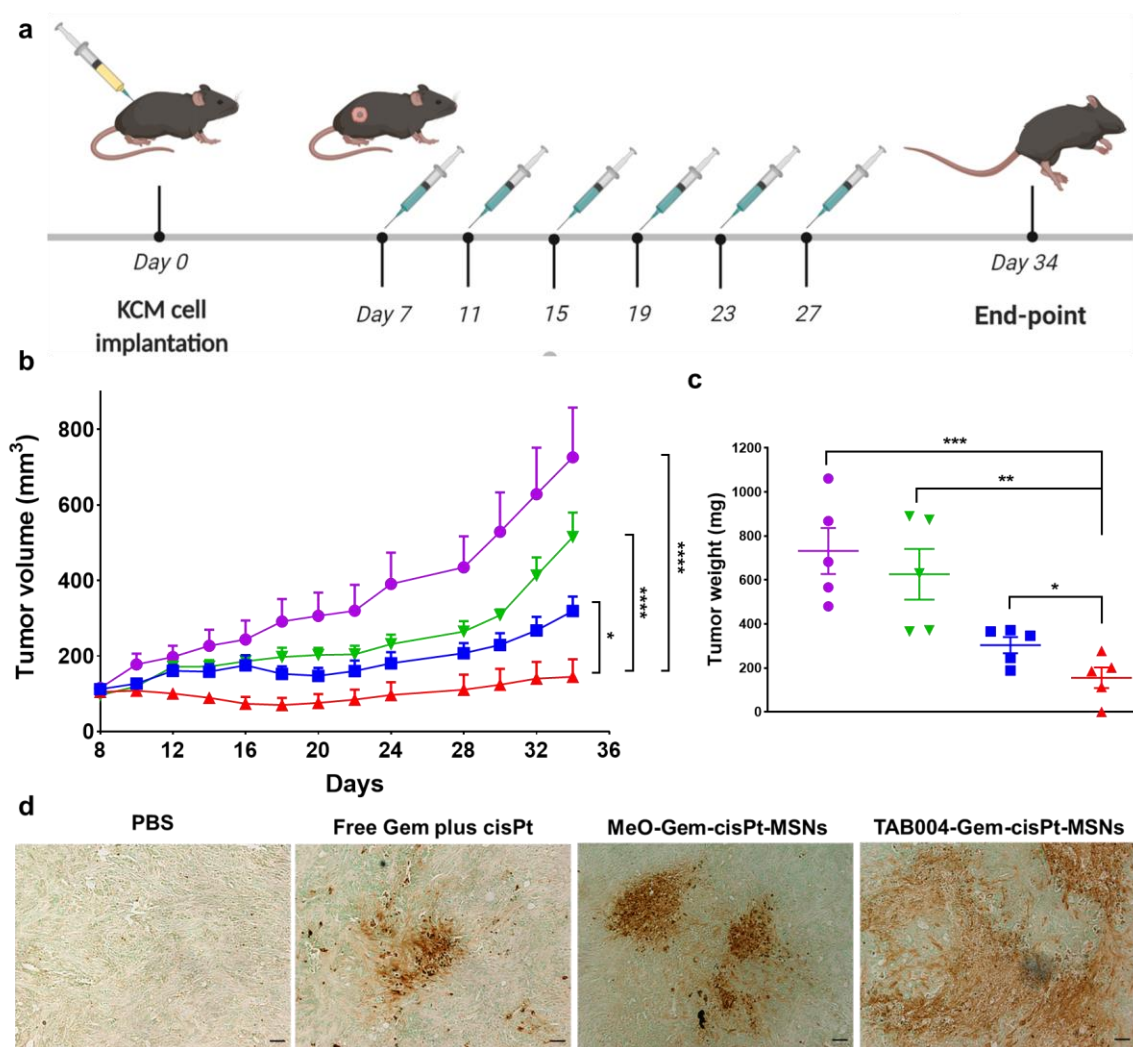
Figure 2.10. *In vivo* therapeutic efficacy in syngeneic KCM mice; **(a)** Schematic representation of the treatment regimen; mice were injected with MSN materials or free drugs 6 times with 4 days interval between the injections. **(b)** Tumor volume measurement throughout the study with various treatment groups: PBS (purple circles), Free Gem/cisPt (green downward triangles), PEG-Gem-cisPt-MSNs (blue squares), and TAB004-Gem-cisPt-MSNs (red upward triangles)

(n=5 mice per group). Two-way ANOVA was performed between different groups and time points to determine the statistical difference. **(c)** Tumor weights measured at the endpoint of the efficacy studies: PBS (purple circles), Free Gem/cisPt (green downward triangles), PEG-Gem-cisPt-MSNs (blue squares), and TAB004-Gem-cisPt-MSNs (red upward triangles) (n=5 mice per group). t-test was performed between different groups to determine the statistical difference. **(d)** *Ex vivo* analysis of tumor sections shows the apoptotic cells in the tumors after treatment. Scale bar = 100 µm. Statistics: ****p≤0.0001, ***p≤0.001, ** *p*≤0.01, * *p*≤0.05 and not significant (ns) *p*>0.05.

2.3.9 *In vivo* biodistribution and safety of TAB004-Gem-cisPt-MSNs in syngeneic KCM mice.

The safety of nanomaterials is essential for their clinical advancement. As all nanocarriers are taken up by the MPS system for their clearance, the nanomaterials usually accumulate in major organs like liver and spleen. Nevertheless, it is crucial that the nanocarriers are safe or well tolerated by the healthy organs. MSNs' safety and biocompatibility has been shown by our group and others (163). Herein, we investigated the safety and biodistribution of TAB004-Gem-cisPt-MSNs and control groups. At the end-point, major organs such as the liver, lungs, kidneys, spleen, and heart were harvested. The *ex vivo* NIR fluorescence associated with each organ was imaged using the IVIS imaging system. The fluorescence intensity was quantified to determine the accumulation of MSNs. The NIR fluorescence signal analysis (per g of tissue) showed that both targeted and untargeted MSN materials were distributed in spleen followed by lungs and liver (**Figure 2.11a and 2.11b**). This trend was confirmed by Si content analysis in the tissues (**Figure 2.11c**). Similar results have been reported and the accumulation is associated to the slow clearance from the hepatobiliary system.
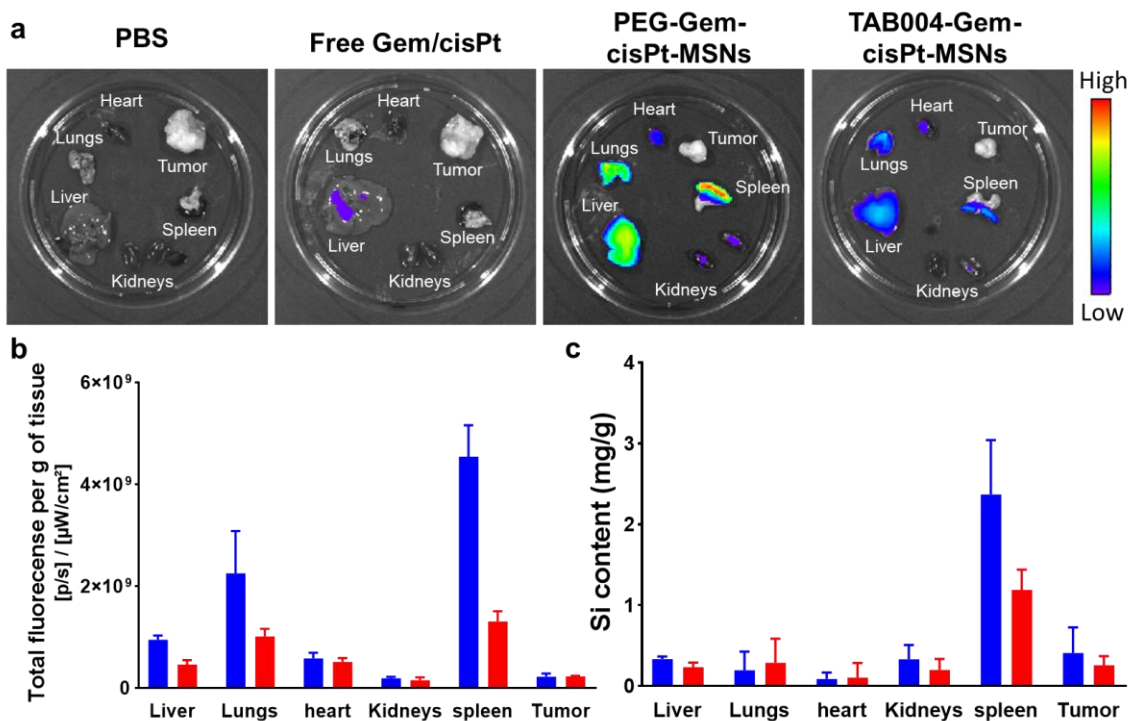
Figure 2.11. Post-treatment biodistribution and safety of TAB004-Gem-cisPt-MSNs. **(a)** Representative NIR fluorescent signals captured by IVIS Imaging system from differrent organs harvested from mice injected with PBS, free Gem/cisPt, PEG-Gem-cisPt-MSNs, and TAB004-Gem-MSNs. **(b)** NIR signaling intensity associated with major organs from mice injected with PEG-Gem-cisPt-MSNs (blue) and TAB004-Gem-MSNs (red) as analyzed using Living Image® 4.5.5. **(c)** Si content analysis in the digested tumor samples from mice injected with PEG-Gem-cisPt-MSNs (blue) and TAB004-Gem-MSNs (red).

The biosafety of the MSNs was evaluated based on the bodyweight measurements during the treatment and histopathological investigation of the organs. The mice's behavior and body weights were monitored throughout the treatment which was used as a primary parameter to determine if the material shows any adverse effects. No significant changes in body weights were observed in any treatment groups. Moreover, there was no behavioral changed noted during the treatment. The secondary parameter of tissue histopathological evaluation was used to investigate any tissue damage from the treatment. Histopathological analysis shows cellular changes in the tissue, which can be used as key signs of toxicity. Tissue samples from major organs were sectioned, fixed

and stained with H&E (**Figure 2.12**). No prominent features of toxicity or changes in the tissue sections was observed in the liver, kidneys, lungs, heart and spleen of mice treated with MSN materials (PEG- or TAB004-Gem-cisPt-MSNs) compared to the ones collected from the PBS group (**Figure 2.12**). These results show that the MSNs are biocompatible as reported in previous studies (187, 188).
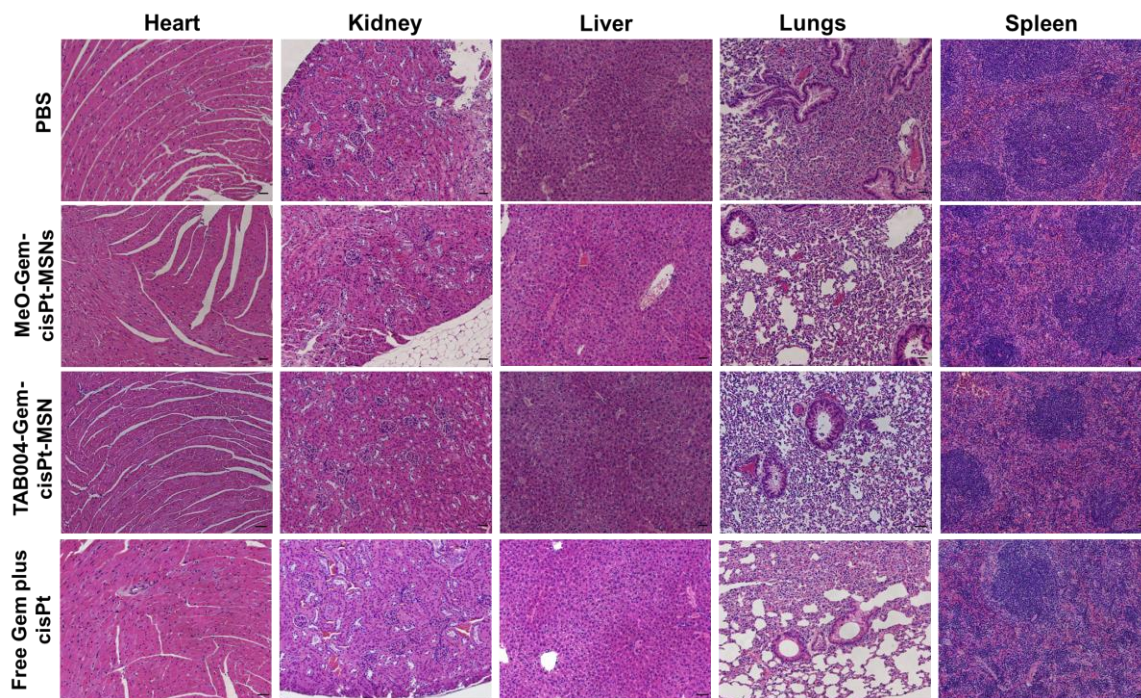
Figure 2.12. Histopathological analysis of the major organs including heart, kidney, liver, lungs and spleen harvested from the mice after the therapeutic treatment; PBS, free Gem/cisPt, PEG-Gem-cisPt-MSNs, and TAB004-Gem-cisPt-MSNs (scale bar= 100 μm).

Nevertheless, we observed distinct features in the kidney tissue associated with the mice treated with free drugs, showing obvious edema of the bowman's capsule (132) (**Figure 2.13a**). Blood serum analysis confirmed the toxicity associated with free drugs. The ratios of AST/ALT and BUN/creatinine, which are used as markers for the function of liver and kidneys, respectively, were analyzed. These values showed an increased ratio of AST/ALT and BUN/ creatinine in the mice treated with free drugs compared to TAB004-Gem-cisPt-MSNs and PEG-Gem-cisPt-MSNs groups (**Figure 2.13b and**

2.13c). The enhanced toxicity associated with free drugs could be due to the high drug (Pt) content in the kidney tissue (**Figure 2.13d**). The increased off-target toxicity of Gem and cisPt in liver and kidney is well-documented and is one of the major side effects of chemotherapy. The Pt analysis of liver and kidneys confirm that the MSN materials have a lower accumulation of cisPt compared to the free drugs. Importantly, the Pt detected in these organs is most likely still chemically conjugated to the nanoparticles which further reduced the potential toxic effect. This observation further proves that chemical conjugation is not only important for enhancing accumulation in the tumor tissue, but also can prevent off-target toxicities.
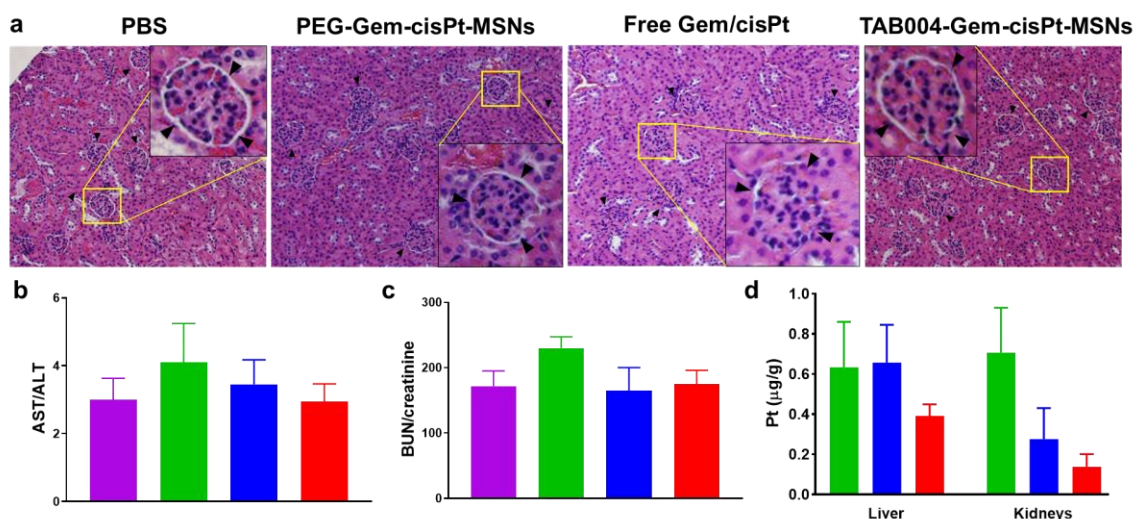
Figure 2.13. Blood serum and organ histology for the assessment of toxicity. **(a)** Histological analysis of kidney tissue sections showing the toxicity in different treatment groups. The bowman's capsule and edema are shown in the zoomed inset images. **(b)** blood serum markers (BUN/creatinine) of kidney function for different treatment groups. **(c)** blood serum markers (AST/ALT) of liver function for different treatment groups. **(d)** Pt content analysis in various organs after treatment groups. Treatment groups PBS (purple), free Gem/cisPt (green), PEG-Gem-cisPt-MSNs (red) and TAB004-gem-cisPt-MSNs (blue).

In light of *in vivo* targeting and therapeutic efficacy data obtained in KCM syngeneic mice, rational design of TAB004-Gem-cisPt-MSNs translated to its enhanced therapeutic performance in KCM syngeneic mice. Of note, administration of the both

MSN materials (TAB004-Gem-cisPt-MSNs and PEG-Gem-cisPt-MSNs) led to improved therapeutic efficacy compared to the free Gem/cisPt. This is attributed to the faster clearance of free drugs, whereas the drugs conjugated to MSNs have longer circulation and better homing in tumors. Though injected at the similar concentration and at the synergistic ratio, it is likely that the free drugs group did not reach the tumors at the same time or at the intended synergistic ratio due to the different physiological properties of Gem and cisPt. On the contrary, MSNs conjugated to Gem/cisPt lead to the spatiotemporal delivery of drugs independent of the physiological properties of the drugs loaded. Thus, the MSNs showed much better tumor inhibition due to controlled release of drugs at the tumor site.

Comparing the MSNs materials, the TAB004-Gem-cisPt-MSNs showed the best performance due to their increased accumulation in tumors owing to the targeting ability of TAB004 to interact with tMUC1 overexpressed on the KCM cells. Increased toxicity profile is another major drawback in conventional drug combination therapies. Our therapeutic and safety data clearly demonstrates the systemic toxicity encountered by free drug administration. Thus, proving that that our nanocarrier design with chemical conjugation of drugs is not only important for enhancing accumulation in the tumor tissue, but also can prevent off-target toxicities. This demonstrates that the controlled release of drugs from nanocarrier under tumor-specific stimuli can prevent the off-target toxicity.

Interestingly, we observed that PEG-Gem-cisPt-MSNs are retained in the organs in higher amounts compared to TAB004-Gem-cisPt-MSNs (**Figure 2.11**). While we lack a complete explanation for this observation, we hypothesize that despite the increased

tumor accumulation, TAB004 antibody on MSN surface can act as immune recognition agent and increase the clearance of TAB004-Gem-cisPt-MSNs. This needs further detailed investigation. The MSNs and drugs conjugated to MSNs are slowly cleared out over a period of weeks and longer PK studies are required to determine the long-term safety and clearance of our therapeutic nanoparticles.

2.3.10 *In vivo* therapeutic efficacy in GEM PDA.MUC1 mice.

Cell line-based models have predictive value, which helps to prioritize the biomarker selection, imaging, and/or therapeutic agents. However, cell line-based models lack genetic and phenotypic heterogeneity and hence, they limit the ability to predict the therapeutic responses in clinical settings (136). GEM models recapitulate the progression of PDAC disease in humans and are recognized as more accurate predictors of drug response and better models for biomarker and therapeutic discovery (138). Activating mutations in the KRAS proto-oncogene is a primary genetic disposition in PDAC. Transgenic mice have been established that express physiological levels of oncogenic KRAS where the glycine at codon 12 is substituted to aspartate in the progenitor cells of the mouse pancreas. These mice are designated as Cre-LSL-KRAS mice which develop a full spectrum of PDAC from the preinvasive lesions to invasive carcinoma and metastasis (189). Dr. Mukherjee's lab further crossed the LSL-KRAS^{G12D} with tamoxifen-inducible ^{P48}Cre to a human MUC1.Tg mice to generate the PDA.MUC1 mice. The triple transgenic mice develop preinvasive lesions and invasive PDA when the oncogenesis is initiated with tamoxifen.

The treatment of PDA.MUC1 mice started after 32 weeks of post-tamoxifen injection which is at advanced stages of PDA. TAB004-Gem-cisPt-MSNs were

intravenously injected to the PDAC.MUC1 mouse every 15 days for a period of three months, six injections total (**Figure 2.14a**). This regimen was designed as extended treatment procedure is needed to observe therapeutic efficacy based on the invasive PDA development in PDA.MUC1 mice (190). After the endpoint, tissue samples from the pancreas were evaluated to determine the therapeutic efficacy. Though we observed few high-grade lesions in the pancreas from both control and mice treated with nanoparticles, the extent of well-differentiated regions of invasive PDA was significantly less in treatment group (**Figure 2.14b**). Further, to localize MSNs in the PDA regions, we used confocal microscopy imaging in the H&E slides. The micrographs confirm that the nanoparticles are not only localized in the pancreas, but they are found at the invasive PDA regions (**Figure 2.14c**).

This very preliminary data, but promising results in a clinically relevant model, demonstrate the potential of our MSN therapeutic platform for PDAC treatment. Though robust, the studies in GEM models are long and do not offer an easier and time-based monitoring of the disease progression and response to the treatment. The only reliable measurement of the therapeutic performance is the end-point pancreas analysis to determine the stage and extent of PDA. Future experiments with increased number of PDA.MUC1 mice in the treatment group needs to be evaluated for detailed understanding of the therapeutic performance of our platform on the progression of PDA as well as metastasis.
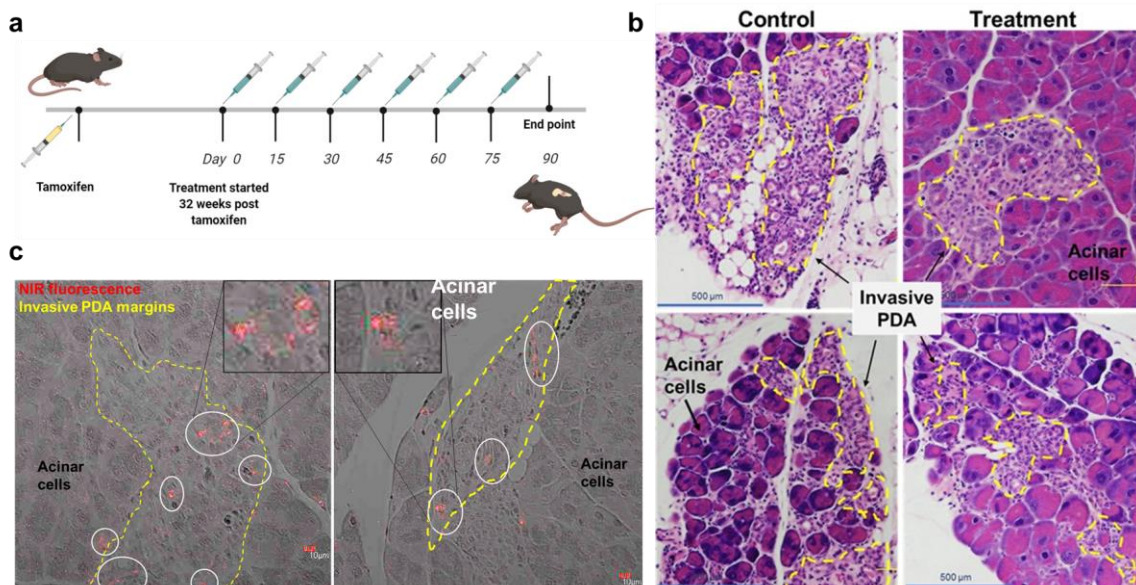
Figure 2.14. Therapeutic efficacy in GEM PDA.MUC1 mice model. **(a)** Schematic representation of the treatment regimen; mice were injected with TAB004-Gem-cisPt-MSNs 6 times with 15-days interval between the injections. **(b)** The pancreas from control and treated mice showed significantly less invasive PDA regions compared to the control (yellow margins represent the invasive PDA regions in the pancreas and the normal acinar cells in the pancreas are also labeled. **(b)** In addition, the pancreas tissue from the treated mice showed NIR fluorescence localized in the invasive PDA regions.

2.4 Conclusions.

Combination therapies have been investigated under preclinical and clinical settings to improve the drawbacks associated with Gem monotherapy. Nevertheless, traditional combination therapies are associated with issues including controlled spatiotemporal and ratiometric delivery due to the distinct physiochemical properties of the participating drugs, different cellular uptake mechanisms, and increased off-target toxicities. Nanoparticles, importantly MSNs provide an excellent opportunity to combat these limitations and exploit the full potential of combination therapies and impart further improvement in combination therapies.

Herein, we have designed and synthesized a novel target-specific, stimuli-responsive MSN-based nanocarrier for the co-delivery of Gem/cisPt. Our strategy takes

advantage of the structural features of MSNs to obtain high loading of Gem/cisPt at a synergistic ratio. Indeed, the chemical conjugation of drugs to MSNs offers batch-to-batch consistency, controlled and high drug loading, controlled release under specific stimuli and prevent systemic leakage of drugs. Through *in vitro* testing in a panel of PDAC cells, we demonstrated the increased cytotoxic effect of Gem-cisPt-MSNs compared to the single drug-conjugated MSNs (Gem-MSNs or cisPt-MSNs) and more importantly the physical mixture of Gem-MSNs plus cisPt-MSNs. An in-depth mechanistic study of the cytotoxic effect showed that the Gem-cisPt-MSNs caused increased DNA damage leading to an enhanced apoptosis in KCM cells, compared to the control materials. Moreover, the TAB004 functionalized Gem-cisPt-MSNs exhibited increased selective cytotoxicity in tMUC1 expressing KCM and HPAF II cells.

The targeting ability of TAB004-Gem-cisPt-MSNs was demonstrated through *in vivo* imaging and Si content analysis in KCM syngeneic mice. The excellent targeting ability of these nanocarriers increased the accumulation in tumors, which increased their therapeutic efficacy compared to non-targeted counterpart and free drugs. The MSNs minimized the side effects of the chemotherapy drugs based on the mice's body weight measurements and the histological analysis of organs revealed no signs of toxicity in the mice group treated with MSNs, whereas prominent features of toxicity were observed in the group treated with free drugs at the equivalent concentration. Overall, the targeting capacity of the TAB004-Gem-cisPt-MSN platform rendered higher tumor localization and increased therapeutic efficiency in a syngeneic model that overexpressed tMUC1. Moreover, the strategy of chemically attaching Gem and cisPt to MSNs dramatically reduced the toxicity of Gem and cisPt compared with the free drugs. The therapeutic

potential of TAB004-Gem-cisPt-MSNs was demonstrated in a clinically robust GEM PDA.MUC1 mice. These results are encouraging to move the MSN platform into clinical settings

In future, *in vivo* models including orthotopic and PDX models needs to be explored to understand the metastatic inhibiting capacity of our material. The Gem-cisPt-MSNs is an ideal system for or combining with PARP inhibitors which are the current focus in clinical trials due to the understanding of prevalent germline mutations observed in certain patients. PDX models from different patients with different levels of germline mutations can be used to realistically predict the applicability of our materials in combination with PARP inhibitors.

CHAPTER 3: CyP-MSNs and PEG-Gem-cisPt-MSNs sequential combination for tumor stroma modulation and improved drug delivery for PDAC.

3.1 INTRODUCTION

3.1.1 Role of tumor stroma in PDAC.

Extensive desmoplastic stroma is one of the primary contributors to the poor clinical prognosis of PDAC (28). Stroma accounts for more than 80% of PDAC tumor volume, where cancer cells exist in close interaction with noncancerous cellular components including cancer-associated fibroblasts (CAFs), pancreatic stellate cells (PSCs), numerous immune cells, and noncellular components of extracellular matrix including collagen, fibrinogen, and hyaluronan (HA) (**Figure 3.1**) (30, 191-194). Cancer cells and stroma change throughout the tumor growth, which is controlled by the cancer cell-stroma crosstalk. The stromal components, as well as the associated signaling pathways involved in the cancer cell-stroma crosstalk, play a vital role in tumorigenesis, progression, and metastasis (195).

The tumor stroma in PDAC is a main factor responsible for the therapy failure, and thus stroma modulation is hypothesized to improve PDAC therapy (27, 193, 196). Below are some of the main features of stroma that impact the performance of nanoparticles for PDAC treatment:

a. Stroma causes elevated interstitial fluid pressure (IFP) due to the compressed blood vessels and reduced blood flow.

b. Stroma acts as a physical barrier leading to poor perfusion of systemic drugs and presents a unique challenge to nanoparticles.

c. Off-target toxicity in stromal components like CAFs leads to increased resistance due to the cancer cell-stroma crosstalk.
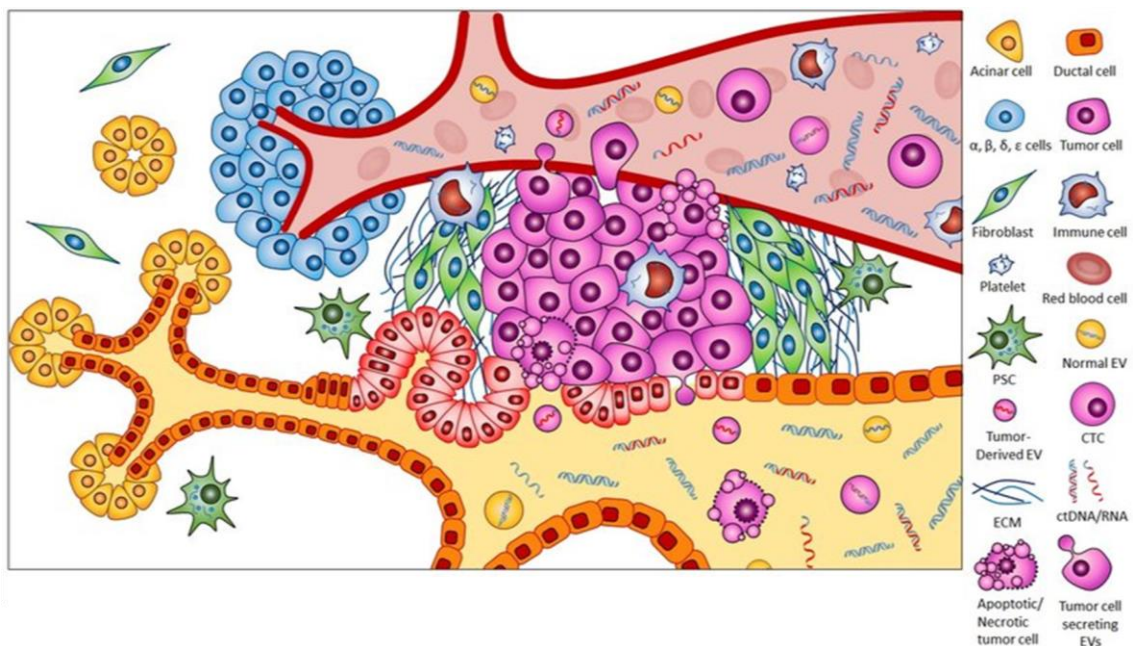
Figure 3.1. The complex tumor microenvironment (TME) in PDAC includes cellular and non-cellular components that are in constant interaction with cancer cells (197).

3.1.2 Role of the Sonic hedgehog pathway as a therapeutic target in PDAC.

3.1.2.1 Sonic hedgehog activation in PDAC.

Sonic hedgehog (SHh) pathway plays a critical role in the embryonic development of tissues (198). While mostly quiescent in the healthy pancreas, SHh is aberrantly activated during PDAC tumorigenesis. Importantly, the SHh pathway is extensively studied for its role in cancer cell-stroma crosstalk leading to dense stroma deposition (199). Among various components of the tumor stroma, CAFs and PSCs are reported to overexpress SHh receptors. These cells are considered to be the star players in extensive stroma production. Overexpression of SHh ligands and downstream markers like smoothened receptor (SMO), patched receptor (PTCH), glioma-associated oncogene homolog-1 (Gli-1) are related to poor prognosis of PDAC (200-202).

As depicted in **Figure 3.2**, during the SHh activation, the SHh ligand released from the cancer cells binds to the transmembrane protein receptor PTCH, which relieves smoothened (SMO) from the inhibitory effect of PTCH. Subsequently, SMO causes the translocation of Gli to the nucleus and activates several Gli-induced transcriptional effectors (203). The SHh pathway participates in both autocrine and paracrine functions, where the SHh ligands released by cancer cells act on the same cells and stromal cells, respectively (**Figure 3.2**). The paracrine activation leads to desmoplasia; whereas the autocrine activation leads to tumor cell proliferation and metastasis.
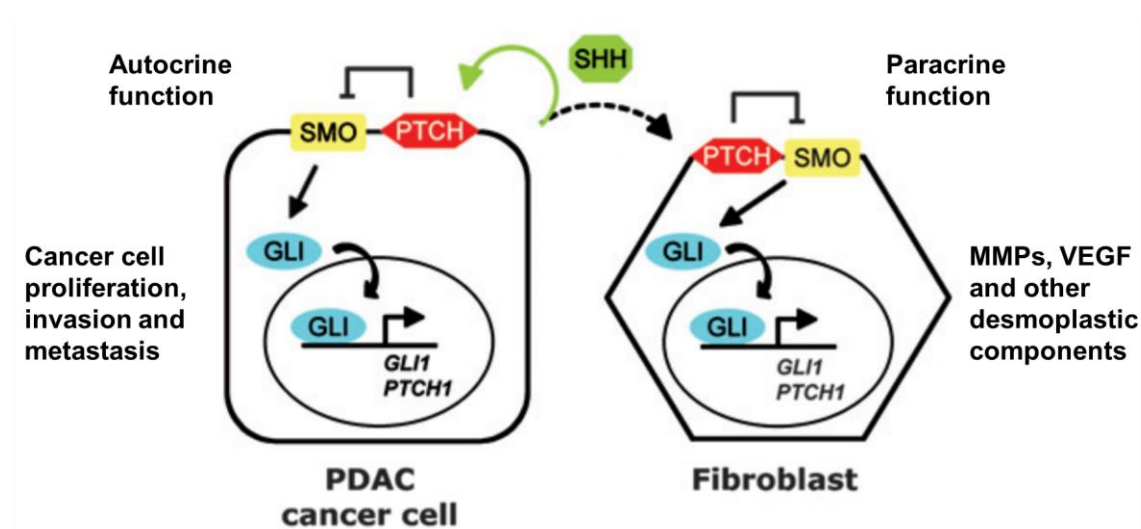
Figure 3.2. Sonic hedgehog pathway is one of the major molecular interactions between stromal cells and cancer cells (204). SHh ligand released from cancer cells acts on cancer cells (autocrine function) and stromal cells (paracrine function).

3.1.2.2 Sonic hedgehog is a promising target for stroma modulation in PDAC.

SHh pathway is the most studied mediator of stroma-cancer cell interaction and desmoplasia. It has been investigated as an important target for stromal remodeling in PDAC (202, 205, 206). Multiple preclinical studies have demonstrated that inhibition of SHh by small-molecule antagonists such as cyclopamine, vismodegib (GDC-0449) or IPI-926 results in suppression of cell proliferation, decreased stroma, and improved

chemotherapy (207, 208). These encouraging results led to multiple clinical trials where the SHh inhibitors were combined with chemotherapy (209). Unfortunately, these trials have been either negative or equivocal giving no survival benefit in comparison to chemotherapy alone. However, not much improvement in the therapeutic efficacy/overall survival has been observed under clinical settings (210, 211). For example, vismodegib was tested in phase II clinical trial in combination with Gem. The overall survival was similar for the combination and Gem alone at 6.9 months and 6.1 months (212).

Possible key considerations for the failure could be the imbalance in the bioavailability of SHh inhibitors at the tumor site, toxicity to the healthy organs, and catastrophic stromal depletion (213). Firstly, reducing SHh signaling promotes angiogenesis, the imbalance of epithelial and stromal elements might explain the clinical trial's setback. Secondly, the efficient and safe delivery of SHh inhibitors is an important issue to be considered to reduce the toxic side-effects and improve the bioavailability in the tumor site. In this direction, nanocarriers can potentially increase the targetability, the circulation of drugs and bioavailability in the tumor site.

Thirdly, recent in-depth investigation demonstrated that long-term, high doses of SHh inhibitors (>100 mg/kg daily) caused catastrophic consequences of excessive disruption of stroma, leading to increased tumor metastasis (214). These results highlighted the importance of preserving tumor-restraining functions of stroma and the need for fine-tuned remodeling of stroma during the PDAC therapy. Careful designing of the therapy regimen can provide the spatial and temporal access to the therapeutic target as well as avoid stromal depletion due to over SHh inhibition. In this regard, sequential delivery using nanocarriers could serve as the best strategy (154). Sequential combination

of chemotherapeutics and signaling pathway inhibitors using nanoparticles have been investigated to reduce the tumor resistance, alter TME and increase efficacy (123, 215).

3.1.2.3 Use of nanoparticles for the delivery of cyclopamine.

Cyclopamine (CyP) is a natural alkaloid, which acts on the SMO receptor to inhibit SHh signaling. CyP has been investigated in PDAC therapy and exhibits promising therapeutic effects. CyP treatment decreased the tumor stroma, facilitated the tumor delivery of drugs, decreased cancer stem cells, reversed chemoresistance in cancer cells, and increased efficiency of radiation (203, 216). More importantly, CyP treatment alleviated the IFP in the tumors, which significantly improved the delivery of nanoparticles (216). However, CyP is insoluble in water and shows systemic toxicity. The bioavailability of CyP can be improved while decreasing systemic toxicity using nanomaterial-based drug delivery systems. In this direction, CyP has been encapsulated in polymeric nanoparticles and micelles (217, 218).

3.1.3 Hypothesis and aims of the present study.

We hypothesized that using MSNs as the main delivery system for a sequential treatment using cyclopamine followed by Gem/cisPt will enhance the treatment of PDAC. Time-staggered delivery of each nanocarrier can optimize the delivery of drugs to specific tumor compartments, thereby leading to effective stromal modulation, increased access of secondary Gem-cisPt-MSNs at the tumor site and improved therapeutic performance (**Figure 3.3**). To prove this hypothesis, we following aims are proposed:

a. Synthesis and characterization of CyP-MSNs.

b. *In vitro* evaluation of the synthesized CyP-MSNs for its cytotoxicity. Evaluation of combination effect of CyP-MSNs and Gem-cisPt-MSNs, which were

synthesized and completely investigated in the previous chapter.

c. *In vivo* investigation of safety, biodistribution, and therapeutic efficacy of sequential combination of CyP-MSNs plus Gem-cisPt-MSNs in HPAF II xenograft and transgenic PDA.MUC1 mice models.
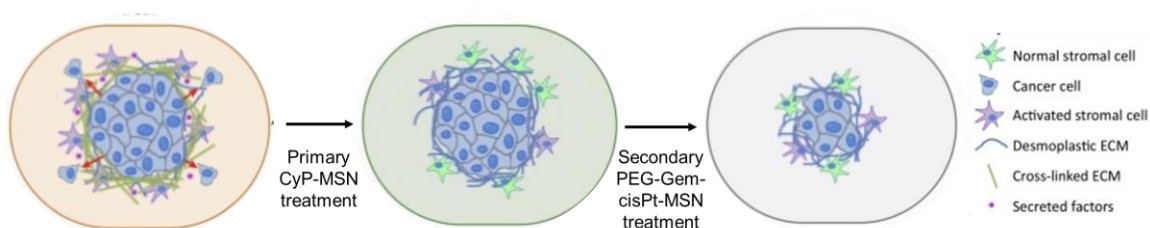
Figure 3.3. Schematic representation of the performance of proposed sequential time-staggered therapy. The primary treatment (CyP-MSNs) will decrease the stromal barrier by TME modulation. The secondary treatment (PEG-Gem-cisPt-MSNs) will efficiently kill the cancer cells.

3.2 Materials and methods.

3.2.1 Materials.

All materials are described in section 2.2.1.

3.2.2 Experimental methods.

3.2.2.1 Synthesis of PEG-Gem-cisPt-MSNs.

The synthesis of PEG-Gem-cisPt-MSNs is already described in the experimental sections 2.2.2 and 2.2.3.

3.2.2.2 Synthesis of PEG-CyP-MSNs.

3.2.2.2.1 Synthesis of MSNs.

MSNs were synthesized following our previous procedure with slight modifications (163, 164). Briefly, the surfactant CTAB (0.78 g, 2.14 mmol) was dissolved in a mixture of ethanol (3.32 mL) and nanopure water (21.6 mL), followed by the addition of DEA (41.4 µL, 0.428 mmol). This surfactant mixture was stirred for 30

minutes at 60 ºC. To this solution, TEOS was added dropwise over a period of 5 minutes. The resulting suspension was stirred for 18 h at 60 ºC. The nanoparticles were then collected via centrifugation at 13,000 rpm for 15 minutes, washed with ethanol three times and stored in ethanol.

The surfactant template was extracted by washing the MSNs in 1M HCl methanolic solution (10 mg of MSNs in 1 mL of the acid solution). The MSNs were dispersed in the acid solution and stirred for 10 h at 60 ºC. MSNs were then collected via centrifugation and washed with ethanol three times. A second acid wash was performed under the same conditions for 6 h. The surfactant-free MSNs were washed with ethanol three times and stored in ethanol.

3.2.2.2.2 Synthesis of Phos-MSNs

Post-synthetic grafting of MSNs using TPMP was carried out following previously reported procedure was slight modification (165). MSNs (200 mg) were dispersed in nanopure water (13 mL). An aqueous solution of TPMP (113.5 µL, 0.2 mmol in 13 mL water, pH adjusted to 6-7) was added to the MSN dispersion. The mixture was stirred for 3 h at 40 ºC. Finally, the nanoparticles were collected via centrifugation, washed thrice with ethanol to afford Phos-MSN.

3.2.2.2.3 Synthesis of PEI-coated MSNs.

MSNs were coated with PEI polymer using the procedure previously reported (132). Phos-MSNs (100 mg) were dispersed in ethanol (40 mL). PEI solution (1.8 KDa, 10 mL, 2.5 mg/mL in ethanol) was added to the MSN dispersion and stirred for 1 h at room temperature. The nanoparticles were collected via centrifugation and washed thrice with ethanol to afford PEI-MSNs. The successful coating of PEI on MSN surface was

determined using ninhydrin assay following the procedure described in section 2.2.3.4.

3.2.2.2.4 Synthesis of PEG-PEI-MSNs.

To synthesize PEG-PEI-MSNs, PEI-MSNs (30 mg) were dispersed in 15 mL of anhydrous acetonitrile. To this dispersion, MeO-PEG-SCM (15 mg) was added and stirred for 48 h at room temperature. Finally, the MSNs were collected via centrifugation, washed thrice with ethanol to afford PEG-PEI-MSN.

3.2.2.2.5 Synthesis of CyP-MSNs.

PEG-PEI-MSNs (40 mg) were dispersed in 40 mL of water. Cyclopamine (CyP, 20 mg) was dissolved in warm DMSO (5 mL) and was heated to maintain the solution at 60 ℃. The warm CyP solution was added slowly to the MSN dispersion under slow stirring. The mixture was stirred for 30 min at 40 ℃. The dispersion was then gradually allowed to cool down to room temperature. The mixture was allowed to stir for an additional 24 h at room temperature. Finally, CyP-MSNs were collected via centrifugation, washed twice with water and stored in water.

3.2.2.2.6 Quantification of CyP loaded in MSNs.

The amount of CyP complexed with PEG-PEI-MSNs was quantified using UHPLC (Thermo scientific UHPLC plus focused series LC/UV Vanquish diode array detector system) fitted with 1.9 μm particle size, 100 x 2.1 mm Hypersil Gold C18 column (Thermo Scientific, USA). Samples (10 μL) were injected with a flow rate of 250 μL/min in 10% Solvent B (Solvent A:acetonitrile; Solvent B: 99.9% water/ 0.1% Formic Acid (v/v)). Analytes were eluted from the column after 1 min holding at 10 % B with a linear gradient to 100% B using a flow of 9 μL/min. After 3 min holding at 100% B, the column was returned to 10% B in 4 min and re-equilibrated for 5 min before the next

injection. CyP standards in acetonitrile ranging from 100 to 800 ng/mL with a 10 μL injection volume. Diluted aliquots from the supernatants obtained after the synthesis of CyP-MSNs were used for this analysis.

3.2.2.3 In vitro studies.

3.2.2.3.1 Cell culture.

Capan-2 and MiaPaca-2 cells were maintained in DMEM media supplemented with FBS (10%), Penicillin-streptomycin antibiotics (1%), Glutamax (1%) and NEAA (1%). HPAF II cells were maintained in EMEM media supplemented with FBS (10%), Penicillin-streptomycin antibiotics (1%), Glutamax (1%), and NEAA (1%). HPAF +++ cells were sorted from HPAF II cells positive for CD24, CD133, and EPCAM markers. Sorted cells referred to as HPAF triple-positive cells (HPAF +++ cells) were maintained in DMEM:F12 media with low FBS (5%). All the cells were maintained at 37 ºC under a 5% CO_2 atmosphere. The cell culture and incubation conditions for all *in vitro* experiments are as indicated above unless otherwise mentioned. The media volume in 96-well plate is 100 μL.

3.2.2.3.2 In vitro cytotoxic effect of CyP-MSNs in PDAC cells.

Capan-2, HPAF II, and MiaPaca-2 cells were seeded in 96-well plate at a cell density of 1000 cells per well. The cells were incubated for 24 h and then inoculated with different MSN materials (PEI-MSNs and CyP-MSNs) at increasing concentration (1-100 μg/mL). The MSNs were prepared in complete cell culture media and treated for 72 h. The cells were then washed once with PBS, replaced with fresh media and incubated for another 24 h for recovery. Finally, the cells were washed once with PBS, and cell viability was evaluated using MTS assay. For MTS assay, 20 μL of the CellTiter 96®

solution was added to each well containing 100 μL media. The cells were incubated for 2.5-3.5 h depending on the cell type, and the absorbance was measured at 490 nm using a Multiskan FC plate reader.

3.2.2.3.3 Cytotoxic effect of the sequential combination: CyP-MSNs and Gem-cisPt-MSNs.

HPAF II or HPAF +++ cells were seeded in 96-well plate at a density of 2000 cells per well. The cells were incubated for 24 h, and then the cells were inoculated with CyP-MSNs (10 µg/mL, CyP 4.4 µg/mL). The cells were treated with CyP-MSNs for 24 h. The cells were then washed with PBS and inoculated with increasing concentrations of Gem-cisPt-MSNs (1-50 µg/mL). The cells were treated with Gem-cisPt-MSNs for 48 h. Post-treatment, the cells were washed once with PBS, replaced with fresh media and incubated for another 24 h for recovery. Finally, the cells were washed once with PBS, and cell viability was evaluated using MTS assay, as described in the previous section. As control group, no CyP-MSNs treatment and only Gem-cisPt-MSN treatment was used.

3.2.2.4. In vivo therapeutic efficacy of CyP-MSN plus PEG-Gem-cisPt-MSN in HPAF II xenograft mice model.

All animal experiments were reviewed and approved by the Institutional Animal Care and Use Committee under the protocol 17-015. Female NOD SCID Gamma (NSG) mice were purchased from Jackson Laboratory.

3.2.2.4.1 Establishment of HPAF II xenograft mice model.

To establish the HPAF II tumors, mice were implanted subcutaneously (s.c, right flank) with HPAF II cells (1×10^6) using Matrigel (1:1 dilution in PBS). Tumor growth

was monitored by caliper measurements every alternate day, and the tumor volume was

calculated using the formula:

$$\text{Tumor volume} = (L*(W)^2)/2 \qquad\qquad \text{Equation (2)}$$

where L is the length and W is the width of the tumor (169).

In vivo targeting and therapeutic efficacy studies were initiated 11 days post HPAF II cell

implantation with tumor volumes reaching approximately 100 mm^3.

3.2.2.4.2 Sequential therapy studies in HPAF II tumor-bearing xenograft mice.

Mice bearing HPAF II tumors were randomly divided into 4 treatment groups

(n=3); PBS, CyP-MSNs plus free drugs, PEG-Gem-cisPt-MSNs, and CyP-MSNs plus

PEG-Gem-cisPt-MSNs. The treatment regimen is depicted in **Figure 3.7a**. Tumor growth

was monitored by measuring the tumors every alternate day. The primary treatment

(CyP-MSNs, 5 mg/Kg in PBS) were injected intratumorally (*i.t*); followed the secondary

treatment of PEG-Gem-cisPt-MSNs (40 mg/Kg in 100 µL of water) or Free Gem/cisPt

(9.52/2.05 mg/Kg), which was injected intravenously (*i.v*) 48 h post CyP-MSNs. Primary

CyP-MSNs plus secondary PEG-Gem-cisPt-MSNs was referred to as the therapy cycle.

"Plus" in the therapeutic studies is used to determine the sequential combination of CyP-

MSNs followed by PEG-GEM-cisPt-MSNs for simplicity. The treatment consisted of a

total of 5 therapy cycles with an additional 48 h-interval between each cycle. Tumor

growth was monitored every other day using calipers. On day 30 post cell implantation,

mice were euthanized, and the major organs were collected including liver, lungs,

kidneys, spleen, heart, and tumor. The fluorescence associated with each organ was

evaluated using the IVIS imaging system. Portions of the organs and tumors were fixed

in formalin for histological analysis. Portions of the tissue samples were frozen and used

later to determine the Si and Pt content.

3.2.2.4.3 Ex vivo fluorescence imaging and analysis.

The harvested organs were placed in Petri dishes and imaged using the IVIS® Spectrum imaging system. The fluorescence images were analyzed, and fluorescent intensity was quantified using the ROI tool of the Living Image® software. The data is presented as the average radiant efficiency associated with each organ. The results are reported as the mean ± SD (n=3 mice per treatment group).

3.2.2.4.4 Analysis of organ Si and Pt content.

Samples from different organs, including the liver, lungs, heart, spleen, kidneys, and tumor, were weighed and thoroughly dried in an oven at 60 ℃ for 3 days. The dried organs were weighed again and digested using a mixture of HNO_3:HCl:HF (10:2:1). The samples were placed in the digestion vessels with the acid mixture for a 20 min pre-digestion at room temperature. The samples were then further digested in a CEM Mars microwave system under the following conditions: ramp to 200 ℃ for 20 minutes, hold at 200 ℃ for 20 minutes and cool down to room temperature. The digested samples were then diluted to 50 mL using DI water.

The Si content was analyzed using an ICP-OES (PerkinElmer 8300 DV). Calibration standards were prepared by diluting the Si element PlasmaCAL (SCP Science) standard in 0.1 M HNO_3. The wavelength of 251.66 nm was selected for Si analysis and the concentration was determined using Syngistix software. The data are represented as the mg of Si per g of tissue. For each organ tested, the results are reported as the average ± SD (n=3 mice per group).

The Pt content was analyzed using an ICP-MS (Thermo Electron X series). The Pt analysis was performed by monitoring the signal of the ^{195}Pt isotope. Calibration standards were prepared by diluting Pt standard in 5% HCl matrix. The data are represented as the µg of Pt per g of tissue. For each organ tested, the results are reported as the average ± SD (n=3 mice per group).

3.2.2.4.5 Histology and Immunohistochemistry.

a. <u>Hematoxylin and eosin (H&E) staining</u>. Major organs such as liver, lungs, spleen, kidneys, heart, and tumors were collected after *in vivo* experiments. For each tissue, a small portion was fixed in a 10% buffered formalin for 24 h at 4 ºC. The fixed tissues were stored in transferred and stored 70 % ethanol. The organs were paraffin-embedded, sectioned (4 µm thick), and stained with Hematoxylin and Eosin (H&E). The H&E stained tissue sections were imaged using a fluorescent microscope (IX71, Olympus) at 10x magnification. Histological signs of toxicity i.e., changes in normal tissue structures were investigated.

b. <u>Picrosirius red staining in tumor tissue</u>. Tumor sections (4 µm) were used to determine collagen deposition using picrosirius red staining. The tissue sections were de-waxed by placing the slides in an oven overnight at 60 ºC. The tissues samples were immediately placed in xylene solution (2 washings) and rehydrated in 100% ethanol (3 washings) and finally placed in water. The hydrated tissues slides were stained in picrosirius red for 1 h in a humidified chamber. The slides were washed twice with acidified water, changing the acidified water in between each wash. The tissue slides are dehydrated (three changes of 100% ethanol), followed by clearing in xylene. The slides were then mounted in a resinous medium. The stained tissues were

imaged using a fluorescent microscope at 4x magnification (IX71, Olympus).

3.2.2.5 Therapeutic efficacy of CyP-MSN and PEG-Gem-cisPt-MSNs in PDA-MUC1 mice model.

The establishment of PDA.MUC1 mice is described in the section 2.2.8. The PDA.MUC1 mice after 43 weeks of tamoxifen injection, were used for the *in vivo* study. One mouse in the control group and 2 mice in the treatment group. The primary treatment (CyP-MSNs, 5 mg/Kg in PBS) were injected intravenously; followed by 5 days interval, the secondary treatment (PEG-Gem-cisPt-MSNs, 40 mg/Kg). Primary CyP-MSNs plus secondary PEG-Gem-cisPt-MSNs was referred to as one therapy cycle. A total of 3 cycles of primary-secondary treatment were followed with 10 days interval between each cycle. After the final cycle, the major organs like the liver, lungs, kidneys, spleen, heart, and pancreas were collected, fixed and stained for imaging. The pancreas was weighed and fixed in formalin. The pancreas was sectioned at 4 um thickness at various depths. A total of 4 sections were stained with H&E and imaged to determine the PanIN lesion and PDA stage.

3.2.3. Statistical analysis.

All the data in this chapter is represented as mean ± SD unless mentioned otherwise. The hydrodynamic size and ζ-potential analysis using DLS were performed in triplicates. The amount of cyclopamine complexed to the MSNs is reported as average of 3 independent batches (n=3). For the cell viability studies, the GraphPad prism was used to calculate the IC_{50} values (n=6). The *in vivo* therapeutic experiments were evaluated using n=3 mice per group. The tumor volumes were reported as mean ± SEM, and two-way ANOVA with Tukey's multiple comparison test was used for statistical analysis. For

tumor weights, unpaired t-test was performed to analyze the statistical difference of each group. The NIR fluorescence, Si and Pt content in organs were evaluated using n=3 mice per group. All the statistical analysis were performed using GraphPad Prism (v8.2.0 for Windows, La Jolla California, CA, USA) with α=0.05 and reported as stars assigned to the p values; ****p≤0.0001, ***p≤0.001, ** p≤0.01, * p≤0.05 and ns p>0.05.

3.3 Results and Discussions.

3.3.1 Synthesis and characterization of PEG-Gem-cisPt-MSNs.

The detailed synthesis and characterization of the PEG-Gem-cisPt-MSNs are described in sections 2.3.2 and 2.3.3.

3.3.2 Synthesis and characterization of CyP-MSNs.

The CyP-MSNs were synthesized following the scheme depicted in **Figure 3.4a**. To synthesize CyP-MSNs, the as-synthesized MSNs were firstly grafted with phosphonate groups to afford Phos-MSNs with a negative surface charge. The Phos-MSNs were coated with PEI via electrostatic interaction between PEI and the phosphonate groups on MSNs to afford PEI-MSNs. PEI-MSNs were conjugated with MeO-PEG-NHS via coupling chemistry between the NHS group and the amines on the PEI-MSNs. CyP molecule was complexed to PEG-PEI-MSNs through hydrogen bonding, due to the presence of a large number of hydrogens on PEI. This approach was successfully used to carry and deliver LY364947, a TGF-β inhibitor (132).

The D_h and surface charge of CyP-MSNs were characterized using DLS. CyP-MSNs exhibited D_h of 252 ± 40 nm (PdI = 0.3) in PBS. The surface charge of the CyP-MSNs was almost neutral with a zeta potential of 7.9 ± 0.7 mV. While the PEG-PEI-MSNs showed a zeta potential of 28 ± 1 mV in PBS, the CyP bonding decreased this to +

7.9 ± 0.7 mV. Further, the amount of CyP loaded onto the MSNs was evaluated using HPLC by determining the CyP in the supernatants and washings after the loading process. Based on the HPLC analysis, 447.5 μg CyP was complexed per mg of PEG-PEI-MSN which results for 44.7 wt% loading.
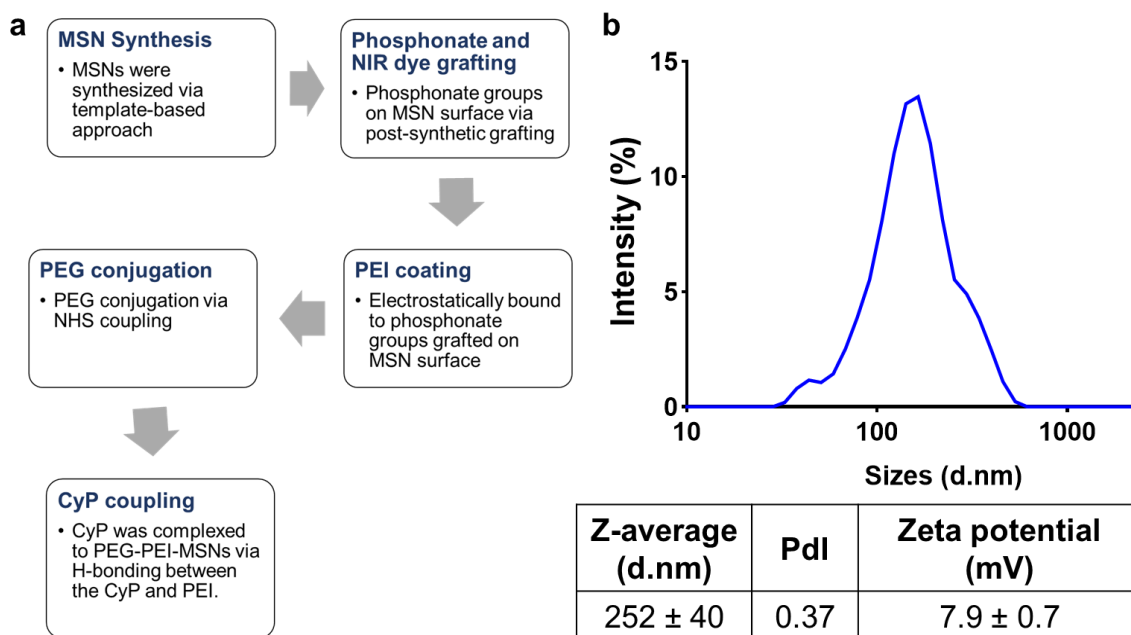
Figure 3.4. Synthesis and characterization of CyP-MSNs. **(a)** Graphical representation of the scheme followed for the synthesis of CyP-MSNs. **(b)** The particle size distribution (PSD) plot of CyP-MSNs in PBS. Hydrodynamic size and zeta potential of CyP-MSNs obtained using DLS (n=3).

3.3.3 *In vitro* cytotoxicity of CyP-MSNs.

The cytotoxic effect of CyP-MSNs was investigated in Capan-2, Miapaca-2, and HPAF II cells. The cells were treated with CyP-MSNs for 72 h, and cell viability was determined using MTS assay and control group involved PEI-MSNs. As depicted in **Figure 3.5**, CyP-MSNs exhibited cytotoxicity in the PDAC cells at concentrations higher than 60 μg/mL. As mentioned previously, SHh activation in the PDAC cells increases cell proliferation, invasion, and metastasis. Nevertheless, the pathway inhibition may not always contribute to the cytotoxicity ability of the SHh inhibitors as cancer cells may not

completely depend on the SHh for growth and proliferation. Hence, the CyP concentrations required to observe cytotoxic effects are high (218).
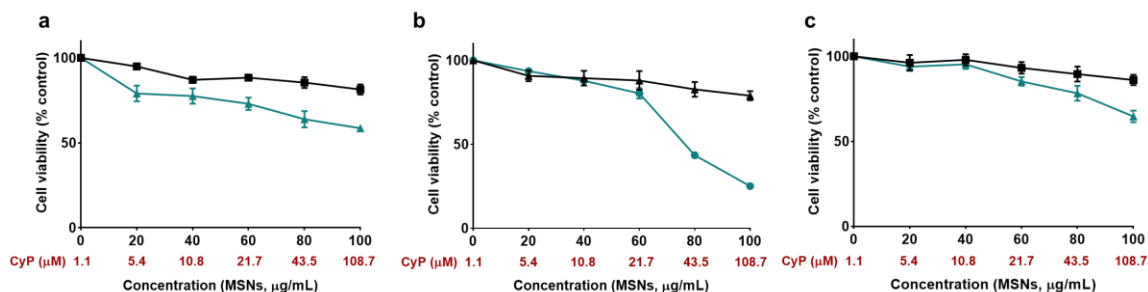
Figure 3.5. Cytotoxicity of CyP-MSNs in a panel of PDAC cells. PDAC cells MiaPaca-2 **(a)**, Capan-2 **(b)**, and HPAF II **(c)** cells were treated with PEI-MSNs (black) and CyP-MSNs (green), for 72 h and cell viability was analyzed using MTS assay.

In addition, PDAC cells are heterogenous, and it has been well documented that variability exists between PDAC cells in terms of SHh receptor expression, the sensitivity of SHh inhibitors and non-canonical SHh activation, where the cancer cells activate SHh downstream of SMO or PTCH receptors and hence do not respond to the SMO antagonists (219). Based on previous reports, it is shown that PDAC cells like MiaPaca-2 and Capan-2 show increased SHh receptor expression and also showed increased sensitivity towards SHh inhibitors like CyP and vismodegib (217). Whereas cells like BxPC3 and Panc-1 do not express the SHh receptors and show resistance to SHh inhibition (217, 220). We are further exploring the effect of CyP-MSNs treatment on the expression of SHh pathway markers including SHh ligand, PTCH receptor and the downstream Gli-1 transcription factor to confirm the SHh inhibition ability of CyP-MSNs.

3.3.4 *In vitro* cytotoxicity of CyP-MSNs plus Gem-cisPt-MSNs.

Next, we investigated the sequential treatment of CyP-MSNs and Gem-cisPt-MSNs in HPAF II cells. The cells were firstly treated with CyP-MSNs (10 μg/mL, 4.4

µg/mL) for 24 h, which served as the primary treatment. The cells were then inoculated with increasing concentrations of Gem-cisPt-MSNs, which represented the secondary treatment. Cell viability analysis after treatment was assessed, which indicate the cytotoxicity of HPAF II cells was not significantly different with or without the CyP-MSN primary treatment (**Figure 3.6a**). The pre-treatment of CyP-MSNs did not enahnce the cytotoxicity of Gem-cisPt-MSN in HPAF II cells as we used very low concentration of CyP-MSNs which was chosen to inhibit SHh pathway and not necessarily cause cytotoxic benefit. The use of low concentration CyP to selectively cause inhibitory effect on SHh pathway has been previously explored as an approach for controlled stroma modulation while preventing stroma depletion in the PDAC tumors (218).
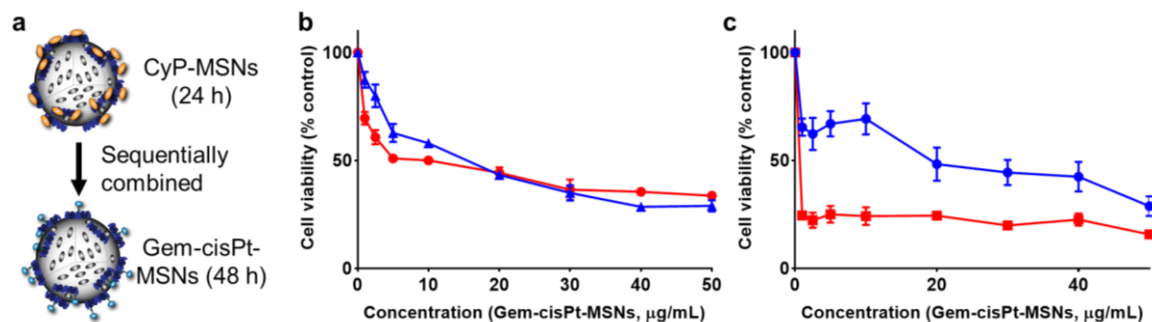
Figure 3.6. *In vitro* cytotoxicity evaluation of CyP-MSNs plus Gem-cisPt-MSNs in PDAC cells. **(a)** Graphical representation of sequential treatment of CyP-MSNs plus Gem-cisPt-MSNs. Cell viability data after sequential treatment of CyP-MSNs plus Gem-cisPt-MSNs (red) and Gem-cisPt-MSNs only (blue) in HPAF II **(b)** and HPAF +++ cells **(c)**.

In addition to HPAF II cells, the sequential treatment was investigated in HPAF triple-positive cells (HPAF +++ cells). The HPAF +++ cells are positive for CD24, CD44 and EPCAM which is a characteristic of cancer stem-like cells. The CyP-MSNs pre-treatment drastically increased the cytotoxic effect of Gem-cisPt-MSNs (**Figure 3.6b**). The increased cell cytotoxicity observed in the sequential combination of CyP-MSN plus Gem-cisPt-MSNs in HPAF +++ cells could be explained by the fact that cancer stem-like

cells overexpress embryonic pathways like SHh, Notch and Wnt. The cancer stem-like cells depend on these pathways for growth and stemness which increases their sensitivity towards the mentioned pathway inhibitors (221). Besides, the treatment of sequential therapy on HPAF +++ cells showed that chemotherapy alone is not effective against cancer stem-like cells. These cells are known to escape chemotherapy or radiotherapy and result in relapse/recurrence. The effective treatment of CyP-MSNs plus Gem-cisPt-MSNs could be a potential treatment to target the cancer stem cell population (222).

3.3.5 Therapeutic efficacy of the sequential treatment using CyP-MSNs and PEG-Gem-cisPt-MSNs in HPAF II xenograft mice model.

Human PDAC cells HPAF II were used to develop xenograft mice model for this study. Previous reports showed that tumors derived from HPAF II developed abundant fibrous stroma (223). The treatment regimen was followed according to the scheme depicted in **Figure 3.7a,** and four treatment groups were tested; PBS, CyP-MSNs plus free drugs, PEG-Gem-cisPt-MSNs, and CyP-MSNs plus PEG- Gem-cisPt-MSNs. Mice bearing ~100 mm^3 HPAF II tumors were intratumorally injected with CyP-MSNs (5 mg/kg) followed by intravenous injection of PEG-Gem-cisPt-MSNs (40 mg/kg) and a total of 5 treatment cycles were followed (**Figure 3.7a**). The CyP-MSNs were not injected in the first cycle to avoid the risk of stroma ablation (214).

The tumor volumes were measured over the course of treatment. Based on the tumor volume measurements, the CyP-MSNs plus PEG-Gem-cisPt-MSNs group showed greater tumor growth inhibition (71.3%) compared to the PBS group. Whereas, PEG-Gem-cisPt-MSNs and the CyP-MSNs plus free Gem/cisPt exhibited 47.6% and 15.2% inhibition, respectively (**Figure 3.7b**). At the endpoint, the tumors were harvested and

weighed to determine the therapeutic efficacy of sequential therapy. As observed in **Figure 3.7c**, the tumors in the sequential therapy group weighed significantly lower compared to the treatment with PEG-Gem-cisPt-MSNs only, CyP-MSNs plus free Gem/cisPt and PBS groups ($p < 0.05$, $p < 0.01$ and $p < 0.01$, respectively). Though the PEG-Gem-cisPt-MSNs performed much better than the free drugs group and PBS ($p < 0.05$), the pretreatment with CyP-MSNs significantly increased the therapeutic benefit of PEG-Gem-cisPt-MSNs (**Figure 3.7c**).
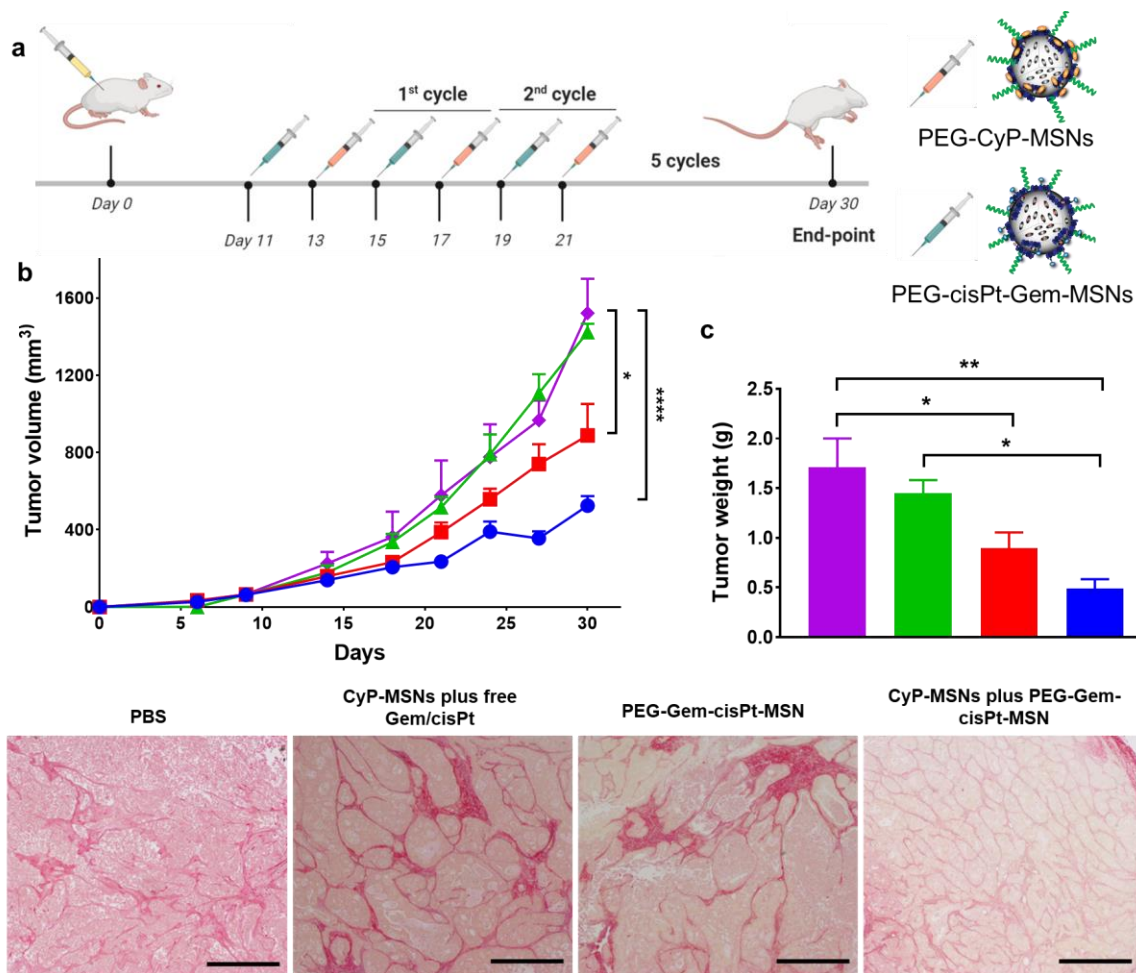
Figure 3.7. Therapeutic study of CyP-MSNs plus PEG-Gem-cisPt-MSNs in the HPAF II bearing xenograft mice. **(a)** Schematic representation of the treatment regimen; HPAF II cells were subcutaneously implanted in NSG mice (yellow arrow). **(b)** Tumor volume measurement of mice in different treatment groups: PBS (purple downward triangles), CyP-MSNs plus free drugs (green upward triangles), PEG-Gem-cisPt-MSNs (red squares), and CyP-MSNs plus PEG-Gem-cisPt-MSNs (blue circles) (n=3 mice per group). Two-way ANOVA was performed between

different groups and time points to determine the statistical difference. **(c)** Tumor weights measured at the endpoint of the therapeutic efficacy studies after 5 cycles: PBS (purple), CyP-MSNs plus free drugs (green), PEG-Gem-cisPt-MSNs (red), and CyP-MSNs plus PEG- Gem-cisPt-MSNs (blue) (n=3 mice per group). t-test was performed between different groups to determine the statistical difference. **(d)** *Ex vivo* analysis of tumor sections stained with picrosirius red for collagen content analysis after treatment (scale bar = 1 mm). Statistics: ****p≤0.0001, ***p≤0.001, ** p≤0.01, * p≤0.05 and ns p>0.05.

We tested the effect of sequential treatment on the tumor stroma changes. One of the primary and simple markers used for the stroma changes is the extracellular matrix deposition. Collagen deposition in the tumors can be easily accessed using picrosirius red stain assay. Hence, tumor sections were stained with picrosirius red. Based on the stained tissue images, there was a significant different in the collagen deposition in the tumors when treated with sequential combination of CyP-MSNs plus Gem-cisPt-MSNs. The collagen content was decreased as well as the spatial distribution of the collagen was altered (**Figure 3.7d**). In the PBS group, where huge areas showed intense collagen as a characteristic of the strong stroma in PDAC tumors. Whereas the tumors treated with the combination of CyP-MSNs plus Gem-cisPt-MSNs showed decreased collagen content spread evenly throughout the tumor.

3.3.6 *In vivo* biodistribution and safety of sequential therapy.

The safety of the sequential treatment was evaluated based on the mice body weights and histopathological analysis of major organs. Firstly, based on the NIR fluorescence signaling associated to the major organs acter treatment was evaluated. The MSNs were predominantly localized in spleen and liver, (**Figures 3.8a and 3.8b**). This is similar to our observation in the previous study (see section 2.3.9) and is associated to the slow clearance from the hepatobiliary system.
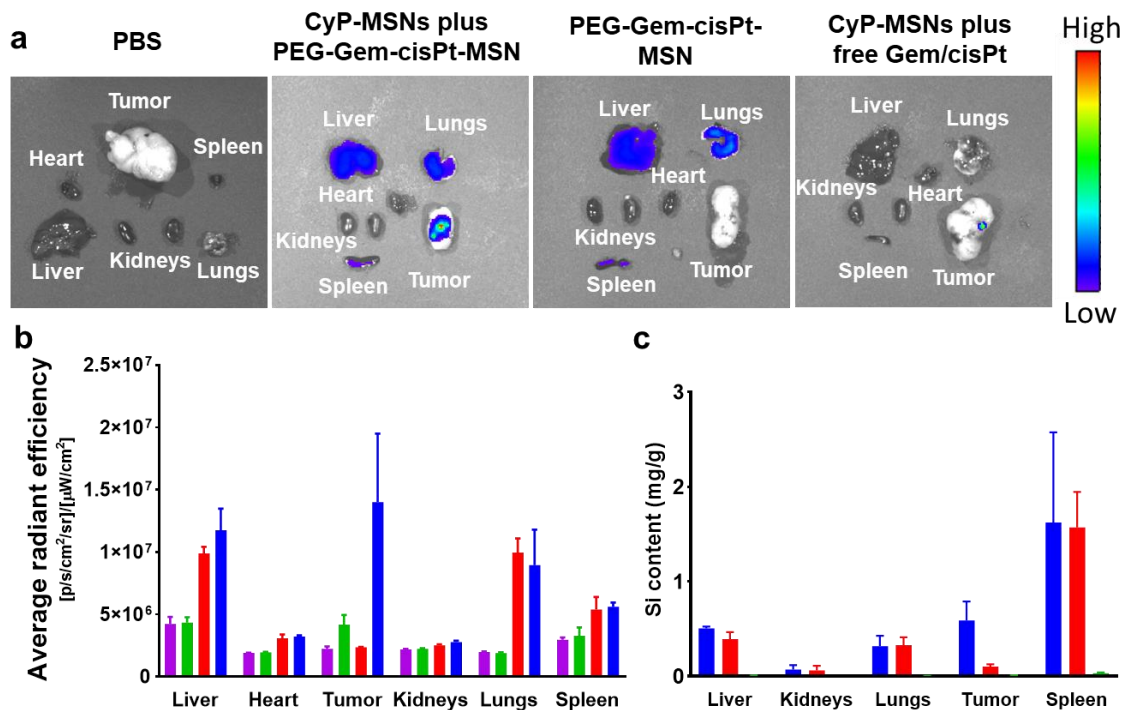
Figure 3.8. End-point tissue analysis after the sequential treatment of CyP-MSNs plus PEG-Gem-cisPt-MSNs. **(a)** Fluorescent signals captured by the IVIS Imaging system from different organs harvested from mice injected with PBS, CyP-MSNs plus PEG-Gem-cisPt-MSNs, PEG-Gem-cisPt-MSNs and CyP-MSNs plus free Gem/cisPt. **(b)** Quantification of the NIR fluorescence signals from organs after various treatments PBS (purple), CyP-MSNs plus PEG-Gem-cisPt-MSNs (blue), PEG-Gem-cisPt-MSNs (red) and CyP-MSNs plus free Gem/cisPt (green) as analyzed using Living Image® 4.5.5.

The biosafety of sequential treatment was evaluated by monitoring the mice body weights during the treatment process and histopathological investigation of the organs post treatment. The mice's behavior and body weights were monitored throughout the treatment which was used as a primary parameter to determine if the material shows any adverse effects. No significant changes in body weights were observed in any treatment groups (**Figure 3.9a**). Moreover, there was no behavioral changed noted during the treatment. Also, the histopathological evaluation of major organs like liver, lungs, kidneys, and heart showed no significant signs of toxicity, as no cellular changes in the tissue, which can be used as key signs of toxicity were observed in CyP-MSNs plus PEG-

Gem-cisPt-MSNs and PEG-Gem-cisPt-MSNs groups compared to the PBS group (**Figure 3.9b**). These results confirmed that the MSNs are biocompatible when used as a sequential therapy, as reported in previous chapter and other studies (187, 188).
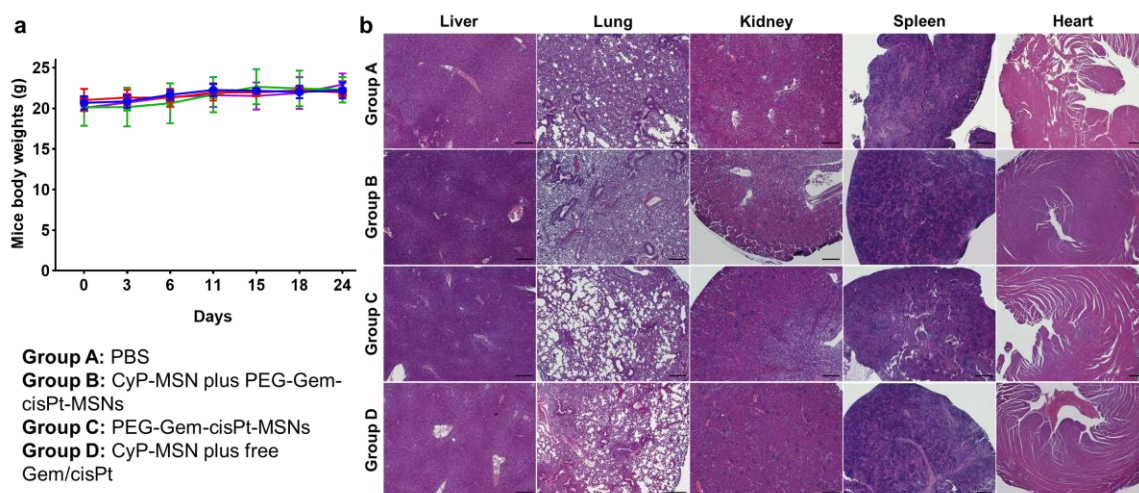
Figure 3.9. Biosafety of the sequential treatment. **(a)** Body weights of mice monitored throughout the treatment under different groups; Group A PBS (purple downward triangle), group B CyP-MSNs plus free Gem/cisPt (green upward triangle), group C PEG-Gem-cisPt-MSNs (red squares), and group D CyP-MSNs plus PEG-Gem-cisPt-MSNs (blue circle) (n=3). **(b)** H&E stained slides of liver, lungs, kidneys, spleen, and heart harvested from the mice after the therapeutic efficacy studies (Scale bars = 500 μm).

Nevertheless, morphological changes were observed in the kidney tissue from mice injected with CyP-MSNs plus free drugs (**Figure 3.10a**). The enhanced toxicity associated with free drugs could be due to the high drug (Pt) content in the kidney tissue (**Figure 3.10b**). The increased off-target toxicity of Gem and cisPt in liver and kidney is well-documented and is one of the major side effects of chemotherapy. Further, blood serum analysis needs to be performed to understand the toxicity with free Gem/cisPt.
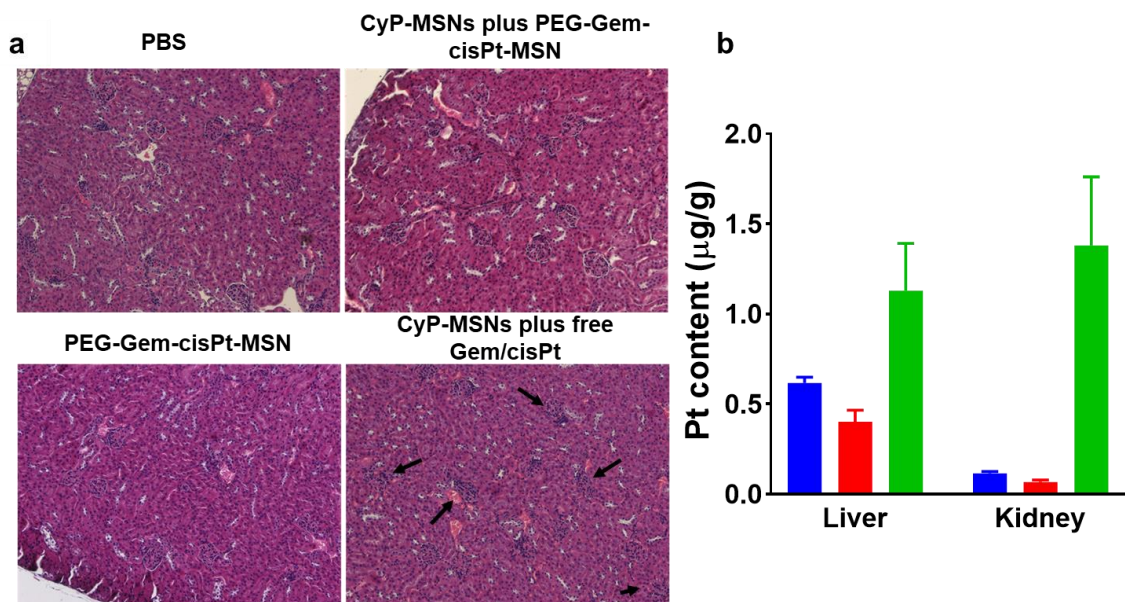
Figure 3.10. Organ histology for the assessment of toxicity. **(a)** Histological analysis of kidney tissue sections showing the toxicity in different treatment groups. The bowman's capsule and edema are shown in the zoomed inset images. **(b)** Pt content analysis in various organs after treatment groups. Treatment groups CyP-MSNs plus PEG-Gem-cisPt-MSNs (blue), PEG-Gem-cisPt-MSNs (red) and CyP-MSNs plus free Gem/cisPt (green) (n=3).

Based on the results obtained from the therapeutic efficacy in HPAF II xenograft mice, we propose that the CyP-MSNs pre-treatment inhibit the stroma-cancer cell interaction via SHh inhibition. This leads to stromal modulation, better penetration of the secondary nanoparticles into the tumor and delivery of chemotherapy agents Gem/cisPt. Though increased fluorescence was associated with the tumors injected with primary CyP-MSN and Gem-cisPt-MSNs **(Figure 3.8)**. As MSNs were used as a carrier for primary and secondary treatment, the fluorescence or Si analysis cannot be used to deduce that the stroma modulation effect of the primary CyP-MSN treatment, increased the tumor accumulation/penetration of secondary PEG-Gem-cisPt-MSNs.

The collagen deposition study showed that the sequential treatment caused changes in the ECM of the tumors. Evident decrease in the collagen content and spatial distribution was observed which support the idea that CyP-MSNs' treatment caused

tumor stroma modulation while retaining the restrictive properties of ECM, not leading to stromal depletion. Detailed tumor stroma modulation is being investigated by analyzing the stromal fibroblast marker alpha-SMA, ECM deposition by analysis of collagen, and changes in the tumor microvessels by CD31 analysis (218). Overall, by time-staggered controlled delivery of CyP and Gem/cisPt using MSNs, we were able to effectively break the tumor cell-stromal communication.

SHh pathway is also important for the cancer stem cell maintenance in the tumors. As demonstrated in **Figure 3.6**, the CyP-MSNs effectively eliminated the HPAF +++ cells. The cancer stem cells are responsible for the chemotherapy resistance, heterogeneity in tumors, and relapse [ref]. Hence, the effect of sequential treatment of CyP-MSNs plus PEG-Gem-cisPt-MSNs on the cancer stem cell population in tumors needs to be investigated to understand the multi-component effect of CyP-MSNs.

3.3.7 *In vivo* **sequential therapy of CyP-MSNs plus PEG-Gem-cisPt-MSNs in PDA.MUC1 mice.**

We further evaluated the therapeutic ability of the sequential therapy of CyP-MSNs plus PEG-Gem-cisPt-MSNs in spontaneous PDA.MUC1 mice. PDA.MUC1 mice develop evident micro/macro-metastasis after 35 weeks of tamoxifen injection. Hence, the primary treatment was injected intravenously, followed by PEG-Gem-cisPt-MSNs after 5 days of primary CyP-MSNs administration. This cycle was repeated 3 times. After 3 cycles, the control mouse and one treatment mouse were euthanized. Major organs were collected. At the end-point, mice were euthanized, and major organs like pancreas, liver, kidney, heart, spleen were collected, fixed, and stained for H&E. The pancreas from each mouse was weighed, and the whole pancreas was fixed and sectioned to

evaluate the grade of PanINs and the progression of PDA (**Figure 3.11**). The control mice showed large tumor regions in the pancreas (yellow arrows, **Figure 3.11**) and high-grade PaINs with extensive stroma (red arrows). The weight of the pancreas from the control mice was 188.2 mg. The pancreas weight from the treatment group was measured to be 188 and 143.7 mg. the histological analysis of these pancreas showed significantly less PDAC regions compared to the control. Further stroma modulation needs to be evaluated in the pancreas of PDA.MUC1 mice as well as the effect of our treatment on the metastasis with increased number of mice in the treatment groups.
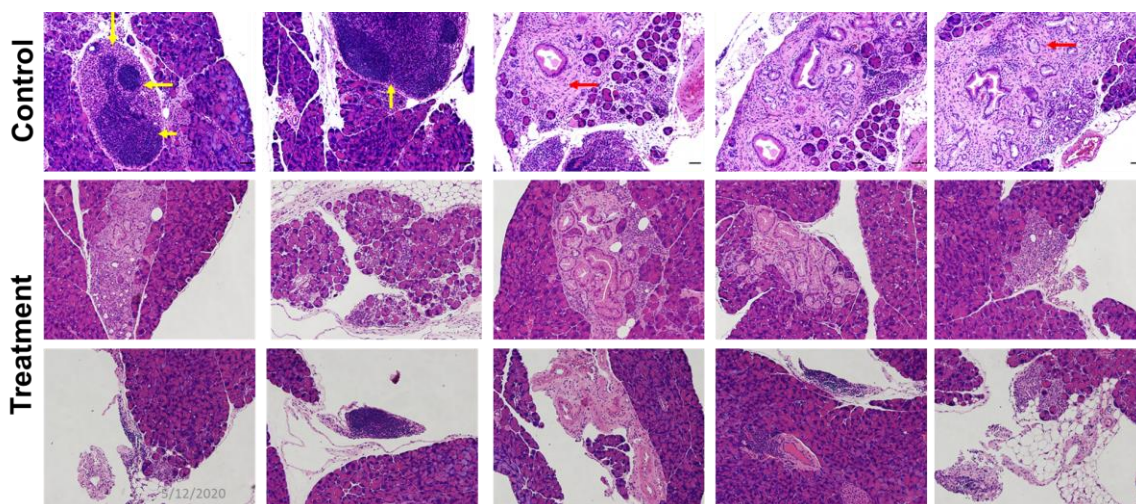
Figure 3.11. Pancreas H&E images of pancreas tissue after the therapeutic study, showing the sections PanIN lesions and invasive PDA.

3.4 Conclusions.

One of the major hallmarks of PDAC is the desmoplastic stroma where the intricate and dynamic crosstalk between cancer cells and stromal cells is dynamic and contributes to tumor progression and metastasis. Stroma causes elevated interstitial pressure, reduced blood flow, hypovascularity and acts as the physical barrier to drug delivery while it also contributes to increased resistance due to off-target toxicity of stromal cells. One of the most studied mediators of cancer cell-stroma crosstalk is the

aberrant activation of sonic hedgehog pathway leading to the intense desmoplasia observed in PDAC tumors. Inspired by recent studies and current clinical investigation of SHh inhibitors, we designed an MSN-based sequential therapy for stroma modulation (CyP-MSNs) and delivery of Gem/cisPt (PEG-Gem-cisPt-MSNs). Sequential delivery of CyP and Gem/cisPt using separate nanocarriers can control the time-dependent and spatial access of drug which have different targets in the tumors.

We successfully synthesized and characterized CyP-MSNs which indicated high CyP loading. The cytotoxicity of CyP-MSNs in PDAC cells, exhibited that low cytotoxicity from CyP-MSNs. In order to test the combination of CyP-MSN with Gem-cisPt-MSNs, low concentration of the CyP-MSNs was chosen. The intent is to block the crosstalk between PDAC cells and stromal cell, not necessarily lead to the death of either types of cells. and tested in PDAC cells. As intended, the combination therapy of CyP-MSNs plus Gem-cisPt-MSNs showed no effect on the HPAF II cells. In addition, upon testing this combination on the HPAF +++ cells, cancer stem-like cells, we observed dramatic benefit in cytotoxicity compared to the Gem-cisPt-MSNs alone. These results indicate the potential of using our combination to deplete the PDAC tumors of cancer stem-like cells which are responsible for resistance and recurrence which needs to be explored in detail in the future.

Fine tuning of CyP and Gem/cisPt delivery is another parameter which we controlled through the time-staggered sequential delivery of these drugs. The sequential combination of CyP-MSNs plus PEG-Gem-cisPt-MSNs therapy in an aggressive HPAF II tumor bearing mice showed increased tumor inhibition. In addition, tumor analysis indicated changes in the collagen deposition in the tumors which is a primary stromal

ECM component. We are currently studying the tumor stromal changes in detail with cancer-associated fibroblast markers and alterations in the blood vessels in the tumor.

Taken together, the nanoparticle-based sequential combination can lead to enhanced therapeutic efficacy in PDAC. Future studies involving orthotopic mice models which can mimic the aggressive desmoplastic reaction of the PDAC tumors, needs to be evaluated.

CHAPTER 4: TAB004-MSNs as a nanoprobe for bioimaging and early diagnosis of PDAC.

4.1 Introduction

4.1.1 Need for non-invasive early diagnostic imaging tools for PDAC.

The dismal outcome of PDAC is partially attributed to the inability to detect PDAC at the early stages. Due to the late presentation of the disease, less than 20% of patients are eligible candidates for surgical resection of pancreatic tumors. This emphasizes the urgent need to increase the percentage of patients diagnosed at early stages (30). Besides, the 5-year survival rate for patients diagnosed with stage I disease is 19 times higher than those diagnosed with stage IV. Hence, significant improvements in survival may be seen if we focus on shifting our efforts to the diagnosis of PDAC at early stages (224). PDAC arises from pancreatic ductal cells and progresses through a series of precursor lesions, with pancreatic intraepithelial neoplasia (PanINs) being the most common and well-studied precursor lesions. PanINs are morphologically classified into four grades, PanIN 1A, PanIN 1B, PanIN 2, and PanIN 3, where PanIN 3 is referred to as carcinoma *in-situ* and is characterized as stage 0 before they give rise to invasive adenocarcinoma (**Figure 4.1**) (27, 139). Diagnosis at the early stages including at the precursor lesions stage can significantly improve the therapeutic outcome of PDAC.

Extensive research in the tumorigenesis and computational insights in the genetic evolution of PDAC has proven that PanIN progression from the initiating mutation to the invasive carcinoma takes at least a decade. An additional 5 to 6 years are required for the cells to acquire metastatic ability (225). These results suggest that we should have a golden opportunity of 2 or 3 years to diagnose PDAC at early stages (PanIN and stage 0).
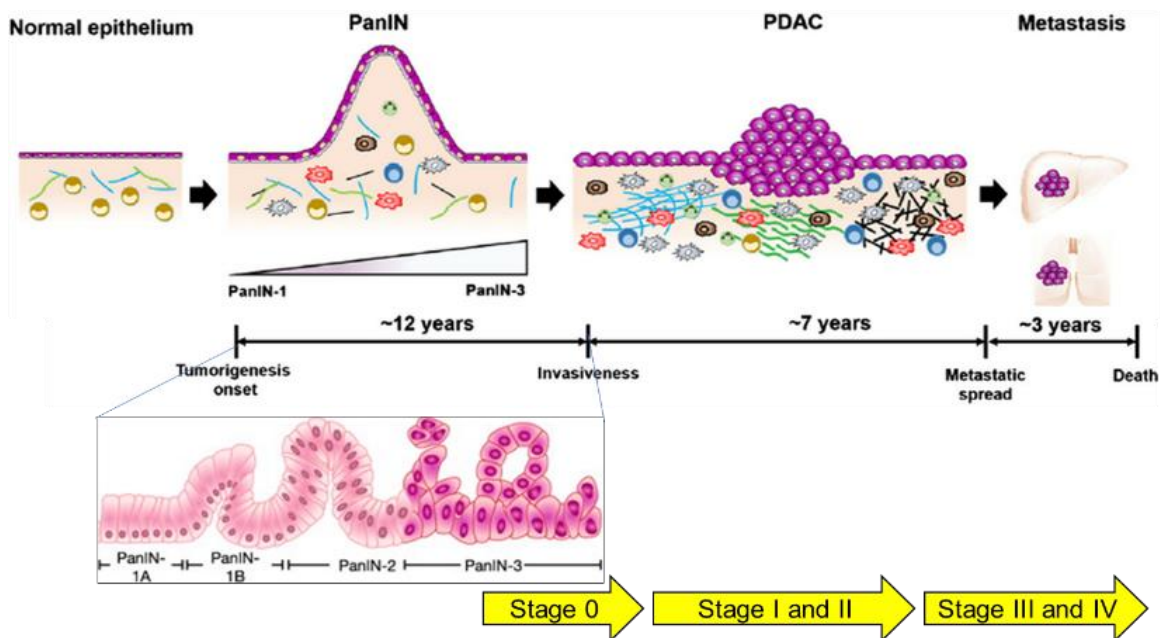
Figure 4.1. Molecular pathology of PDAC. Estimated time required for the progression of PDAC from PanIN precursor stage to invasive carcinoma and finally reaching the metastatic stage (27).

Despite this opportunity, the absence of symptoms in the initial stages, anatomical location of the pancreas, and lack of reliable biomarkers makes the early diagnosis and predictive imaging very difficult. In addition, more factors are being considered for determining high-risk individuals (HRI), for example recent onset of diabetes mellitus. Currently available imaging methods include magnetic resonance imaging (MRI), magnetic resonance cholangiopancreatography (MRCP), and endoscopic ultrasound (EUS). Abdominal ultrasonography is often the first procedure performed on patients. Most of these diagnostic imaging techniques have limitations in detection of small pancreatic tumors (136). With more factors being considered for HRI, potential diagnostic window, and limitations in current diagnosis, it is critical to develop reliable non-invasive, diagnostic tools for the early detection of PDAC at a curable stage (136, 226).

4.1.2 tMUC1 is a potential biomarker for early stage detection of PDAC.

The lack of reliable biomarkers is another limitation to detect PDAC at the early stages. Currently, some serum markers such as CA19-9, carcinoembryonic antigen (CEA), and DUPAN-2 are used for the diagnosis of PDAC. However, they are not reliable for early detection (136). In humans, tMUC1 glycoprotein is reported to be present as early as PanIN lesions, and its expression gradually increases as PDAC progresses (227). In addition, the increase in the expression of tMUC1 was co-related with the grade of PanINs. Overexpression of tMUC1 is evident in PanIN 2 and 3 and further increases with PDA progression (228). All these features make tMUC1 an ideal biomarker for early detection of PDAC. TAB004 antibody, which recognizes the exposed epitopes in tMUC1, exhibits high specificity to tMUC1 in tumor tissue samples of PDAC patients (159). Hence, we hypothesize that a TAB004-targeted MSN-based imaging probe can be used for the specific bioimaging as well as the detection of PDAC at early stages.

4.1.3 Nanomaterials are ideal candidates for the diagnosis of cancer.

Nanomaterials have been extensively investigated for developing novel probes and therapies to improve existing cancer diagnostic and treatment strategies (68, 69). For PDAC, several nanomaterials have been investigated for detection using targeted biomarkers (77, 78) and for combinational therapies (68, 80-83). In this project, we investigated tMUC1-specific MSN nanoprobe for specific imaging and possible non-invasive probe for the detection of PDAC at early stages (PanIN 2-3).

4.1.3.1 MSNs for selective cancer imaging and diagnosis.

We have recently demonstrated the safety and targeting of TAB004 antibody

functionalized MSNs in a genetically engineered breast cancer mouse (MMT) model (229). TAB004-MSN material was used as an optical probe for selective breast cancer detection (**Figure 4.2a**). The TAB004-MSN imaging probe was shown to selectively accumulate in tumors of MMT mice, which overexpress human tMUC1 (229). On the contrary, Mtag mice, which similar to MMT, spontaneously develops breast tumors, but overexpress mouse homolog of tMUC1, do not show significant accumulation of TAB004-MSN (**Figure 4.2b**). These preliminary results demonstrate the safety and targeting ability of TAB004-MSN platform towards tMUC1 antigen and promise their potential in PDAC imaging.
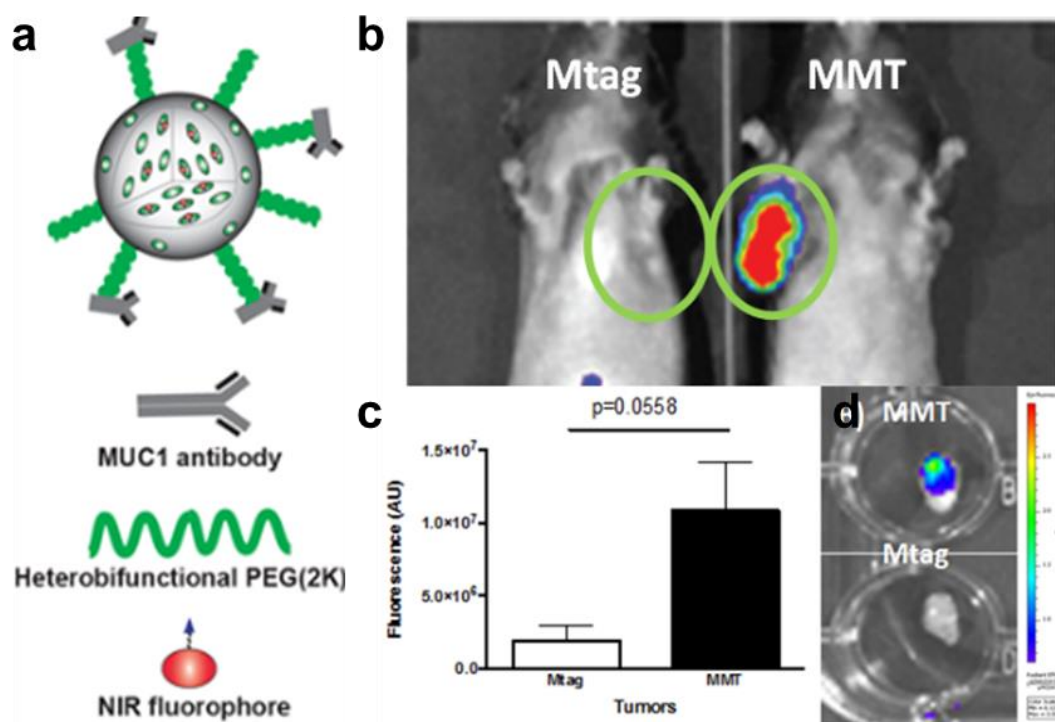
Figure 4.2. TAB004-MSNs for selective detection of breast cancer. **(a)** MSNs were chemically functionalized with a NIR-797 dye and a heterobifunctional polyethylene glycol (PEG) linker, which was further conjugated to the TAB004 antibody. **(b)** Fluorescent signals captured by IVIS Imaging system after intravenous injection with TAB004 in MMT nad Mtag mice. *Ex vivo* NIR fluorescence signals **(c)** and quantification of the NIR fluorescence signal **(d)** intensities in tumors harvested from Mtag and MMT mice (19).

4.2 Experimental section.

4.2.1 Synthesis TAB004-MSNs used for *in vitro* studies.

4.2.1.1 Synthesis of MSNs.

MSNs were synthesized following our previous procedures with slight modifications (163, 164). Briefly, the surfactant CTAB (0.78 g, 2.14 mmol) was dissolved in a mixture of ethanol (3.32 mL) and nanopure water (21.6 mL), followed by the addition of DEA (41.4 µL, 0.428 mmol). This surfactant mixture was stirred for 30 min at 60 ºC. To this solution, TEOS was added dropwise over a period of 5 minutes. The resulting suspension was stirred for 18 h at 60 ºC. MSNs were then collected via centrifugation at 13,000 rpm for 15 minutes, washed with ethanol three times and stored in ethanol.

The surfactant template was extracted by washing the MSNs in 1M HCl methanolic solution (10 mg of MSNs in 1 mL of the acid solution). The MSNs were dispersed in the acidic solution and stirred for 10 h at 60 ºC. MSNs were then collected via centrifugation and washed with ethanol three times. A second acid wash was performed under the same conditions for 6 h. Finally, the surfactant-free MSNs were washed with ethanol three times and stored in ethanol.

4.2.1.2 Synthesis of post-synthetically grafted AP-MSNs.

MSNs (100 mg) were dispersed in ethanol (40 mL), and APTES (20 µL, 85.3 µmol) was added to the MSN dispersion. The reaction was stirred for 24 h at 60 ºC. MSNs were then collected via centrifugation, washed three times with ethanol to afford post-synthetically grafted AP-MSNs (Pg-AP-MSNs).

4.2.1.3 Synthesis of TRITC labeled MSNs.

4.2.1.3.1 Synthesis of TRITC-silane derivative.

TRITC silane derivative was prepared by dissolving TRITC (1.87 mg, 4.23 µmol) in 1 mL of DMF. APTES (5.0 µL, 21.3 µmol) was then added to the TRITC solution and stirred for 3 hours at room temperature. As-synthesized TRITC-silane was used without any purification.

4.2.1.3.2 Synthesis of TRITC-MSNs.

Pg-AP-MSNs (100 mg) were dispersed in 40 mL of ethanol, and as-synthesized solution of TRITC silane derivative was added to the MSNs dispersion. The mixture was stirred for 24 h at 60 ºC in the dark. MSNs were finally collected by centrifugation, washed thrice with ethanol to afford TRITC-MSNs.

4.2.1.4 Synthesis of PEG-TRITC-MSNs and Mal-TRITC-MSNs.

TRITC-MSNs (10 mg) were dispersed in 5 mL of anhydrous acetonitrile. MeO-PEG-NHS or Mal-PEG-NHS (10 mg) was added to the TRITC-MSN dispersion and stirred for 48 h. Post reaction, the MSNs were collected by centrifugation, washed once with acetonitrile, twice with ethanol and stored in ethanol.

4.2.1.5 Synthesis of TAB004-TRITC-MSNs.

The TAB004 antibody was modified to introduce free sulfhydryl groups as described in the section 2.2.3.6.1. Sulfhydryl modified TAB004 was conjugated to Mal-PEG-TRITC-MSNs via maleimide-thiol chemistry to afford TAB004-TRITC-MSNs according to the procedure reported in section 2.2.3.6.2.

4.2.2 Synthesis of TAB004-MSNs used for in vivo experiments.

4.2.2.1 Synthesis of MSNs.

MSNs were synthesized according to the procedure described in the section 4.2.1.1.

4.2.2.2 Synthesis of phosphonate grafted and NIR-labelled MSNs.

4.2.2.2.1 Synthesis of NIR-silane derivative.

NIR silane derivative was synthesized by dissolving NIR (1.65 mg, 1.87 µmol) in DMF (1 mL). Then APTES (3.9 µL, 16.6 µmol) was added to the NIR solution and stirred for 3 h at room temperature. As-synthesized solution of NIR-silane derivative was used without any further purification.

4.2.2.2.2 Synthesis of Phos-NIR-MSNs.

To synthesize MSNs labeled with NIR-797, MSNs (200 mg) were dispersed in nanopure water (13 mL). An aqueous solution of TPMP (113.5 µL, 0.2 mmol in 13 mL, pH adjusted to 6-7) was added to the MSN dispersion. The reaction mixture was stirred for 3 h at 40 ℃. To this reaction, as-synthesized NIR-silane derivative (described in the previous section) was added to the MSN mixture under stirring. The mixture was further allowed to stir for an additional 3 h at 40 ℃ covered from light. The MSNs were finally collected via centrifugation, washed three times with ethanol, and stored in ethanol to afford Phos-NIR-MSN.

4.2.2.3 Synthesis of PEI-coated MSNs.

MSNs were coated with PEI polymer using a procedure previously reported (132). Phosphonate-grafted MSNs (Phos-MSN or Phos-cisPt-MSN, 100 mg) were dispersed in ethanol (40 mL). A PEI solution (1.8 KDa, 10 mL, 2.5 mg/mL in ethanol)

was added to the MSN dispersion and stirred for 1 h at room temperature. The nanoparticles were collected via centrifugation and washed thrice with ethanol to afford PEI-MSN.

4.2.2.4 Synthesis of PEG-MSNs or Mal-PEG-MSNs.

PEI-MSNs (30 mg) were dispersed in 15 mL of anhydrous acetonitrile. MeO-PEG-NHS or Mal-PEG-NHS (15 mg) was then added to the MSN dispersion. The mixture was stirred for 48 h at room temperature in the dark. The MeO-PEG-MSNs or Mal-PEG-MSNs were finally collected via centrifugation, washed with ethanol 3 times, and stored in ethanol.

4.2.2.5 Synthesis of TAB004-MSNs.

The TAB004 antibody was modified to introduce free sulfhydryl groups as described in the section 2.2.3.6.1. Sulfhydryl modified TAB004 was conjugated to Mal-PEG-TRITC-MSNs via maleimide-thiol chemistry to afford TAB004-TRITC-MSNs according to the procedure reported in section 2.2.3.6.2.

4.2.3 *In vitro* studies.

Cell culture conditions are described in the section 2.2.6.1. PDAC cells KCM, KCKO, and HPAF II were used for the *in vitro* studies. For cellular uptake studies, KCKO cells were used as control. KCKO are transgenic mice which do not express the human MUC1, and the cells generated from the spontaneous PDA tumors from KCKO mice are used as a control in this study (140). KCM and KCKO cells were generously provided by Dr. Mukherjee (UNC Charlotte).

4.2.3.1 In vitro targeting ability of TAB004-MSNs.

Quantitative determination of cellular uptake was carried out using flow

cytometry. Briefly, PDAC cells KCM, KCKO, and HPAF II were seeded in 24 well plates at a density of 20,000 cells per well and incubated for 24 h. The MSNs (20, 40, and 80 µg/mL) prepared in complete cell culture media were added to the cells and treated for 24 h. The cells were washed with PBS three times, detached using trypsin and centrifuged to collect the cell pellet. The cells were resuspended in PBS and were immediately analyzed using BD LSR Fortessa flow cytometer. The results are reported as the percentage of TRITC positive cells (average ± SD) obtained from three independent experiments.

Qualitative cellular uptake was carried out using confocal microscopy. KCM cells were seeded on glass slides placed in 6 well plates at a density of 50,000 cells per well and incubated for 24 h. The MSNs (40 µg/mL) prepared in complete cell culture media were added to the cells and treated for 24 h. The cells were washed with PBS three times and cell nuclei were stained with DAPI for 30 min. Post staining, the cells were washed with PBS again to remove excess stain and immediately imaged using an Olympus Fluoview FV 1000 confocal fluorescence microscope.

4.2.4 *In vivo* targeting ability of TAB004-MSNs in KCM syngeneic mice.

The syngeneic mice were established as per the procedure described in the section 2.2.7.1. The targeting ability of the TAB004-MSNs was evaluated in the syngeneic KCM mice 7 days post of cell implantation. The KCM tumor-bearing mice were injected intravenously with 40 mg/Kg of TAB004-MSNs. The mice were imaged prior to the administration of the MSN material and at 30 min, 1, 4, 24, 48 and 96 h post injection using the IVIS® Spectrum imaging system (PerkinElmer). The images were analyzed using the Living Image® Software (version 4.5.5, PerkinElmer). The mice were

euthanized after 96 h and the major organs including liver, lungs, kidneys, spleen and tumor, were collected. The *ex vivo* fluorescence associated with the organs was measured using the IVIS imaging system.

4.2.5 *In vivo* targeting ability of TAB004-MSNs in PDA.MUC1 mice.

The PDA.MUC1 mice were generated as described in section 2.2.8.1. PDA.MUC1 mice 8, 12, and 27 weeks post tamoxifen induction were injected intravenously with 40 mg/Kg of TAB004-MSNs.). The mice were imaged prior to the administration of the MSN material and at 30 min, 1, 4, 24, 48 and 96 h post injection using the IVIS® Spectrum imaging system (PerkinElmer). The images were analyzed using the Living Image® Software (version 4.5.5, PerkinElmer). The mice were euthanized after 96 h and the major organs including liver, lungs, kidneys, spleen and tumor, were collected. The *ex vivo* fluorescence associated with the organs was measured using the IVIS imaging system. The pancreas was weighed and fixed in formalin. The pancreas was sectioned at 4 um thickness at various tissue depths. A total of 4 sections were stained with H&E and imaged to determine the PanIN lesion and PDA stage.

4.2.6. Statistical analysis.

All the data in this chapter is represented as mean ± SD unless mentioned otherwise. Cellular uptake using flow cytometry was evaluated with a minimum of 5000 gated cells. The cellular uptake was quantified in triplicates. The statistical analysis was performed with One-way ANOVA using Tukey's multiple comparison test. All the statistical analysis were performed using GraphPad Prism (v8.2.0 for Windows, La Jolla California, CA, USA) with $\alpha=0.05$ and reported as stars assigned to the p values; ****$p \leq 0.0001$, ***$p \leq 0.001$, ** $p \leq 0.01$, * $p \leq 0.05$ and ns $p > 0.05$.

4.3 Results and Discussions.

4.3.1 *In vitro* targeting ability of TAB004-MSNs

The specific accumulation of TAB004-MSNs in tMUC1 expressing PDAC cells was evaluated using flow cytometry and confocal microscopy. PEG-MSNs were used as controls. PDAC cells, KCM and HPAF II were incubated with different concentrations of TRITC labeled TAB004-MSNs and PEG-MSNs for 24 h. The cellular internalization data obtained in KCM cells showed concentration-dependent MSN internalization and about 5-fold increased TRTC-positive KCM cells when treated with TAB004-MSNs compared to the untargeted PEG-MSNs ($p<0.001$) (**Figure 4.3a**). Similarly, HPAF II cells treated with TAB004-MSNs showed approximately 2.5-fold increased cellular uptake compared to the untargeted PEG-MSNs ($p<0.001$) (**Figure 4.3b**). Thus, demonstrating the higher cellular uptake of MSNs functionalized with tMUC1 specific TAB004. The cellular uptake of MSNs was further evaluated using confocal microscopy. The micrographs indicate that KCM cells treated with TAB004-MSNs exhibit increased TRITC fluorescence associated with the cells compared to PEG-MSNs, which confirmed the findings from flow cytometry data (**Figure 4.3c**).
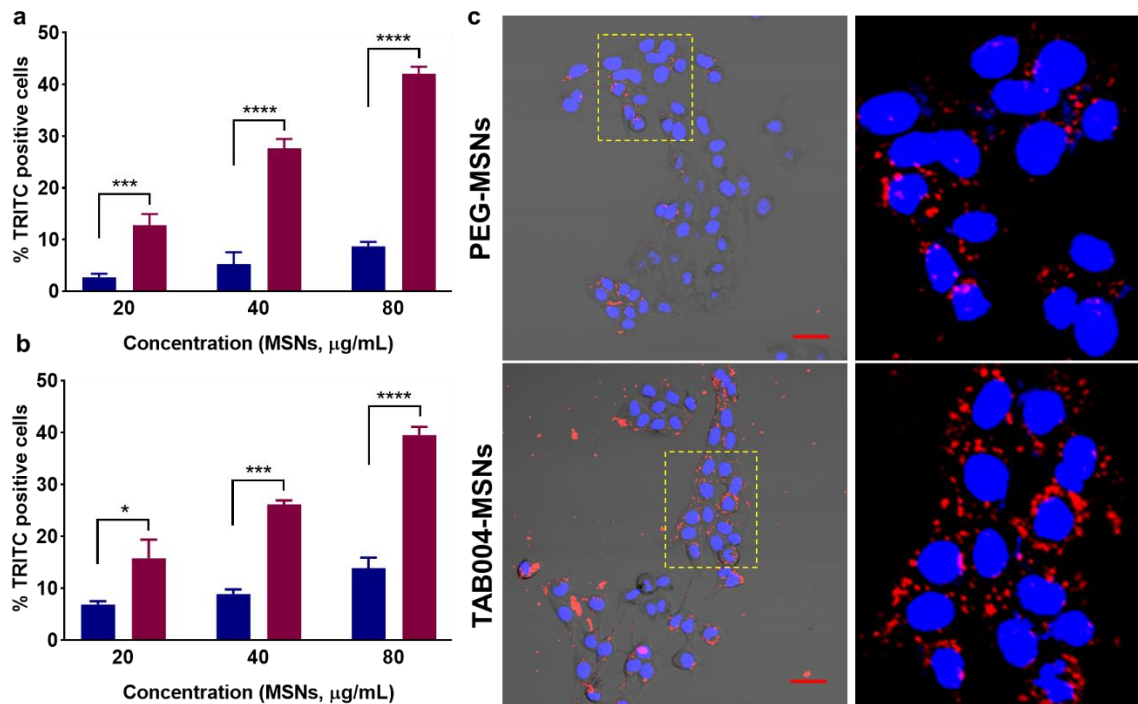
Figure 4.3. *In vitro* cellular targeting of TAB004-MSNs. Flow cytometry data for the cellular uptake of PEG-MSNs (blue) and TAB004-MSNs (red) at 20, 40, and 80 μg/mL in murine PDAC KCM cells **(a)** and human PDAC HPAF II cells **(b)** after 24 h of incubation. The data is represented as mean ± SD in triplicate. One-way ANOVA using Tukey's multiple comparison test; ****$p \leq 0.0001$, ***$p \leq 0.001$, ** $p \leq 0.01$, * $p \leq 0.05$ and ns $p > 0.05$. **(c)** Confocal images of KCM cells after incubation with PEG-MSNs and TAB004-MSNs (40 μg/mL) for 24 h. Overlay of the blue channel, which shows to the nuclei stained with Hoechst dye, the red channel which shows the TRITC fluorescence associated to the MSNs, and DIC channel (scale bar = 20 μm).

KCM cells overexpress human tMUC1 whereas KCKO cells lack the human tMUC1 expression (140). The specificity of the TAB004-MSNs to recognize the tMUC1 was assessed by determining their differential uptake in KCM and KCKO cells. KCM and KCKO cells were treated with both TAB004-MSNs and PEG-MSNs for 24 h. The cellular uptake data depicted in **Figure 4.4a,** indicate that TAB004-MSNs were taken up by KCM cells at increased levels compared to the KCKO cells. Indeed, uptake of MSNs in KCKO cells was not significantly different between the targeted and untargeted MSNs (**Figure 4.4b).** The increased cellular uptake of targeted TAB004-MSNs in tMUC1

expressing KCM and HPAF II cells is be attributed to the receptor-mediated endocytosis due to the interaction of TAB004 with tMUC1 on the cell surface (184).
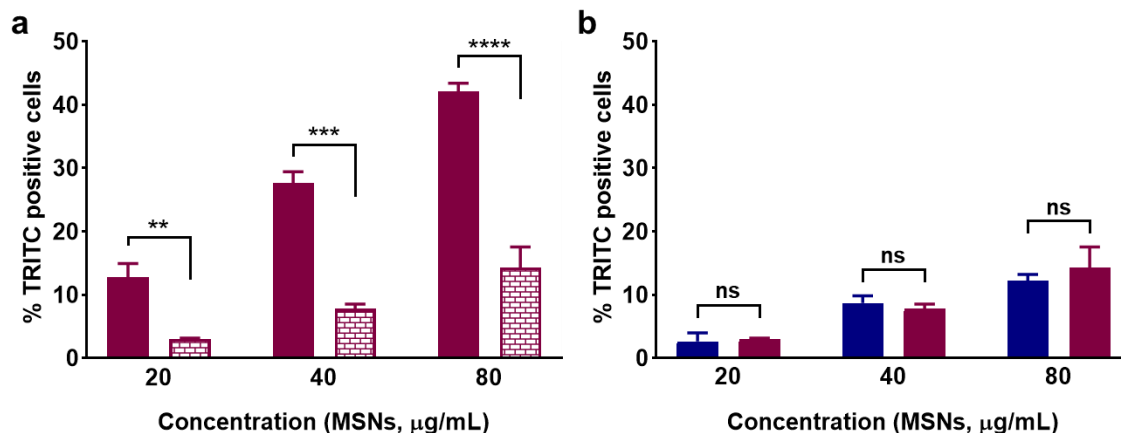
Figure 4.4. In vitro specificity and targeted ability of TAB004-MSNs. Flow cytometry data for the cellular uptake of TAB004-MSNs at 20, 40, and 80 μg/mL in KCM cells (solid red) and KCKO cells (brick-patterned red) after 24 h of incubation. (b) cellular uptake of TAB004-MSNs (red) and PEG-MSNs (blue) at 20, 40, and 80 μg/mL in KCKO cells after 24 h of incubation. The data is represented as mean ± SD in triplicate. One-way ANOVA using Tukey's multiple comparison test; ****$p \leq 0.0001$, ***$p \leq 0.001$, ** $p \leq 0.01$, * $p \leq 0.05$ and ns $p > 0.05$.

4.3.2 *In vivo* targeting ability of TAB004-MSNs in syngeneic KCM mice.

After the successful demonstration of the selectivity and targeting ability TAB004-MSNs in PDAC cells, we further investigated their targeting ability in syngeneic KCM mice. We have previously shown that TAB004-MSNs were safe and can selectively accumulate in the breast cancer tumors in MMT mouse model (163). NIR labeled TAB004-MSNs (40 mg/Kg) were intravenously injected in KCM tumor-bearing mice 7-day post KCM cell implantation i.e., when the tumors reached volumes of 100 mm^3. NIR fluorescence was used to track the distribution of MSNs in the mice by imaging the fluorescence in the abdominal region and tumor region (right flank of the mice) at 4, 24 and 48 h post-injection. The fluorescence images show the accumulation of the TAB004-MSN in the tumor region at as early as 4 h after intravenous injection of

TAB004-MSN (**Figure 4.5a**). The mice were euthanized after 96 h and the *ex vivo* fluorescence images of the tumors demonstrate a higher accumulation of MSNs in mice injected with TAB004-MSNs (**Figure 4.5b**). The primarily investigation of TAB004-MSNs demonstrate their tumor accumulation in simple syngeneic model.
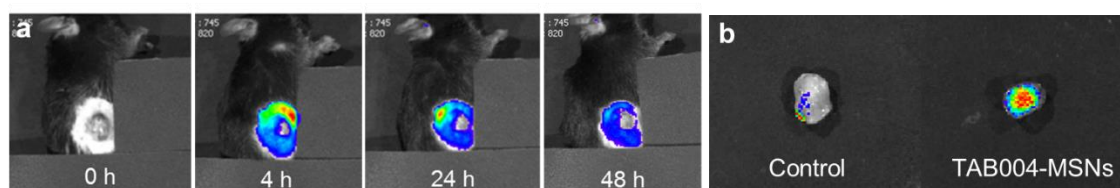
Figure 4.5. *In vivo* targeting ability of TAB004-MSNs. **(a)** KCM syngeneic mice were intravenously injected with TAB004-MSNs and imaged 4, 24, and 48 h post nanoparticle injection. **(b)** *Ex vivo* NIR fluorescence associated with the tumors harvested 96 h post nanoparticle injection.

4.3.3 *In vivo* targeting ability of TAB004-MSNs in PDA.MUC1 mice.

As emphasized in earlier chapters, cell line-based models have predictive value, however, they lack genetic and phenotypic heterogeneity and hence, cannot showcase the early stages of human cancers (136). Genetically engineered mice models (GEM) recapitulate the progression of PDAC similar to that in humans and are better models to demonstrate early diagnostic capability of nanoprobes (138). PDA.MUC1 mice are triple transgenic which develop full spectrum of PDAC from the preinvasive lesions to invasive carcinoma when the oncogenesis is initiated with tamoxifen. To assess the potential of TAB004-MSN to target and detect early stages of PDAC, before the pre-neoplastic lesions develop to full invasive PDA, we used PDA.MUC1 mice. We investigated the accumulation of TAB004-MSNs in PDA.MUC1 mice at increasing stages of the disease. PDA.MUC1 mice at 8, 12, and 27 post oncogenesis initiation. PDA.MUC1 mice develop PanIN 1 and PanIN 2 lesions at the time points chosen (143).

The PDA.MUC1 mice at 8, 12, and 27 weeks post tamoxifen were injected with 40 mg/Kg of NIR-labeled TAB004-MSNs (**Figure 4.6a**). Mice were euthanized 96 h post nanoparticle injection and pancreas was harvested. Though we collected whole-body images to understand the distribution of MSNs at various time intervals, the whole-body fluorescence images do not provide any information on the accumulation of the MSNs in the pancreas. This is due to the positioning of the pancreas (behind the liver and stomach) and the accumulation of all nanoparticles in the liver. Therefore, end-point e*x vivo* NIR fluorescence from the pancreas is the reliable approach to understand MSN accumulation in pancreas. As depicted in **Figure 4.6b**, the NIR fluorescence associated to pancreas indicate the accumulation of TAB004-MSNs in the pancreas as early as weeks 8 and 12.

Interestingly, the amount accumulated of TAB004-MSNs in the pancreas showed to be associated with the progression of the disease; higher accumulation was observed in PDA.MUC1 mice at week 12 compared to the one at week 8. Upon analysis of the H&E stained micrographs from the pancreas of the PDA.MUC1 mice at weeks 8 and 12, we confirmed the presence of PanIN 1 and PanIN 2 grade lesions (**Figure 4.6c**). Our preliminary data show strong evidence that the TAB004-MSN can detect PDAC in stages as early as PanIN 1 and PanIN 2 lesions in a clinically relevant GEM model.
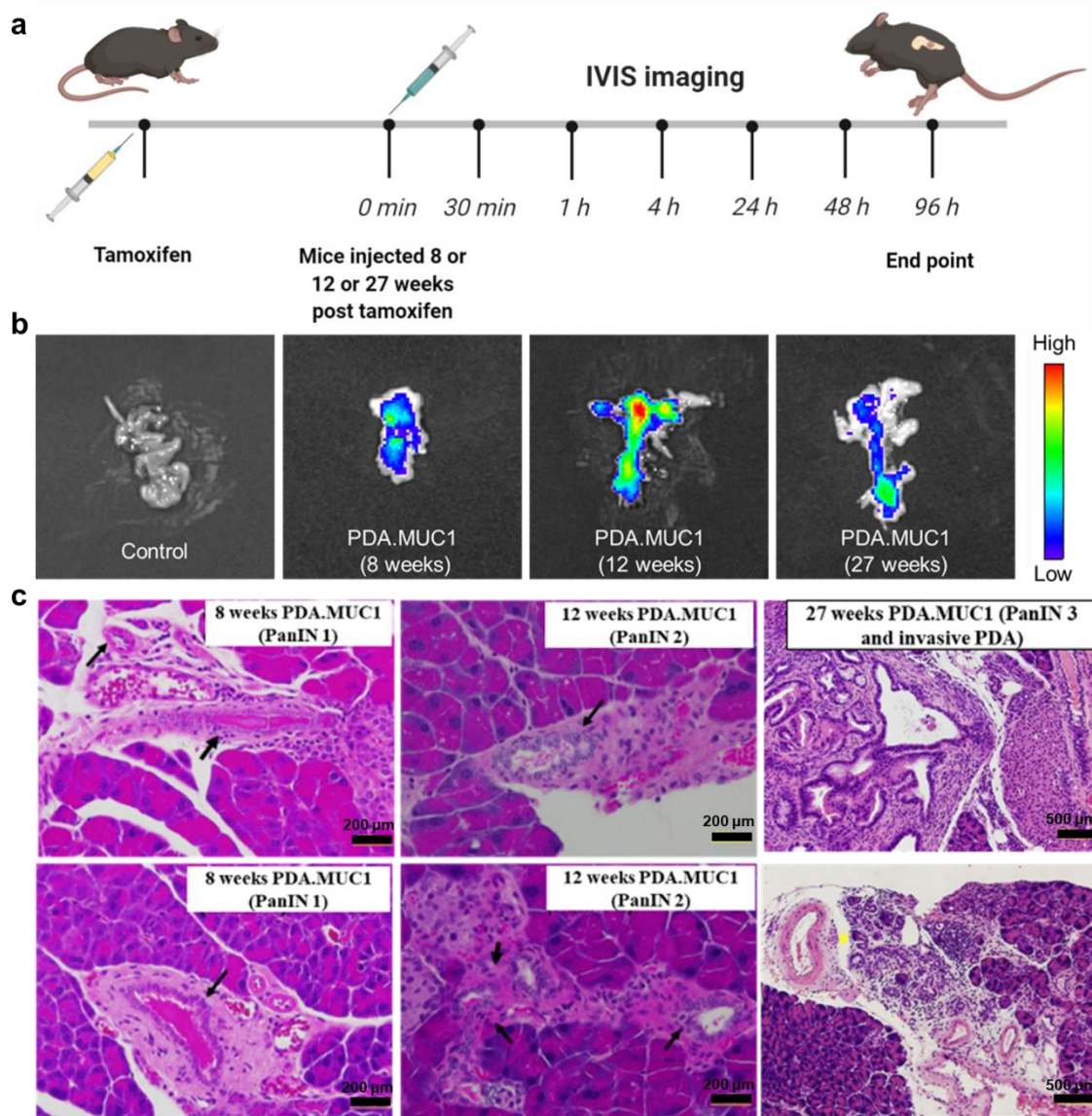
Figure 4.6. TAB004-MSNs' ability to detect PDAC at early stages. **(a)** Imaging regimen followed using PDA.MUC mice at 8, 12, and 27 weeks post tamoxifen. Mice were intravenously injected with 40mg/Kg of TAB004-MSNs and imaged at various time points after injection. The mice were euthanized 96 h post MSNs injection. **(b)** *Ex vivo* NIR fluorescence associated with the pancreas; control, and PDA.MUC1 mice at weeks 8, 12, and 27 post tamoxifen. **(c)** H&E images of the pancreas showing the presence of PanIN 1 and 2 lesions in PDA.MUC1 mice (black arrows).

4.4 Conclusions.

Improvement in early detection of PDAC as well as non-invasive imaging can have significant impacts on the prognosis of this disease. Early detection can increase the percentage of patients for potentially curative surgery and increase the success rate of

other therapeutic options. Herein, we investigated the potential of a target-specific MSN-based nanoprobe, TAB004-MSNs for selective bioimaging, tumor accumulation, and early detection of PDAC.

TAB004-MSNs showed increased cellular uptake in tMUC1 expressing KCM and HPAF II cells which is be attributed to the receptor-mediated endocytosis due to the interaction of TAB004 with tMUC1 on the cell surface. In addition, we clearly demonstrated the selectivity of TAB004-MSNs by their differential uptake in KCM and KCKO cells. We next tested the tumor accumulation of TAB004-MSNs in KCM syngeneic mice and they exhibited increased tumor accumulation. More importantly, our investigation of TAB004-MSNs in PDA.MUC1 mice indicate that the specific nanoprobe can selectivity accumulate in the pancreas at early PanIN lesion stage. Hence, TAB004-MSNs can be a potential nanoprobe for the early diagnosis of PDAC with further modifications.

Our design has some drawbacks, the size of the nanoparticles and their slow degradation hinder the potential imaging application. Hence, we have investigated research on the small sub-20 nm MSNs and we further plan to increase the biodegradability of the material. The small MSNs can significantly change in the biodistribution, leading to higher accumulation in PanIN lesions and PDAC accompanied by increased clearance (230). This can further enhance the detection capabilities of the TAB004-MSN by higher accumulation and retention in the pancreas, providing a longer window compared to the free TAB004 antibody obtaining higher sensitivity and specificity from the target site (231).

CHAPTER 5: Summary and future directions

5.1 Overall summary.

PDAC is an aggressive cancer exhibiting high mortality, with a 5-year survival rate of 9%, that has not significantly improved over the past 40 years. Various factors contribute to the devastating state of PDAC patients including late diagnosis, high metastatic burden, inherent and acquired resistance to systemic therapies, and abundant desmoplastic stroma. Hence, it is imperative to investigate on reliable, novel and improved methods for the detection and treatment of PDAC. Nanomedicine has great potential in the treatment and imaging of PDAC, especially mesoporous silica nanoparticle (MSN)-based modalities, owing to their outstanding properties such as high surface area, tunable particle and pore diameters, external and internal surface for high drug loading and facile functionalization. Herein novel MSN-based modalities are reported to address various drawbacks in PDAC therapy (**Figure 5.1**).
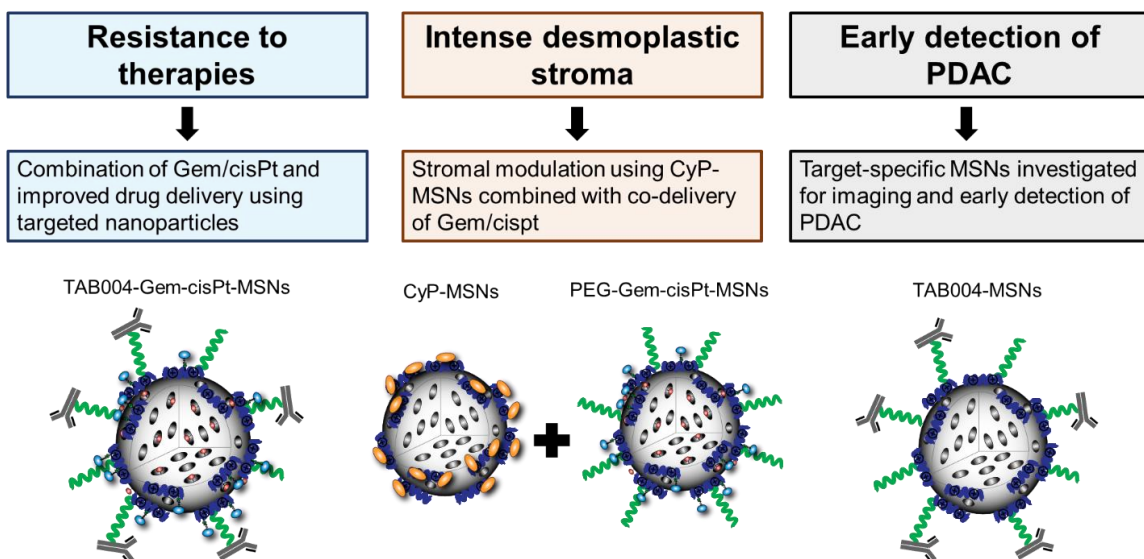
Figure 5.1. Overview of MSN-based therapeutic and imaging modalities investigated in this Thesis.

5.1.1 tMUC1-Targeted combinatorial drug delivery using mesoporous silica nanoparticles for improved therapy of PDAC

Systemic therapies, importantly chemotherapy is the mainstay for PDAC maintenance in the clinic. To improve the drawback in chemotherapy including inadequate/insufficient drug delivery, resistance, rapid drug degradation, systemic toxicities, we hypothesized an MSN-based combination chemotherapy using Gem/cisPt to efficiently co-deliver potent chemotherapy drugs to PDAC tumors, decrease systemic leakage and systemic toxicities. Our nanoplatform consisted of localizing cisPt in the interior porous surface and Gem to the external surface of the MSN. By doing so we exploited the unique structural features of the MSN along with controlled/uniform conjugation of drugs at high loading, limiting batch-to-batch variability. Our design criterion also involved chemical conjugation of chemotherapy drugs to provide uniform ratio maintenance, eliminate or at a minimum reduce toxicity in healthy organs. Moreover, the chemical linkages between the drugs and MSNs are stimuli-responsive i.e., the drugs are released in a controlled fashion in the tumor and cancer cells under their reductive environment. Further improving the nanocarrier localization in the tumors, our nanoplatform was functionalized with a novel antibody TAB004 that recognizes specific tumor-associated MUC1 (tMUC1) antigens overexpressed on pancreatic cancer cells.

As envisioned, we successfully synthesized TAB004-Gem-cisPt-MSNs through a multistep process yielding 5.13 ± 0.9 wt% cisPt and 23.9 ± 2.6 wt% Gem. Our thorough *in vitro* investigation showed that dual drug conjugated MSNs (Gem-cisPt-MSNs) outperformed both single-drug MSNs and their physical mixture. The Gem-cisPt-MSNs exhibited lower IC_{50} compared to the other materials, yet increased DNA damage and cell

apoptosis.
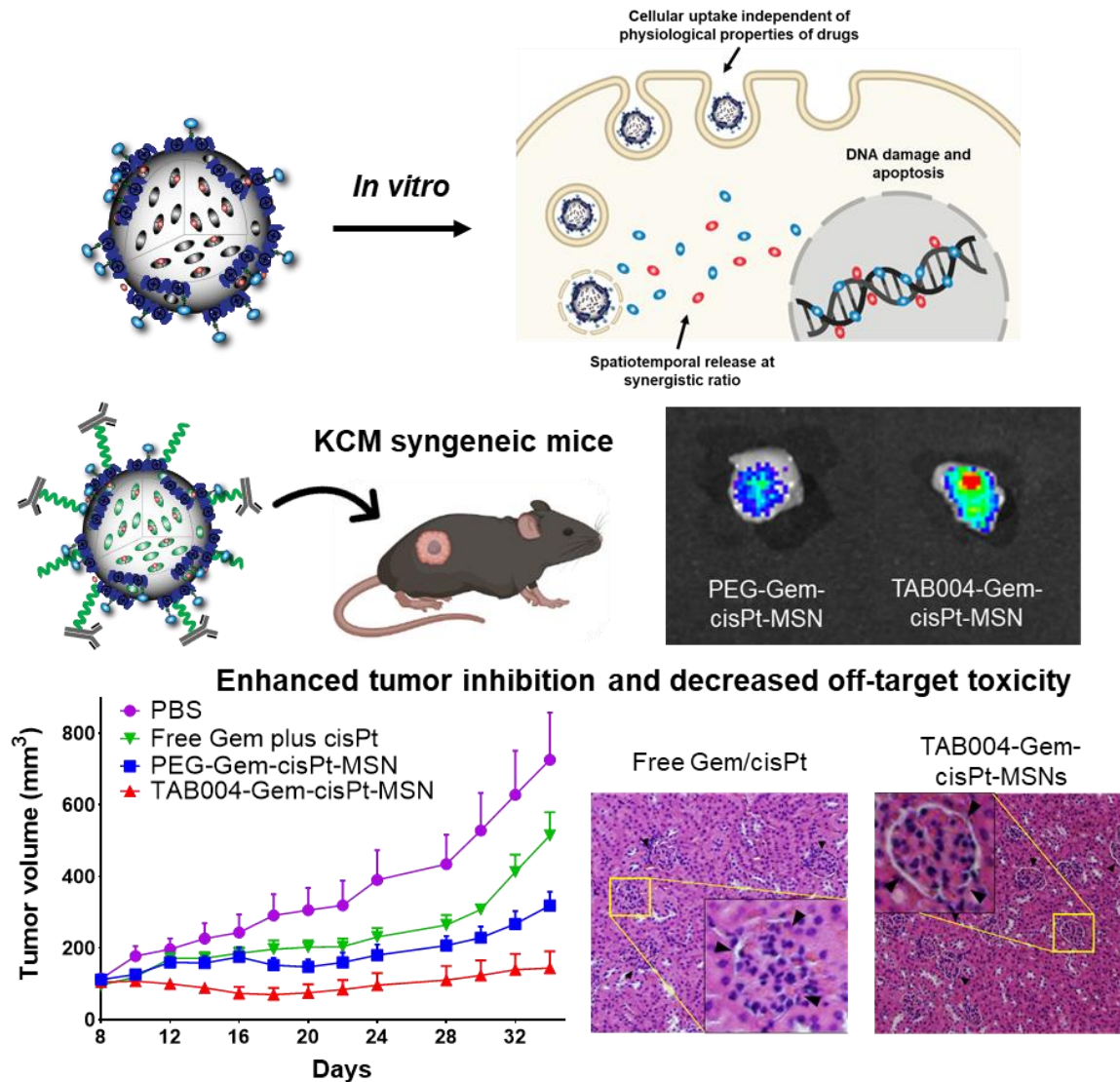
Figure 5.2. Gem-cisPt-MSNs showed efficient delivery co-delivery of Gem/cisPt leading to DAN damage and apoptosis. The MSN platform was functionalized with novel tMUC1-specific antibody (TAB004) for targeted drug delivery. The TAB004-Gem-cisPt-MSNs showed increased accumulation in the tumors, which outperformed the untargeted MSN material as well as free Gem/cisPt. Our nanoplatform showed no systemic toxicities in KCM syngeneic mice

Regardless, in the light of current experimental results, we conclude that the spatiotemporal release of drugs at a synergistic ratio resulted in the increased cytotoxic effect observed in PDAC cells. The rational design of MSNs i.e., the localization of cisPt

in the porous internal surface and Gem localization on the external surface may result in an in-situ time-differed release of each drug. Such drug release kinetics significantly contribute to the enhanced activity of Gem-cisPt-MSNs when compared to co-incubation with Gem and cisPt by themselves. Cancer cells preincubated with Gem were associated with increased combination effect of Gem/cisPt. We are currently exploring the role of *in situ* differential delivery of Gem vs cisPt drug by our nanoplatform Gem-cisPt-MSNs.

In vivo investigation targeting and therapeutic effects of TAB004-Gem-cisPt-MSNs in KCM syngeneic mice, highlighted an increased uptake of TAB004-functionalized MSNs in tumors when compared to the non-targeted MSNs. This increased tumor accumulation lead to an enhanced tumor growth inhibition compared to non-targeted MSNs as well as to free drugs. Further, TAB004-Gem-cisPt-MSNs nanoplatform was not associated with any sign of interference with normal organ function, whereas off-target damages were observed in mice treated with free drugs. The encouraging *in vivo* studies in syngeneic KCM mice prompted preliminary efficacy studies in the robust genetically engineered mice PDA.MUC1 mouse model.

5.1.2 CyP-MSNs and PEG-Gem-cisPt-MSNs sequential combination for tumor stroma modulation and improved drug delivery for PDAC.

One of the major hallmarks of PDAC is the desmoplastic stroma where the intricate and dynamic crosstalk between cancer cells and stromal cells is dynamic and contributes to tumor progression and metastasis. Stroma causes elevated interstitial pressure, reduced blood flow, hypovascularity and acts as the physical barrier to drug delivery while it also contributes to increased resistance due to off-target toxicity of stromal cells. One of the most studied mediators of cancer cell-stroma crosstalk is the

sonic hedgehog pathway leading to the intense desmoplasia observed in PDAC tumors. Inspired by recent studies and current clinical investigation of SHh inhibitors, we designed an MSN-based sequential therapy for primary stroma modulation and secondary chemotherapy delivery for improved PDAC treatment. Sequential delivery of CyP and Gem/cisPt using separate nanocarriers can control the time-dependent and spatial access of drug which have different targets in the tumors. Hence, we developed a sequential combination that includes stroma modulating treatment using CyP-MSNs plus PEG-Gem-cisPt-MSNs.

We successfully synthesized and characterized CyP-MSNs which indicated high CyP loading. With an intent is to block the crosstalk between PDAC cells and stromal cell, not necessarily lead to the death of either types of cells. and tested in PDAC cells, we chose low concentrations of CyP-MSNs. As intended, the combination therapy of CyP-MSNs plus Gem-cisPt-MSNs showed no effect on the HPAF II cells. Fine tuning of CyP and Gem/cisPt delivery is another parameter which we controlled through the time-staggered sequential delivery of these drugs. The sequential combination of CyP-MSNs plus PEG-Gem-cisPt-MSNs therapy in an aggressive HPAF II tumor bearing mice showed increased tumor inhibition. In addition, tumor analysis indicated changes in the collagen deposition in the tumors which is a primary stromal ECM component.
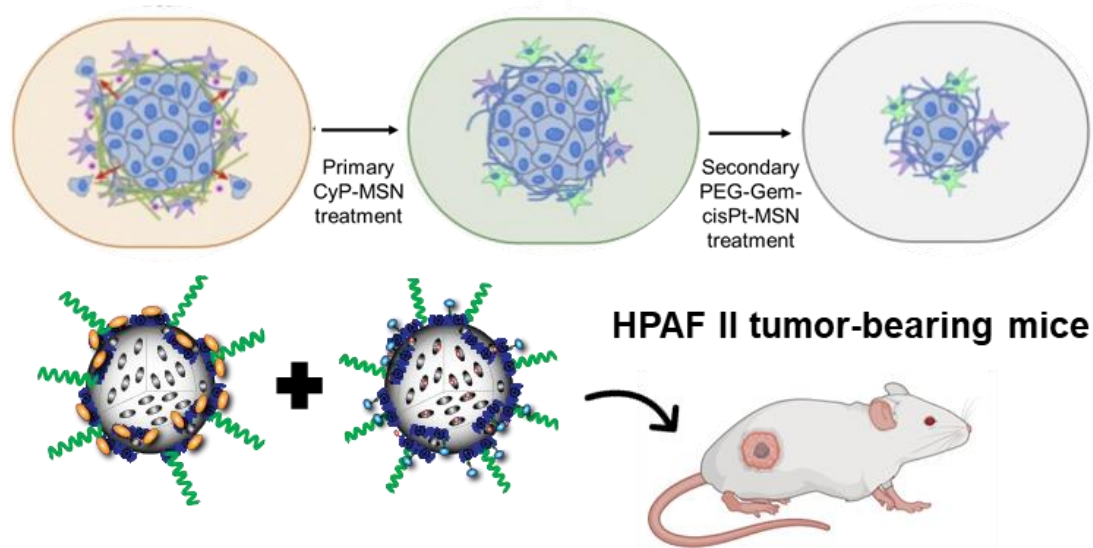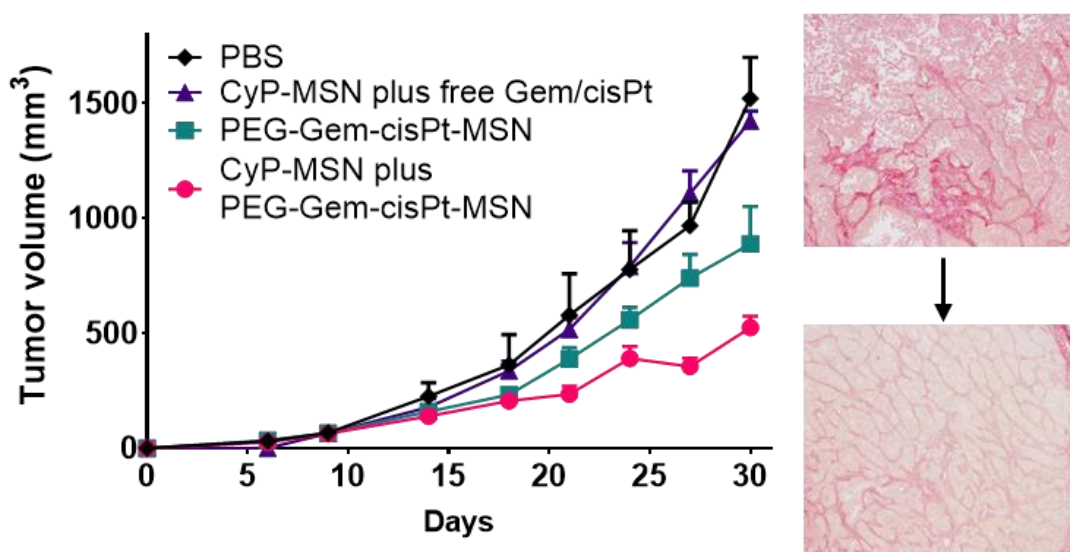
Figure 5.3. Sequential therapy was designed to combat the stromal barrier via CyP-MSNs and improved Gem/cisPt delivery using PEG-Gem-cisPt-MSNs. The time-staggered sequential combination therapy of CyP-MSNs plus Gem-cisPt-MSNs showed increased tumor inhibition as well as changes in the ECM deposition in an aggressive HPAF II tumor-bearing mice

We are currently studying the tumor stromal changes in detail with cancer-associated fibroblast markers and alterations in the blood vessels in the tumor. In addition, upon testing this combination on the HPAF +++ cells, cancer stem-like cells, we observed dramatic benefit in cytotoxicity compared to the Gem-cisPt-MSNs alone.

These results indicate the potential of using our combination to deplete the PDAC tumors of cancer stem-like cells which are responsible for resistance and recurrence which needs to be explored in detail in the future. Taken together, the nanoparticle-based sequential combination can lead to enhanced therapeutic efficacy in PDAC. Future studies involving orthotopic mice models which can mimic the desmoplastic stroma o the PDAC tumors needs to be evaluated.

5.1.3 TAB004-MSN as nanoprobe for bioimaging and early diagnosis of PDAC.

As emphasized throughout this Thesis, the bioimaging and early detection of PDAC is critical and can significantly improve the prognosis of PDAC. Target specific TAB004-MSNs had increased selectivity towards tMUC1-expressing PDAC cells. More importantly, TAB004-MSNs selectivity accumulate in the pancreas at the early PanIN lesion stage. Hence, with some modifications, TAB004-MSNs may serve as a nanoprobe for the early diagnosis of PDAC. Our platform as presented and investigated, has some limitations. As the size of nanoparticles is one of the primary factors which affect the accumulation and thus detection ability. Indeed, previous work demonstrated that the nanoparticle size governs their biodistribution and pharmacokinetics. In particular, MSNs with sub-20 nm diameter have a different biodistribution with possibly higher accumulation in early stages of pancreatic cancer development. Focusing on sub-20 nm MSNs likely will promote higher accumulation and retention in the pancreas and thus further enhance the detection capabilities of MSNs. Such improvement of MSNs for detection may also provide increased retention in pancreas, in addition to increased accumulation. This can lead to extended imaging/detection and higher sensitivity compared to the use of target specific antibodies. Overall, our data support multimodal

applications of MSNs in PDAC detection and therapy.
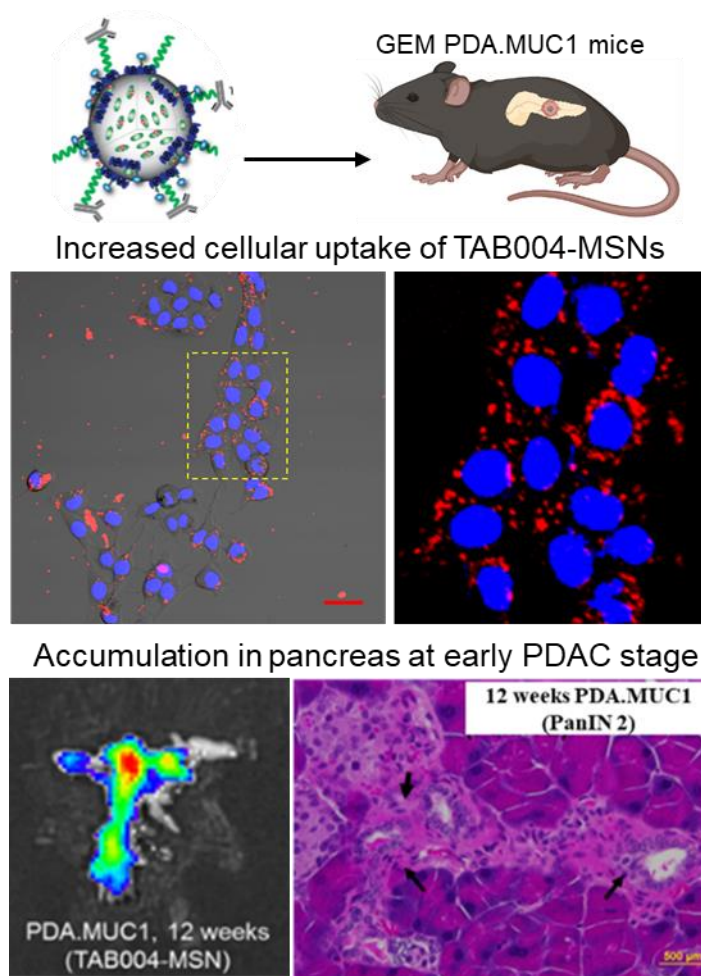
Figure 5.4. The imaging and PDAC detection. Early diagnosis of PDAC is essential to improve PDAC prognosis. In this direction, target specific TAB004-MSNs was used as an imaging and diagnostic probe. TAB004-MSNs demonstrated increased selectivity in tMUC1-expressing PDAC cells. More importantly, TAB004-MSNs could selectivity accumulate in the pancreas at an early PanIN lesion stage.

5.2 Future directions.

We plan to explore additional combinations for the precise co-delivery of drugs building on the knowledge gathered in the investigations of the TAB004-Gem-cisPt-MSN platform. For example, the Gem/PTX combination promotes synergistic drug killing of tumor cells. In addition, PTX increases the active Gem concentration by deactivating cytidine deaminase. Most prevalent in the clinic, the therapeutic Gem/PTX

combination in clinic is accompanied with increased side effects accompanied with this combination. This has led to exploration of Gem/PTX combination using various nanoplatforms like polymeric, liposomes or co-delivery. Thus, the versatility of our MSN-based platform is being explored to conjugate PTX/Gem using redox-responsive chemical linkages. For this therapeutic combination, to further increase the capacity of MSNs, we have recently modified and precisely controlled the pore sizes of the MSNs without increasing the diameter of the nanoparticle (50 nm). Using MSNs with pore size of 6 nm, PTX as a prodrug was conjugated to the internal pores and Gem was conjugated to the external surface.

The tunability of MSN platform has led to a class of high capacity MSNs, which allow countless possibilities and combinations including chemotherapy agents, immunotherapy agents and molecular targeting agents. Furthermore, as cancer mechanisms are shared, such MSNs loaded with specific anti-cancer drug combination likely will benefit patients with other cancer types. For example, we are working on an MSN platform delivery combining PTX/cisPt targeting triple negative breast cancer (TNBC) and the recurrence associated with this disease.

The TME in PDAC is very complicated where the stroma not only acts as a physical barrier but is also involved in intricate communications between cancer cells and stromal cells that promote tumor progression and metastasis. Multiple pathways including TGF-beta, sonic hedgehog, Notch, and CXC12 pathways participate in the crosstalk. Therapeutic intervention of these limits this intense crosstalk and lead to decrease tumor progression. Engineered nanoparticles may be used to inhibit the TME-specific crosstalk and have been explored extensively in the past decade improve the

pancreatic cancer therapy.

Numerous combinations of chemotherapy agents with stroma-modulating agents may be investigated. In the current era of personalized cancer therapy, nanomedicine has an opportunity for personalized nanomedicine. Indeed, the personalized tumor data gathered from genomic and epigenetic profile can guide the therapeutic combination for MSN-based therapy. For example, patients with germline mutation(s), who benefit from Pt-based combinations may be treated with Gem/cisPt-loaded MSNs. Furthermore, stromal component analysis would guide the personalized combination with stroma-modulating agent delivered using MSNs. The relative ease of MSN modifications is crucial to the use and success of MSNs platform for personalized medicine. The drug combinations can be altered and optimized in single nanocarrier prior to clinical use. Optimization with MSNs can be further tailored based on the molecular subtypes of the pancreatic cancer treated furthering personalized therapy.

Moreover, at diagnostic, the PDAC high metastatic burden is a key factor responsible for the poor prognosis. The "Soil and seed" hypothesis suggests that signals within the microenvironment i.e., within the pre-metastatic niche favor the colonization and the growth of cancer cells at the metastatic sites [ref]. In particular, multiple markers especially of inflammation including but not limited to MMPs are associated with the development of premetastatic niches. MSN-based carriers may be designed for the MMP-responsive delivery of TME modifying agents and thus possibly alter the metastatic burden through possible depletion of favorable premetastatic niches. Such MSN carrier may be multifunctional with actions that first deplete the premetastatic niche sites thereby limiting potential of recruitment, colonization and growth of PDAC cells and second

promote primary tumor cell death through for example an efficient chemotherapeutic drug of drug combination. Our sequential therapy MSN platform (discussed in chapter 3) has multiple benefits including the ability of controlling the delivery of molecular agents and drugs based on their spatial and temporal requirements.

Finally, MSN platform related future research include further investigations and biomarker selection for the imaging and therapeutic targeted delivery systems. Here, we explored tMUC1 as the primary marker for diagnosis and targeted therapy. Other markers including can be used for multiplexed imaging.

In Conclusion, MSNs based platform are highly attractive in both detection and treatment of cancers and our data further support their clinical evaluation. Toward a clinical use, the large-scale synthesis and consistency of the MSN platform is critical. Additionally, the long-term effects of Si accumulation in the body and hence, increased degradability of the MSNs needs further investigations. The therapeutic and diagnostic approaches assessed in this thesis support the potential of nanomedicine, especially of MSN-based nanoplatforms and nanoprobes in the improvement of PDAC diagnosis and customizable/personalized therapeutic intervention.

References

1.   De Palma M, Hanahan D. The biology of personalized cancer medicine: Facing individual complexities underlying hallmark capabilities. Molecular Oncology. 2012;6(2):111-27. doi: https://doi.org/10.1016/j.molonc.2012.01.011.

2.   De Sousa EMF, Vermeulen L, Fessler E, Medema JP. Cancer heterogeneity--a multifaceted view. EMBO Rep. 2013;14(8):686-95. Epub 2013/07/13. doi: 10.1038/embor.2013.92. PubMed PMID: 23846313; PMCID: PMC3736134.

3.   Hanahan D, Weinberg RA. The Hallmarks of Cancer. Cell. 2000;100(1):57-70. doi: 10.1016/S0092-8674(00)81683-9.

4.   Hanahan D, Weinberg Robert A. Hallmarks of Cancer: The Next Generation. Cell. 2011;144(5):646-74. doi: 10.1016/j.cell.2011.02.013.

5.   Egeblad M, Nakasone ES, Werb Z. Tumors as Organs: Complex Tissues that Interface with the Entire Organism. Developmental Cell. 2010;18(6):884-901. doi: https://doi.org/10.1016/j.devcel.2010.05.012.

6.   Pietras K, Östman A. Hallmarks of cancer: Interactions with the tumor stroma. Experimental Cell Research. 2010;316(8):1324-31. doi: https://doi.org/10.1016/j.yexcr.2010.02.045.

7.   Bhowmick NA, Neilson EG, Moses HL. Stromal fibroblasts in cancer initiation and progression. Nature. 2004;432(7015):332-7. doi: 10.1038/nature03096.

8.   Witsch E, Sela M, Yarden Y. Roles for growth factors in cancer progression. Physiology (Bethesda, Md). 2010;25(2):85-101. Epub 2010/05/01. doi: 10.1152/physiol.00045.2009. PubMed PMID: 20430953; PMCID: PMC3062054.

9.   Amit I, Citri A, Shay T, Lu Y, Katz M, Zhang F, Tarcic G, Siwak D, Lahad J, Jacob-Hirsch J, Amariglio N, Vaisman N, Segal E, Rechavi G, Alon U, Mills GB, Domany E, Yarden Y. A module of negative feedback regulators defines growth factor signaling. Nature Genetics. 2007;39(4):503-12. doi: 10.1038/ng1987.

10.   Sherr CJ, McCormick F. The RB and p53 pathways in cancer. Cancer cell. 2002;2(2):103-12. Epub 2002/09/03. PubMed PMID: 12204530.

11.   Adams JM, Cory S. The Bcl-2 apoptotic switch in cancer development and therapy. Oncogene. 2007;26(9):1324-37. doi: 10.1038/sj.onc.1210220.

12.   Lowe SW, Cepero E, Evan G. Intrinsic tumour suppression. Nature. 2004;432(7015):307-15. Epub 2004/11/19. doi: 10.1038/nature03098. PubMed PMID: 15549092.

13.   Artandi SE, DePinho RA. Telomeres and telomerase in cancer. Carcinogenesis. 2009;31(1):9-18. doi: 10.1093/carcin/bgp268.

14.   Blasco MA. Telomeres and human disease: ageing, cancer and beyond. Nature Reviews Genetics. 2005;6(8):611-22. doi: 10.1038/nrg1656.

15.   Carmeliet P. VEGF as a Key Mediator of Angiogenesis in Cancer. Oncology. 2005;69(suppl 3)(Suppl. 3):4-10. doi: 10.1159/000088478.

16.   Baeriswyl V, Christofori G. The angiogenic switch in carcinogenesis. Seminars in Cancer Biology. 2009;19(5):329-37. doi: https://doi.org/10.1016/j.semcancer.2009.05.003.

17.   Siemann DW. The unique characteristics of tumor vasculature and preclinical evidence for its selective disruption by Tumor-Vascular Disrupting Agents. Cancer

treatment reviews. 2011;37(1):63-74. Epub 06/08. doi: 10.1016/j.ctrv.2010.05.001. PubMed PMID: 20570444.

18.   Fidler IJ. The pathogenesis of cancer metastasis: the 'seed and soil' hypothesis revisited. Nature Reviews Cancer. 2003;3(6):453-8. doi: 10.1038/nrc1098.

19.   Colotta F, Allavena P, Sica A, Garlanda C, Mantovani A. Cancer-related inflammation, the seventh hallmark of cancer: links to genetic instability. Carcinogenesis. 2009;30(7):1073-81. Epub 2009/05/27. doi: 10.1093/carcin/bgp127. PubMed PMID: 19468060.

20.   DeBerardinis RJ, Lum JJ, Hatzivassiliou G, Thompson CB. The biology of cancer: metabolic reprogramming fuels cell growth and proliferation. Cell metabolism. 2008;7(1):11-20. Epub 2008/01/08. doi: 10.1016/j.cmet.2007.10.002. PubMed PMID: 18177721.

21.   Chandra R, Liddle RA. Modulation of pancreatic exocrine and endocrine secretion. Curr Opin Gastroenterol. 2013;29(5):517-22. doi: 10.1097/MOG.0b013e3283639326. PubMed PMID: 23817137.

22.   Becker AE, Hernandez YG, Frucht H, Lucas AL. Pancreatic ductal adenocarcinoma: risk factors, screening, and early detection. World journal of gastroenterology. 2014;20(32):11182-98. doi: 10.3748/wjg.v20.i32.11182. PubMed PMID: 25170203.

23.   Rahib L, Smith BD, Aizenberg R, Rosenzweig AB, Fleshman JM, Matrisian LM. Projecting cancer incidence and deaths to 2030: the unexpected burden of thyroid, liver, and pancreas cancers in the United States. Cancer Res. 2014;74(11):2913-21. Epub 2014/05/21. doi: 10.1158/0008-5472.can-14-0155. PubMed PMID: 24840647.

24.   Max Roser and Hannah Ritchie (2020) - "Cancer" Published online at OurWorldInData.org. Available from: 'https://ourworldindata.org/cancer'.

25.   Siegel RL, Miller KD, Jemal A. Cancer statistics, 2020. CA: A Cancer Journal for Clinicians. 2020;70(1):7-30. doi: 10.3322/caac.21590.

26.   Cicenas J, Kvederaviciute K, Meskinyte I, Meskinyte-Kausiliene E, Skeberdyte A, Cicenas J. KRAS, TP53, CDKN2A, SMAD4, BRCA1, and BRCA2 Mutations in Pancreatic Cancer. Cancers (Basel). 2017;9(5):42. doi: 10.3390/cancers9050042. PubMed PMID: 28452926.

27.   Fokas E, O'Neill E, Gordon-Weeks A, Mukherjee S, McKenna WG, Muschel RJ. Pancreatic ductal adenocarcinoma: From genetics to biology to radiobiology to oncoimmunology and all the way back to the clinic. Biochimica et Biophysica Acta (BBA) - Reviews on Cancer. 2015;1855(1):61-82. doi: https://doi.org/10.1016/j.bbcan.2014.12.001.

28.   Oberstein PE, Olive KP. Pancreatic cancer: why is it so hard to treat? Therapeutic Advances in Gastroenterology. 2013;6(4):321-37. doi: 10.1177/1756283X13478680. PubMed PMID: PMC3667471.

29.   Kota J, Hancock J, Kwon J, Korc M. Pancreatic cancer: Stroma and its current and emerging targeted therapies. Cancer Letters. 2017;391:38-49. doi: https://doi.org/10.1016/j.canlet.2016.12.035.

30.   Adamska A, Domenichini A, Falasca M. Pancreatic Ductal Adenocarcinoma: Current and Evolving Therapies. Int J Mol Sci. 2017;18(7):1338. doi: 10.3390/ijms18071338. PubMed PMID: 28640192.

31.   Yachida S, Iacobuzio-Donahue CA. The Pathology and Genetics of Metastatic Pancreatic Cancer. Archives of Pathology & Laboratory Medicine. 2009;133(3):413-22. doi: 10.1043/1543-2165-133.3.413. PubMed PMID: 19260747.

32.   Ren B, Cui M, Yang G, Wang H, Feng M, You L, Zhao Y. Tumor microenvironment participates in metastasis of pancreatic cancer. Mol Cancer. 2018;17(1):108-. doi: 10.1186/s12943-018-0858-1. PubMed PMID: 30060755.

33.   Swayden M, Iovanna J, Soubeyran P. Pancreatic cancer chemo-resistance is driven by tumor phenotype rather than tumor genotype. Heliyon. 2018;4(12):e01055-e. doi: 10.1016/j.heliyon.2018.e01055. PubMed PMID: 30582059.

34.   Liang C, Shi S, Meng Q, Liang D, Ji S, Zhang B, Qin Y, Xu J, Ni Q, Yu X. Complex roles of the stroma in the intrinsic resistance to gemcitabine in pancreatic cancer: where we are and where we are going. Experimental & Molecular Medicine. 2017;49(12):e406-e. doi: 10.1038/emm.2017.255.

35.   Whatcott CJ, Han H, Von Hoff DD. Orchestrating the Tumor Microenvironment to Improve Survival for Patients With Pancreatic Cancer: Normalization, Not Destruction. Cancer J. 2015;21(4):299-306. doi: 10.1097/PPO.0000000000000140. PubMed PMID: 26222082.

36.   Weledji EP, Enoworock G, Mokake M, Sinju M. How Grim is Pancreatic Cancer? Oncol Rev. 2016;10(1):294-. doi: 10.4081/oncol.2016.294. PubMed PMID: 27471581.

37.   Chiaravalli M, Reni M, O'Reilly EM. Pancreatic ductal adenocarcinoma: State-of-the-art 2017 and new therapeutic strategies. Cancer Treatment Reviews. 2017;60:32-43. doi: https://doi.org/10.1016/j.ctrv.2017.08.007.

38.   Mini E, Nobili S, Caciagli B, Landini I, Mazzei T. Cellular pharmacology of gemcitabine. Annals of Oncology. 2006;17(suppl_5):v7-v12. doi: 10.1093/annonc/mdj941.

39.   Binenbaum Y, Na'ara S, Gil Z. Gemcitabine resistance in pancreatic ductal adenocarcinoma. Drug Resistance Updates. 2015;23:55-68. doi: https://doi.org/10.1016/j.drup.2015.10.002.

40.   Min YJ, Joo KR, Park NH, Yun TK, Nah YW, Nam CW, Park JH. Gemcitabine therapy in patients with advanced pancreatic cancer. Korean J Intern Med. 2002;17(4):259-62. doi: 10.3904/kjim.2002.17.4.259. PubMed PMID: 12647642.

41.   Shipley LA, Brown TJ, Cornpropst JD, Hamilton M, Daniels WD, Culp HW. Metabolism and disposition of gemcitabine, and oncolytic deoxycytidine analog, in mice, rats, and dogs. Drug metabolism and disposition: the biological fate of chemicals. 1992;20(6):849-55. Epub 1992/11/01. PubMed PMID: 1362937.

42.   Koczor CA, Torres RA, Lewis W. The role of transporters in the toxicity of nucleoside and nucleotide analogs. Expert Opin Drug Metab Toxicol. 2012;8(6):665-76. Epub 04/18. doi: 10.1517/17425255.2012.680885. PubMed PMID: 22509856.

43.   Kazuno H, Sakamoto K, Fujioka A, Fukushima M, Matsuda A, Sasaki T. Possible antitumor activity of 1-(3-C-ethynyl-β-d-ribo-pentofuranosyl)cytosine (ECyd, TAS-106) against an established gemcitabine (dFdCyd)-resistant human pancreatic cancer cell line. Cancer Science. 2005;96(5):295-302. doi: 10.1111/j.1349-7006.2005.00046.x.

44.   Nakahira S, Nakamori S, Tsujie M, Takahashi Y, Okami J, Yoshioka S, Yamasaki M, Marubashi S, Takemasa I, Miyamoto A, Takeda Y, Nagano H, Dono K, Umeshita K, Sakon M, Monden M. Involvement of ribonucleotide reductase M1 subunit

overexpression in gemcitabine resistance of human pancreatic cancer. International Journal of Cancer. 2007;120(6):1355-63. doi: 10.1002/ijc.22390.

45.   Amrutkar M, Gladhaug IP. Pancreatic Cancer Chemoresistance to Gemcitabine. Cancers (Basel). 2017;9(11):157. doi: 10.3390/cancers9110157. PubMed PMID: 29144412.

46.   Manji GA, Olive KP, Saenger YM, Oberstein P. Current and Emerging Therapies in Metastatic Pancreatic Cancer. Clinical Cancer Research. 2017;23(7):1670-8. doi: 10.1158/1078-0432.ccr-16-2319.

47.   Von Hoff DD, Ervin T, Arena FP, Chiorean EG, Infante J, Moore M, Seay T, Tjulandin SA, Ma WW, Saleh MN, Harris M, Reni M, Dowden S, Laheru D, Bahary N, Ramanathan RK, Tabernero J, Hidalgo M, Goldstein D, Van Cutsem E, Wei X, Iglesias J, Renschler MF. Increased survival in pancreatic cancer with nab-paclitaxel plus gemcitabine. The New England journal of medicine. 2013;369(18):1691-703. Epub 2013/10/18. doi: 10.1056/NEJMoa1304369. PubMed PMID: 24131140; PMCID: PMC4631139.

48.   Rajeshkumar NV, Yabuuchi S, Pai SG, Tong Z, Hou S, Bateman S, Pierce DW, Heise C, Von Hoff DD, Maitra A, Hidalgo M. Superior therapeutic efficacy of nab-paclitaxel over cremophor-based paclitaxel in locally advanced and metastatic models of human pancreatic cancer. British Journal of Cancer. 2016;115(4):442-53. doi: 10.1038/bjc.2016.215.

49.   Conroy T, Desseigne F, Ychou M, Bouché O, Guimbaud R, Bécouarn Y, Adenis A, Raoul J-L, Gourgou-Bourgade S, de la Fouchardière C, Bennouna J, Bachet J-B, Khemissa-Akouz F, Péré-Vergé D, Delbaldo C, Assenat E, Chauffert B, Michel P, Montoto-Grillot C, Ducreux M. FOLFIRINOX versus Gemcitabine for Metastatic Pancreatic Cancer. New England Journal of Medicine. 2011;364(19):1817-25. doi: 10.1056/NEJMoa1011923. PubMed PMID: 21561347.

50.   Stein SM, James ES, Deng Y, Cong X, Kortmansky JS, Li J, Staugaard C, Indukala D, Boustani AM, Patel V, Cha CH, Salem RR, Chang B, Hochster HS, Lacy J. Final analysis of a phase II study of modified FOLFIRINOX in locally advanced and metastatic pancreatic cancer. British Journal of Cancer. 2016;114(7):737-43. doi: 10.1038/bjc.2016.45.

51.   Wang-Gillam A, Li CP, Bodoky G, Dean A, Shan YS, Jameson G, Macarulla T, Lee KH, Cunningham D, Blanc JF, Hubner RA, Chiu CF, Schwartsmann G, Siveke JT, Braiteh F, Moyo V, Belanger B, Dhindsa N, Bayever E, Von Hoff DD, Chen LT. Nanoliposomal irinotecan with fluorouracil and folinic acid in metastatic pancreatic cancer after previous gemcitabine-based therapy (NAPOLI-1): a global, randomised, open-label, phase 3 trial. Lancet (London, England). 2016;387(10018):545-57. Epub 2015/11/30. doi: 10.1016/s0140-6736(15)00986-1. PubMed PMID: 26615328.

52.   ASLAN M, SHAHBAZI R, ULUBAYRAM K, OZPOLAT B. Targeted Therapies for Pancreatic Cancer and Hurdles Ahead. Anticancer research. 2018;38(12):6591-606. doi: 10.21873/anticanres.13026.

53.   Moore MJ, Goldstein D, Hamm J, Figer A, Hecht JR, Gallinger S, Au HJ, Murawa P, Walde D, Wolff RA, Campos D, Lim R, Ding K, Clark G, Voskoglou-Nomikos T, Ptasynski M, Parulekar W. Erlotinib Plus Gemcitabine Compared With Gemcitabine Alone in Patients With Advanced Pancreatic Cancer: A Phase III Trial of the National Cancer Institute of Canada Clinical Trials Group. Journal of Clinical

Oncology. 2007;25(15):1960-6. doi: 10.1200/jco.2006.07.9525. PubMed PMID: 17452677.

54.   Jameson GS, Borazanci E, Babiker HM, Poplin E, Niewiarowska AA, Gordon MS, Barrett MT, Rosenthal A, Stoll-D'Astice A, Crowley J, Shemanski L, Korn RL, Ansaldo K, Lebron L, Ramanathan RK, Von Hoff DD. Response Rate Following Albumin-Bound Paclitaxel Plus Gemcitabine Plus Cisplatin Treatment Among Patients With Advanced Pancreatic Cancer: A Phase 1b/2 Pilot Clinical Trial. JAMA oncology. 2019. Epub 2019/10/04. doi: 10.1001/jamaoncol.2019.3394. PubMed PMID: 31580386; PMCID: PMC6777241.

55.   Reni M, Zanon S, Balzano G, Passoni P, Pircher C, Chiaravalli M, Fugazza C, Ceraulo D, Nicoletti R, Arcidiacono PG, Macchini M, Peretti U, Castoldi R, Doglioni C, Falconi M, Partelli S, Gianni L. A randomised phase 2 trial of nab-paclitaxel plus gemcitabine with or without capecitabine and cisplatin in locally advanced or borderline resectable pancreatic adenocarcinoma. European journal of cancer (Oxford, England : 1990). 2018;102:95-102. Epub 2018/08/28. doi: 10.1016/j.ejca.2018.07.007. PubMed PMID: 30149366.

56.   Jones S, Zhang X, Parsons DW, Lin JC-H, Leary RJ, Angenendt P, Mankoo P, Carter H, Kamiyama H, Jimeno A, Hong S-M, Fu B, Lin M-T, Calhoun ES, Kamiyama M, Walter K, Nikolskaya T, Nikolsky Y, Hartigan J, Smith DR, Hidalgo M, Leach SD, Klein AP, Jaffee EM, Goggins M, Maitra A, Iacobuzio-Donahue C, Eshleman JR, Kern SE, Hruban RH, Karchin R, Papadopoulos N, Parmigiani G, Vogelstein B, Velculescu VE, Kinzler KW. Core Signaling Pathways in Human Pancreatic Cancers Revealed by Global Genomic Analyses. Science. 2008;321(5897):1801-6. doi: 10.1126/science.1164368.

57.   Hruban RH, Goggins M, Parsons J, Kern SE. Progression Model for Pancreatic Cancer. Clinical Cancer Research. 2000;6(8):2969-72.

58.   Zhang Y, Yang C, Cheng H, Fan Z, Huang Q, Lu Y, Fan K, Luo G, Jin K, Wang Z, Liu C, Yu X. Novel agents for pancreatic ductal adenocarcinoma: emerging therapeutics and future directions. J Hematol Oncol. 2018;11(1):14-. doi: 10.1186/s13045-017-0551-7. PubMed PMID: 29386069.

59.   Kaufman B, Shapira-Frommer R, Schmutzler RK, Audeh MW, Friedlander M, Balmana J, Mitchell G, Fried G, Stemmer SM, Hubert A, Rosengarten O, Steiner M, Loman N, Bowen K, Fielding A, Domchek SM. Olaparib monotherapy in patients with advanced cancer and a germline BRCA1/2 mutation. Journal of clinical oncology : official journal of the American Society of Clinical Oncology. 2015;33(3):244-50. Epub 2014/11/05. doi: 10.1200/jco.2014.56.2728. PubMed PMID: 25366685; PMCID: PMC6057749.

60.   Chini CC, Guerrico AM, Nin V, Camacho-Pereira J, Escande C, Barbosa MT, Chini EN. Targeting of NAD metabolism in pancreatic cancer cells: potential novel therapy for pancreatic tumors. Clinical cancer research : an official journal of the American Association for Cancer Research. 2014;20(1):120-30. Epub 2013/09/13. doi: 10.1158/1078-0432.ccr-13-0150. PubMed PMID: 24025713; PMCID: PMC3947324.

61.   Sato N, Cheng X-B, Kohi S, Koga A, Hirata K. Targeting hyaluronan for the treatment of pancreatic ductal adenocarcinoma. Acta Pharm Sin B. 2016;6(2):101-5. Epub 01/21. doi: 10.1016/j.apsb.2016.01.002. PubMed PMID: 27006892.

62.   Vennin C, Murphy KJ, Morton JP, Cox TR, Pajic M, Timpson P. Reshaping the Tumor Stroma for Treatment of Pancreatic Cancer. Gastroenterology. 2018;154(4):820-38. doi: 10.1053/j.gastro.2017.11.280.

63.   Sherman MH, Yu RT, Engle DD, Ding N, Atkins AR, Tiriac H, Collisson EA, Connor F, Van Dyke T, Kozlov S, Martin P, Tseng TW, Dawson DW, Donahue TR, Masamune A, Shimosegawa T, Apte MV, Wilson JS, Ng B, Lau SL, Gunton JE, Wahl GM, Hunter T, Drebin JA, O'Dwyer PJ, Liddle C, Tuveson DA, Downes M, Evans RM. Vitamin D receptor-mediated stromal reprogramming suppresses pancreatitis and enhances pancreatic cancer therapy. Cell. 2014;159(1):80-93. Epub 2014/09/27. doi: 10.1016/j.cell.2014.08.007. PubMed PMID: 25259922; PMCID: PMC4177038.

64.   Zhang Y-F, Jiang S-H, Hu L-P, Huang P-Q, Wang X, Li J, Zhang X-L, Nie H-Z, Zhang Z-G. Targeting the tumor microenvironment for pancreatic ductal adenocarcinoma therapy. Chinese Clinical Oncology. 2019;8(2).

65.   Tsai KK, Chan T-S, Shaked Y. Next Viable Routes to Targeting Pancreatic Cancer Stemness: Learning from Clinical Setbacks. J Clin Med. 2019;8(5):702. doi: 10.3390/jcm8050702. PubMed PMID: 31108941.

66.   Hilmi M, Bartholin L, Neuzillet C. Immune therapies in pancreatic ductal adenocarcinoma: Where are we now? World journal of gastroenterology. 2018;24(20):2137-51. doi: 10.3748/wjg.v24.i20.2137. PubMed PMID: 29853732.

67.   Vieira DB, Gamarra LF. Advances in the use of nanocarriers for cancer diagnosis and treatment. Einstein. 2016;14(1):99-103. doi: 10.1590/S1679-45082016RB3475. PubMed PMID: PMC4872924.

68.   Zhu L, Staley C, Kooby D, El-Rays B, Mao H, Yang L. Current status of biomarker and targeted nanoparticle development: The precision oncology approach for pancreatic cancer therapy. Cancer Lett. 2017;388:139-48. Epub 2016/12/06. doi: 10.1016/j.canlet.2016.11.030. PubMed PMID: 27916607; PMCID: Pmc5318282.

69.   Sailor MJ, Park JH. Hybrid nanoparticles for detection and treatment of cancer. Advanced materials (Deerfield Beach, Fla). 2012;24(28):3779-802. Epub 2012/05/23. doi: 10.1002/adma.201200653. PubMed PMID: 22610698; PMCID: PMC3517011.

70.   Conde J, Tian F, Baptista PV, de la Fuente JM. Multifunctional Gold Nanocarriers for Cancer Theranostics: From Bench to Bedside and Back Again? In: Alonso MJ, Garcia-Fuentes M, editors. Nano-Oncologicals: New Targeting and Delivery Approaches. Cham: Springer International Publishing; 2014. p. 295-328.

71.   Hsueh CT, Selim JH, Tsai JY, Hsueh CT. Nanovectors for anti-cancer drug delivery in the treatment of advanced pancreatic adenocarcinoma. World journal of gastroenterology. 2016;22(31):7080-90. Epub 2016/09/10. doi: 10.3748/wjg.v22.i31.7080. PubMed PMID: 27610018; PMCID: Pmc4988316.

72.   Au M, Emeto TI, Power J, Vangaveti VN, Lai HC. Emerging Therapeutic Potential of Nanoparticles in Pancreatic Cancer: A Systematic Review of Clinical Trials. Biomedicines. 2016;4(3):20. doi: 10.3390/biomedicines4030020. PubMed PMID: 28536387.

73.   Hu CM, Zhang L. Nanoparticle-based combination therapy toward overcoming drug resistance in cancer. Biochemical pharmacology. 2012;83(8):1104-11. Epub 2012/01/31. doi: 10.1016/j.bcp.2012.01.008. PubMed PMID: 22285912.

74.   Parhi P, Mohanty C, Sahoo SK. Nanotechnology-based combinational drug delivery: an emerging approach for cancer therapy. Drug discovery today. 2012;17(17-

18):1044-52. Epub 2012/06/02. doi: 10.1016/j.drudis.2012.05.010. PubMed PMID: 22652342.

75.   Ruoslahti E, Bhatia SN, Sailor MJ. Targeting of drugs and nanoparticles to tumors. The Journal of cell biology. 2010;188(6):759-68. Epub 2010/03/17. doi: 10.1083/jcb.200910104. PubMed PMID: 20231381; PMCID: PMC2845077.

76.   Rosenblum D, Joshi N, Tao W, Karp JM, Peer D. Progress and challenges towards targeted delivery of cancer therapeutics. Nature communications. 2018;9(1):1410-. doi: 10.1038/s41467-018-03705-y. PubMed PMID: 29650952.

77.   Zhou H, Qian W, Uckun FM, Wang L, Wang YA, Chen H, Kooby D, Yu Q, Lipowska M, Staley CA, Mao H, Yang L. IGF1 Receptor Targeted Theranostic Nanoparticles for Targeted and Image-Guided Therapy of Pancreatic Cancer. ACS Nano. 2015;9(8):7976-91. doi: 10.1021/acsnano.5b01288.

78.   Yang L, Sajja HK, Cao Z, Qian W, Bender L, Marcus AI, Lipowska M, Wood WC, Wang YA. uPAR-targeted optical imaging contrasts as theranostic agents for tumor margin detection. Theranostics. 2013;4(1):106-18. Epub 2014/01/08. doi: 10.7150/thno.7409. PubMed PMID: 24396518; PMCID: Pmc3881230.

79.   McCarroll J, Teo J, Boyer C, Goldstein D, Kavallaris M, Phillips P. Potential applications of nanotechnology for the diagnosis and treatment of pancreatic cancer. Frontiers in physiology. 2014;5(2). doi: 10.3389/fphys.2014.00002.

80.   Licciardi M, Paolino D, Celia C, Giammona G, Cavallaro G, Fresta M. Folate-targeted supramolecular vesicular aggregates based on polyaspartyl-hydrazide copolymers for the selective delivery of antitumoral drugs. Biomaterials. 2010;31(28):7340-54. doi: https://doi.org/10.1016/j.biomaterials.2010.05.060.

81.   Arya G, Vandana M, Acharya S, Sahoo SK. Enhanced antiproliferative activity of Herceptin (HER2)-conjugated gemcitabine-loaded chitosan nanoparticle in pancreatic cancer therapy. Nanomedicine : nanotechnology, biology, and medicine. 2011;7(6):859-70. Epub 2011/05/10. doi: 10.1016/j.nano.2011.03.009. PubMed PMID: 21550422.

82.   Bhaw-Luximon A, Jhurry D. New avenues for improving pancreatic ductal adenocarcinoma (PDAC) treatment: Selective stroma depletion combined with nano drug delivery. Cancer Lett. 2015;369(2):266-73. Epub 2015/09/30. doi: 10.1016/j.canlet.2015.09.007. PubMed PMID: 26415628.

83.   Huang HC, Mallidi S, Liu J, Chiang CT, Mai Z, Goldschmidt R, Ebrahim-Zadeh N, Rizvi I, Hasan T. Photodynamic Therapy Synergizes with Irinotecan to Overcome Compensatory Mechanisms and Improve Treatment Outcomes in Pancreatic Cancer. Cancer research. 2016;76(5):1066-77. Epub 2016/01/01. doi: 10.1158/0008-5472.can-15-0391. PubMed PMID: 26719532; PMCID: Pmc4775276.

84.   Cosco D, Bulotta A, Ventura M, Celia C, Calimeri T, Perri G, Paolino D, Costa N, Neri P, Tagliaferri P, Tassone P, Fresta M. In vivo activity of gemcitabine-loaded PEGylated small unilamellar liposomes against pancreatic cancer. Cancer Chemotherapy and Pharmacology. 2009;64(5):1009-20. doi: 10.1007/s00280-009-0957-1.

85.   Wonganan P, Lansakara PD, Zhu S, Holzer M, Sandoval MA, Warthaka M, Cui Z. Just getting into cells is not enough: mechanisms underlying 4-(N)-stearoyl gemcitabine solid lipid nanoparticle's ability to overcome gemcitabine resistance caused by RRM1 overexpression. J Control Release. 2013;169(1-2):17-27. Epub 2013/04/11. doi: 10.1016/j.jconrel.2013.03.033. PubMed PMID: 23570983; PMCID: PMC3683387.

86.   Zhu S, Wonganan P, Lansakara PD, O'Mary HL, Li Y, Cui Z. The effect of the acid-sensitivity of 4-(N)-stearoyl gemcitabine-loaded micelles on drug resistance caused by RRM1 overexpression. Biomaterials. 2013;34(9):2327-39. Epub 2012/12/25. doi: 10.1016/j.biomaterials.2012.11.053. PubMed PMID: 23261218; PMCID: PMC3552003.

87.   Desmaele D, Gref R, Couvreur P. Squalenoylation: a generic platform for nanoparticular drug delivery. J Control Release. 2012;161(2):609-18. Epub 2011/08/16. doi: 10.1016/j.jconrel.2011.07.038. PubMed PMID: 21840355.

88.   Réjiba S, Reddy LH, Bigand C, Parmentier C, Couvreur P, Hajri A. Squalenoyl gemcitabine nanomedicine overcomes the low efficacy of gemcitabine therapy in pancreatic cancer. Nanomedicine: Nanotechnology, Biology and Medicine. 2011;7(6):841-9. doi: https://doi.org/10.1016/j.nano.2011.02.012.

89.   Chitkara D, Mittal A, Behrman SW, Kumar N, Mahato RI. Self-Assembling, Amphiphilic Polymer–Gemcitabine Conjugate Shows Enhanced Antitumor Efficacy Against Human Pancreatic Adenocarcinoma. Bioconjugate Chemistry. 2013;24(7):1161-73. doi: 10.1021/bc400032x.

90.   Kattel K, Mondal G, Lin F, Kumar V, Mahato RI. Biodistribution of Self-Assembling Polymer–Gemcitabine Conjugate after Systemic Administration into Orthotopic Pancreatic Tumor Bearing Mice. Molecular Pharmaceutics. 2017;14(5):1365-72. doi: 10.1021/acs.molpharmaceut.6b00929.

91.   Poon C, He C, Liu D, Lu K, Lin W. Self-assembled nanoscale coordination polymers carrying oxaliplatin and gemcitabine for synergistic combination therapy of pancreatic cancer. J Control Release. 2015;201:90-9. Epub 01/22. doi: 10.1016/j.jconrel.2015.01.026. PubMed PMID: 25620067.

92.   Emamzadeh M, Emamzadeh M, Pasparakis G. Dual Controlled Delivery of Gemcitabine and Cisplatin Using Polymer-Modified Thermosensitive Liposomes for Pancreatic Cancer. ACS Applied Bio Materials. 2019;2(3):1298-309. doi: 10.1021/acsabm.9b00007.

93.   van der Meel R. Targeted inhibition of tumor growth and angiogenesis 2013.

94.   Oliveira-Cunha M, Newman WG, Siriwardena AK. Epidermal growth factor receptor in pancreatic cancer. Cancers (Basel). 2011;3(2):1513-26. doi: 10.3390/cancers3021513. PubMed PMID: 24212772.

95.   Mondal G, Kumar V, Shukla SK, Singh PK, Mahato RI. EGFR-Targeted Polymeric Mixed Micelles Carrying Gemcitabine for Treating Pancreatic Cancer. Biomacromolecules. 2016;17(1):301-13. doi: 10.1021/acs.biomac.5b01419.

96.   McDaid W, Greene M, Johnston M, Pollheimer E, Smyth P, McLaughlin K, Van Schaeybroeck S, Straubinger R, Longley D, Scott C. Repurposing of Cetuximab in antibody-directed chemotherapy-loaded nanoparticles in EGFR therapy-resistant pancreatic tumours. Nanoscale. 2019;11. doi: 10.1039/C9NR07257H.

97.   Patra CR, Bhattacharya R, Wang E, Katarya A, Lau JS, Dutta S, Muders M, Wang S, Buhrow SA, Safgren SL, Yaszemski MJ, Reid JM, Ames MM, Mukherjee P, Mukhopadhyay D. Targeted Delivery of Gemcitabine to Pancreatic Adenocarcinoma Using Cetuximab as a Targeting Agent. Cancer Research. 2008;68(6):1970-8. doi: 10.1158/0008-5472.can-07-6102.

98.   Mondal G, Almawash S, Chaudhary AK, Mahato RI. EGFR-Targeted Cationic Polymeric Mixed Micelles for Codelivery of Gemcitabine and miR-205 for Treating

Advanced Pancreatic Cancer. Molecular Pharmaceutics. 2017;14(9):3121-33. doi: 10.1021/acs.molpharmaceut.7b00355.

99.   Lee GY, Qian WP, Wang L, Wang YA, Staley CA, Satpathy M, Nie S, Mao H, Yang L. Theranostic Nanoparticles with Controlled Release of Gemcitabine for Targeted Therapy and MRI of Pancreatic Cancer. ACS Nano. 2013;7(3):2078-89. doi: 10.1021/nn3043463.

100.   Zinger A, Koren L, Adir O, Poley M, Alyan M, Yaari Z, Noor N, Krinsky N, Simon A, Gibori H, Krayem M, Mumblat Y, Kasten S, Ofir S, Fridman E, Milman N, Lubtow MM, Liba L, Shklover J, Shainsky-Roitman J, Binenbaum Y, Hershkovitz D, Gil Z, Dvir T, Luxenhofer R, Satchi-Fainaro R, Schroeder A. Collagenase Nanoparticles Enhance the Penetration of Drugs into Pancreatic Tumors. ACS Nano. 2019. Epub 2019/09/11. doi: 10.1021/acsnano.9b02395. PubMed PMID: 31503443.

101.   Miao L, Liu Q, Lin CM, Luo C, Wang Y, Liu L, Yin W, Hu S, Kim WY, Huang L. Targeting Tumor-Associated Fibroblasts for Therapeutic Delivery in Desmoplastic Tumors. Cancer research. 2017;77(3):719-31. Epub 11/18. doi: 10.1158/0008-5472.CAN-16-0866. PubMed PMID: 27864344.

102.   Mardhian DF, Storm G, Bansal R, Prakash J. Nano-targeted relaxin impairs fibrosis and tumor growth in pancreatic cancer and improves the efficacy of gemcitabine in vivo. Journal of Controlled Release. 2018;290:1-10. doi: https://doi.org/10.1016/j.jconrel.2018.09.031.

103.   Hu M, Wang Y, Xu L, An S, Tang Y, Zhou X, Li J, Liu R, Huang L. Relaxin gene delivery mitigates liver metastasis and synergizes with check point therapy. Nature communications. 2019;10(1):2993. doi: 10.1038/s41467-019-10893-8.

104.   Vallet-Regi M, Colilla M, Izquierdo-Barba I, Manzano M. Mesoporous Silica Nanoparticles for Drug Delivery: Current Insights. Molecules (Basel, Switzerland). 2017;23(1). Epub 2018/01/04. doi: 10.3390/molecules23010047. PubMed PMID: 29295564; PMCID: PMC5943960.

105.   Vivero-Escoto JL, Slowing II, Trewyn BG, Lin VSY. Mesoporous Silica Nanoparticles for Intracellular Controlled Drug Delivery. Small. 2010;6(18):1952-67. doi: 10.1002/smll.200901789.

106.   Coti KK, Belowich ME, Liong M, Ambrogio MW, Lau YA, Khatib HA, Zink JI, Khashab NM, Stoddart JF. Mechanised nanoparticles for drug delivery. Nanoscale 2009;1(1):16-39. PubMed PMID: AN 2009:1406867.

107.   Cheon J, Lee J-H. Synergistically Integrated Nanoparticles as Multimodal Probes for Nanobiotechnology. Acc Chem Res 2008;41(12):1630-40. PubMed PMID: AN 2008:982777.

108.   Wani A, Savithra GHL, Abyad A, Kanvinde S, Li J, Brock S, Oupicky D. Surface PEGylation of Mesoporous Silica Nanorods (MSNR): Effect on loading, release, and delivery of mitoxantrone in hypoxic cancer cells. Scientific reports. 2017;7(1):2274. Epub 2017/05/26. doi: 10.1038/s41598-017-02531-4. PubMed PMID: 28536462; PMCID: PMC5442097.

109.   Rosenholm JM, Mamaeva V, Sahlgren C, Linden M. Nanoparticles in targeted cancer therapy: mesoporous silica nanoparticles entering preclinical development stage. Nanomedicine (London, England). 2012;7(1):111-20. Epub 2011/12/24. doi: 10.2217/nnm.11.166. PubMed PMID: 22191780.

110.   Pasqua L, Leggio A, Sisci D, Ando S, Morelli C. Mesoporous Silica Nanoparticles in Cancer Therapy: Relevance of the Targeting Function. Mini reviews in medicinal chemistry. 2016;16(9):743-53. Epub 2016/03/22. doi: 10.2174/1389557516666160321113620. PubMed PMID: 26996622.

111.   Zhou Y, Quan G, Wu Q, Zhang X, Niu B, Wu B, Huang Y, Pan X, Wu C. Mesoporous silica nanoparticles for drug and gene delivery. Acta Pharm Sin B. 2018;8(2):165-77. Epub 02/12. doi: 10.1016/j.apsb.2018.01.007. PubMed PMID: 29719777.

112.   Narayan R, Nayak UY, Raichur AM, Garg S. Mesoporous Silica Nanoparticles: A Comprehensive Review on Synthesis and Recent Advances. Pharmaceutics. 2018;10(3):118. doi: 10.3390/pharmaceutics10030118. PubMed PMID: 30082647.

113.   Phillips E, Penate-Medina O, Zanzonico PB, Carvajal RD, Mohan P, Ye Y, Humm J, Gönen M, Kalaigian H, Schöder H, Strauss HW, Larson SM, Wiesner U, Bradbury MS. Clinical translation of an ultrasmall inorganic optical-PET imaging nanoparticle probe. Sci Transl Med. 2014;6(260):260ra149-260ra149. Epub 10/29. doi: 10.1126/scitranslmed.3009524. PubMed PMID: 25355699.

114.   Song Y, Li Y, Xu Q, Liu Z. Mesoporous silica nanoparticles for stimuli-responsive controlled drug delivery: advances, challenges, and outlook. International journal of nanomedicine. 2017;12:87-110. Epub 2017/01/06. doi: 10.2147/ijn.s117495. PubMed PMID: 28053526; PMCID: PMC5191581.

115.   Colilla M, González B, Vallet-Regí M. Mesoporous silica nanoparticles for the design of smart delivery nanodevices. Biomaterials Science. 2013;1(2):114-34. doi: 10.1039/C2BM00085G.

116.   Wu S-H, Mou C-Y, Lin H-P. Synthesis of mesoporous silica nanoparticles. Chemical Society Reviews. 2013;42(9):3862-75. doi: 10.1039/C3CS35405A.

117.   Yang P, Gai S, Lin J. Functionalized mesoporous silica materials for controlled drug delivery. Chemical Society Reviews. 2012;41(9):3679-98. doi: 10.1039/C2CS15308D.

118.   Trewyn BG, Slowing II, Giri S, Chen H-T, Lin VSY. Synthesis and Functionalization of a Mesoporous Silica Nanoparticle Based on the Sol–Gel Process and Applications in Controlled Release. Accounts of Chemical Research. 2007;40(9):846-53. doi: 10.1021/ar600032u.

119.   Kuthati Y, Sung P-J, Weng C, Mou C-Y, Lee C-H. Functionalization of Mesoporous Silica Nanoparticles for Targeting, Biocompatibility, Combined Cancer Therapies and Theragnosis. Journal of nanoscience and nanotechnology. 2013;13:2399-430. doi: 10.1166/jnn.2013.7363.

120.   Liu X, Situ A, Kang Y, Villabroza KR, Liao Y, Chang CH, Donahue T, Nel AE, Meng H. Irinotecan Delivery by Lipid-Coated Mesoporous Silica Nanoparticles Shows Improved Efficacy and Safety over Liposomes for Pancreatic Cancer. ACS Nano. 2016;10(2):2702-15. doi: 10.1021/acsnano.5b07781.

121.   Malfanti A, Miletto I, Bottinelli E, Zonari D, Blandino G, Berlier G, Arpicco S. Delivery of Gemcitabine Prodrugs Employing Mesoporous Silica Nanoparticles. Molecules (Basel, Switzerland). 2016;21(4):522. Epub 2016/04/26. doi: 10.3390/molecules21040522. PubMed PMID: 27110750.

122.   Fu Q, Hargrove D, Lu X. Improving paclitaxel pharmacokinetics by using tumor-specific mesoporous silica nanoparticles with intraperitoneal delivery. Nanomedicine :

nanotechnology, biology, and medicine. 2016;12(7):1951-9. Epub 2016/05/08. doi: 10.1016/j.nano.2016.04.013. PubMed PMID: 27151564; PMCID: Pmc5115211.

123.   Meng H, Zhao Y, Dong J, Xue M, Lin Y-S, Ji Z, Mai WX, Zhang H, Chang CH, Brinker CJ, Zink JI, Nel AE. Two-Wave Nanotherapy to Target the Stroma and Optimize Gemcitabine Delivery to a Human Pancreatic Cancer Model in Mice. ACS nano. 2013;7(11):10.1021/nn404083m. doi: 10.1021/nn404083m. PubMed PMID: PMC3878438.

124.   Meng H, Wang M, Liu H, Liu X, Situ A, Wu B, Ji Z, Chang CH, Nel AE. Use of a Lipid-Coated Mesoporous Silica Nanoparticle Platform for Synergistic Gemcitabine and Paclitaxel Delivery to Human Pancreatic Cancer in Mice. ACS Nano. 2015;9(4):3540-57. doi: 10.1021/acsnano.5b00510.

125.   Er Ö, Colak SG, Ocakoglu K, Ince M, Bresolí-Obach R, Mora M, Sagristá ML, Yurt F, Nonell S. Selective Photokilling of Human Pancreatic Cancer Cells Using Cetuximab-Targeted Mesoporous Silica Nanoparticles for Delivery of Zinc Phthalocyanine. Molecules (Basel, Switzerland). 2018;23(11):2749. doi: 10.3390/molecules23112749. PubMed PMID: 30355983.

126.   Xing L, Li X, Xing Z, Li F, Shen M, Wang H, Shi X, Du L. Silica/gold nanoplatform combined with a thermosensitive gel for imaging-guided interventional therapy in PDX of pancreatic cancer. Chemical Engineering Journal. 2020;382:122949. doi: https://doi.org/10.1016/j.cej.2019.122949.

127.   McNally LR, Mezera M, Morgan DE, Frederick PJ, Yang ES, Eltoum IE, Grizzle WE. Current and Emerging Clinical Applications of Multispectral Optoacoustic Tomography (MSOT) in Oncology. Clinical cancer research : an official journal of the American Association for Cancer Research. 2016;22(14):3432-9. Epub 2016/05/22. doi: 10.1158/1078-0432.ccr-16-0573. PubMed PMID: 27208064; PMCID: Pmc5046137.

128.   Zeiderman MR, Morgan DE, Christein JD, Grizzle WE, McMasters KM, McNally LR. Acidic pH-targeted chitosan capped mesoporous silica coated gold nanorods facilitate detection of pancreatic tumors via multispectral optoacoustic tomography. ACS biomaterials science & engineering. 2016;2(7):1108-20. Epub 2017/06/20. doi: 10.1021/acsbiomaterials.6b00111. PubMed PMID: 28626793; PMCID: Pmc5470628.

129.   Woo W, Carey ET, Choi M. Spotlight on liposomal irinotecan for metastatic pancreatic cancer: patient selection and perspectives. Onco Targets Ther. 2019;12:1455-63. doi: 10.2147/OTT.S167590. PubMed PMID: 30863113.

130.   Sun J, Kim D-H, Guo Y, Teng Z, Li Y, Zheng L, Zhang Z, Larson AC, Lu G. A c(RGDfE) conjugated multi-functional nanomedicine delivery system for targeted pancreatic cancer therapy. Journal of Materials Chemistry B. 2015;3(6):1049-58. doi: 10.1039/C4TB01402B.

131.   Meng H, Wang M, Liu H, Liu X, Situ A, Wu B, Ji Z, Chang CH, Nel AE. Correction to Use of a Lipid-Coated Mesoporous Silica Nanoparticle Platform for Synergistic Gemcitabine and Paclitaxel Delivery to Human Pancreatic Cancer in Mice. ACS Nano. 2016;10(6):6416-. doi: 10.1021/acsnano.6b03110.

132.   Meng H, Zhao Y, Dong J, Xue M, Lin Y-S, Ji Z, Mai WX, Zhang H, Chang CH, Brinker CJ, Zink JI, Nel AE. Two-wave nanotherapy to target the stroma and optimize gemcitabine delivery to a human pancreatic cancer model in mice. ACS nano. 2013;7(11):10048-65. Epub 10/28. doi: 10.1021/nn404083m. PubMed PMID: 24143858.

133.   Krempley BD, Yu KH. Preclinical models of pancreatic ductal adenocarcinoma. Chinese Clinical Oncology. 2017;6(3):3.
134.   Talmadge JE, Singh RK, Fidler IJ, Raz A. Murine Models to Evaluate Novel and Conventional Therapeutic Strategies for Cancer. The American Journal of Pathology. 2007;170(3):793-804. doi: 10.2353/ajpath.2007.060929. PubMed PMID: PMC1864878.
135.   Voskoglou-Nomikos T, Pater JL, Seymour L. Clinical predictive value of the in vitro cell line, human xenograft, and mouse allograft preclinical cancer models. Clinical cancer research : an official journal of the American Association for Cancer Research. 2003;9(11):4227-39. Epub 2003/10/02. PubMed PMID: 14519650.
136.   Mohammed A, Janakiram NB, Lightfoot S, Gali H, Vibhudutta A, Rao CV. Early detection and prevention of pancreatic cancer: use of genetically engineered mouse models and advanced imaging technologies. Current medicinal chemistry. 2012;19(22):3701-13. Epub 2012/06/12. doi: 10.2174/092986712801661095. PubMed PMID: 22680929.
137.   Labrijn AF, Meesters JI, Bunce M, Armstrong AA, Somani S, Nesspor TC, Chiu ML, Altintas I, Verploegen S, Schuurman J, Parren P. Efficient Generation of Bispecific Murine Antibodies for Pre-Clinical Investigations in Syngeneic Rodent Models. Scientific reports. 2017;7(1):2476. Epub 2017/06/01. doi: 10.1038/s41598-017-02823-9. PubMed PMID: 28559564; PMCID: PMC5449386.
138.   Krempley BD, Yu KH. Preclinical models of pancreatic ductal adenocarcinoma. Chinese clinical oncology. 2017;6(3):25. Epub 2017/07/15. doi: 10.21037/cco.2017.06.15. PubMed PMID: 28705002.
139.   Hruban RH, Maitra A, Goggins M. Update on Pancreatic Intraepithelial Neoplasia. International Journal of Clinical and Experimental Pathology. 2008;1(4):306-16. PubMed PMID: PMC2480542.
140.   Besmer DM, Curry JM, Roy LD, Tinder TL, Sahraei M, Schettini J, Hwang SI, Lee YY, Gendler SJ, Mukherjee P. Pancreatic ductal adenocarcinoma mice lacking mucin 1 have a profound defect in tumor growth and metastasis. Cancer Res. 2011;71(13):4432-42. Epub 2011/05/12. doi: 10.1158/0008-5472.can-10-4439. PubMed PMID: 21558393; PMCID: PMC3129481.
141.   Wang P, Yoo B, Sherman S, Mukherjee P, Ross A, Pantazopoulos P, Petkova V, Farrar C, Medarova Z, Moore A. Predictive imaging of chemotherapeutic response in a transgenic mouse model of pancreatic cancer. International journal of cancer. 2016;139(3):712-8. Epub 2016/03/22. doi: 10.1002/ijc.30098. PubMed PMID: 26996122; PMCID: Pmc4925171.
142.   Mukherjee P, Basu GD, Tinder TL, Subramani DB, Bradley JM, Arefayene M, Skaar T, De Petris G. Progression of pancreatic adenocarcinoma is significantly impeded with a combination of vaccine and COX-2 inhibition. Journal of immunology (Baltimore, Md : 1950). 2009;182(1):216-24. Epub 2008/12/26. PubMed PMID: 19109152; PMCID: Pmc3838792.
143.   Tinder TL, Subramani DB, Basu GD, Bradley JM, Schettini J, Million A, Skaar T, Mukherjee P. MUC1 enhances tumor progression and contributes toward immunosuppression in a mouse model of spontaneous pancreatic adenocarcinoma. Journal of immunology (Baltimore, Md : 1950). 2008;181(5):3116-25. Epub 2008/08/21. PubMed PMID: 18713982; PMCID: Pmc2625292.

144.	Moog R, Burger AM, Brandl M, Schuler J, Schubert R, Unger C, Fiebig HH, Massing U. Change in pharmacokinetic and pharmacodynamic behavior of gemcitabine in human tumor xenografts upon entrapment in vesicular phospholipid gels. Cancer chemotherapy and pharmacology. 2002;49(5):356-66. Epub 2002/04/27. doi: 10.1007/s00280-002-0428-4. PubMed PMID: 11976829.

145.	Jia Y, Xie J. Promising molecular mechanisms responsible for gemcitabine resistance in cancer. Genes & Diseases. 2015;2(4):299-306. doi: https://doi.org/10.1016/j.gendis.2015.07.003.

146.	Reid JM, Qu W, Safgren SL, Ames MM, Krailo MD, Seibel NL, Kuttesch J, Holcenberg J. Phase I Trial and Pharmacokinetics of Gemcitabine in Children With Advanced Solid Tumors. Journal of Clinical Oncology. 2004;22(12):2445-51. doi: 10.1200/jco.2004.10.142. PubMed PMID: 15197207.

147.	Dugbartey GJ, Peppone LJ, de Graaf IAM. An integrative view of cisplatin-induced renal and cardiac toxicities: Molecular mechanisms, current treatment challenges and potential protective measures. Toxicology. 2016;371:58-66. Epub 2016/10/04. doi: 10.1016/j.tox.2016.10.001. PubMed PMID: 27717837.

148.	Moufarij MA, Phillips DR, Cullinane C. Gemcitabine potentiates cisplatin cytotoxicity and inhibits repair of cisplatin-DNA damage in ovarian cancer cell lines. Molecular pharmacology. 2003;63(4):862-9. Epub 2003/03/20. doi: 10.1124/mol.63.4.862. PubMed PMID: 12644587.

149.	Peters GJ, Van Moorsel CJ, Lakerveld B, Smid K, Noordhuis P, Comijn EC, Weaver D, Willey JC, Voorn D, Van der Vijgh WJ, Pinedo HM. Effects of gemcitabine on cis-platinum-DNA adduct formation and repair in a panel of gemcitabine and cisplatin-sensitive or -resistant human ovarian cancer cell lines. International journal of oncology. 2006;28(1):237-44. Epub 2005/12/06. PubMed PMID: 16328001.

150.	van Moorsel CJ, Pinedo HM, Veerman G, Bergman AM, Kuiper CM, Vermorken JB, van der Vijgh WJ, Peters GJ. Mechanisms of synergism between cisplatin and gemcitabine in ovarian and non-small-cell lung cancer cell lines. British journal of cancer. 1999;80(7):981-90. Epub 1999/06/11. doi: 10.1038/sj.bjc.6690452. PubMed PMID: 10362105; PMCID: Pmc2363050.

151.	Dicko A, Mayer LD, Tardi PG. Use of nanoscale delivery systems to maintain synergistic drug ratios in vivo. Expert opinion on drug delivery. 2010;7(12):1329-41. doi: 10.1517/17425247.2010.538678.

152.	Mayer LD, Harasym TO, Tardi PG, Harasym NL, Shew CR, Johnstone SA, Ramsay EC, Bally MB, Janoff AS. Ratiometric dosing of anticancer drug combinations: controlling drug ratios after systemic administration regulates therapeutic activity in tumor-bearing mice. Molecular cancer therapeutics. 2006;5(7):1854-63. Epub 2006/08/08. doi: 10.1158/1535-7163.mct-06-0118. PubMed PMID: 16891472.

153.	Meng F, Han N, Yeo Y. Organic nanoparticle systems for spatiotemporal control of multimodal chemotherapy. Expert opinion on drug delivery. 2017;14(3):427-46. Epub 2016/08/02. doi: 10.1080/17425247.2016.1218464. PubMed PMID: 27476442; PMCID: Pmc5385259.

154.	Meng H, Nel AE. Use of nano engineered approaches to overcome the stromal barrier in pancreatic cancer. Advanced Drug Delivery Reviews. 2018;130:50-7. doi: https://doi.org/10.1016/j.addr.2018.06.014.

155.   Nath S, Mukherjee P. MUC1: a multifaceted oncoprotein with a key role in cancer progression. Trends in molecular medicine. 2014;20(6):332-42. Epub 2014/03/29. doi: 10.1016/j.molmed.2014.02.007. PubMed PMID: 24667139; PMCID: Pmc5500204.

156.   Lang JM, Andrei AC, McNeel DG. Prioritization of cancer antigens: keeping the target in sight. Expert review of vaccines. 2009;8(12):1657-61. Epub 2009/12/01. doi: 10.1586/erv.09.134. PubMed PMID: 19943761.

157.   Qu CF, Li Y, Song YJ, Rizvi SM, Raja C, Zhang D, Samra J, Smith R, Perkins AC, Apostolidis C, Allen BJ. MUC1 expression in primary and metastatic pancreatic cancer cells for in vitro treatment by (213)Bi-C595 radioimmunoconjugate. British journal of cancer. 2004;91(12):2086-93. Epub 2004/12/16. doi: 10.1038/sj.bjc.6602232. PubMed PMID: 15599383; PMCID: Pmc2409789.

158.   Zhou R, Curry JM, Roy LD, Grover P, Haider J, Moore LJ, Wu S-t, Kamesh A, Yazdanifar M, Ahrens WA, Leung T, Mukherjee P. A Novel Association of Neuropilin-1 and MUC1 in Pancreatic Ductal Adenocarcinoma: Role in Induction of VEGF Signaling and Angiogenesis. Oncogene. 2016;35(43):5608-18. doi: 10.1038/onc.2015.516. PubMed PMID: PMC4960005.

159.   Curry JM, Thompson KJ, Rao SG, Besmer DM, Murphy AM, Grdzelishvili VZ, Ahrens WA, McKillop IH, Sindram D, Iannitti DA, Martinie JB, Mukherjee P. The Use of a Novel MUC1 Antibody to Identify Cancer Stem Cells and Circulating MUC1 in Mice and Patients With Pancreatic Cancer. Journal of surgical oncology. 2013;107(7):10.1002/jso.23316. doi: 10.1002/jso.23316. PubMed PMID: PMC3880940.

160.   Roy LD, Dillon LM, Zhou R, Moore LJ, Livasy C, El-Khoury JM, Puri R, Mukherjee P. A tumor specific antibody to aid breast cancer screening in women with dense breast tissue. Genes & Cancer. 2017;8(3-4):536-49. doi: 10.18632/genesandcancer.134. PubMed PMID: PMC5489651.

161.   Alvarez-Berríos MP, Vivero-Escoto JL. In vitro evaluation of folic acid-conjugated redox-responsive mesoporous silica nanoparticles for the delivery of cisplatin. International journal of nanomedicine. 2016;11:6251-65. doi: 10.2147/IJN.S118196. PubMed PMID: 27920531.

162.   Dasari M, Acharya AP, Kim D, Lee S, Lee S, Rhea J, Molinaro R, Murthy N. H-Gemcitabine: A New Gemcitabine Prodrug for Treating Cancer. Bioconjugate Chemistry. 2013;24(1):4-8. doi: 10.1021/bc300095m.

163.   Dréau D, Moore LJ, Alvarez-Berrios MP, Tarannum M, Mukherjee P, Vivero-Escoto JL. Mucin-1-Antibody-Conjugated Mesoporous Silica Nanoparticles for Selective Breast Cancer Detection in a Mucin-1 Transgenic Murine Mouse Model. J Biomed Nanotechnol. 2016;12(12):2172-84. doi: 10.1166/jbn.2016.2318. PubMed PMID: 28522938.

164.   Walker WA, Tarannum M, Vivero-Escoto JL. Cellular Endocytosis and Trafficking of Cholera Toxin B-Modified Mesoporous Silica Nanoparticles. J Mater Chem B. 2016;4(7):1254-62. Epub 01/07. doi: 10.1039/C5TB02079D. PubMed PMID: 27134749.

165.   Bouchoucha M, Côté M-F, C.-Gaudreault R, Fortin M-A, Kleitz F. Size-Controlled Functionalized Mesoporous Silica Nanoparticles for Tunable Drug Release and Enhanced Anti-Tumoral Activity. Chemistry of Materials. 2016;28(12):4243-58. doi: 10.1021/acs.chemmater.6b00877.

166.   Sun Y, Kunc F, Balhara V, Coleman B, Kodra O, Raza M, Chen M, Brinkmann A, Lopinski GP, Johnston LJ. Quantification of amine functional groups on silica nanoparticles: a multi-method approach. Nanoscale Advances. 2019;1(4):1598-607. doi: 10.1039/C9NA00016J.

167.   Nadrah P, Porta F, Planinšek O, Kros A, Gaberšček M. Poly(propylene imine) dendrimer caps on mesoporous silica nanoparticles for redox-responsive release: smaller is better. Physical Chemistry Chemical Physics. 2013;15(26):10740-8. doi: 10.1039/C3CP44614J.

168.   Lopez-Acevedo M, Grace L, Teoh D, Whitaker R, Adams DJ, Jia J, Nixon AB, Secord AA. Dasatinib (BMS-35482) potentiates the activity of gemcitabine and docetaxel in uterine leiomyosarcoma cell lines. Gynecologic Oncology Research and Practice. 2014;1:2. doi: 10.1186/2053-6844-1-2. PubMed PMID: PMC4877815.

169.   Tomayko MM, Reynolds CP. Determination of subcutaneous tumor size in athymic (nude) mice. Cancer Chemother Pharmacol. 1989;24(3):148-54. Epub 1989/01/01. doi: 10.1007/bf00300234. PubMed PMID: 2544306.

170.   Wu S-t, Williams CD, Grover PA, Moore LJ, Mukherjee P. Early detection of pancreatic cancer in mouse models using a novel antibody, TAB004. PLoS One. 2018;13(2):e0193260. doi: 10.1371/journal.pone.0193260.

171.   Miao L, Guo S, Zhang J, Kim WY, Huang L. Nanoparticles with Precise Ratiometric Co-Loading and Co-Delivery of Gemcitabine Monophosphate and Cisplatin for Treatment of Bladder Cancer. Adv Funct Mater. 2014;24(42):6601-11. doi: 10.1002/adfm.201401076. PubMed PMID: 25395922.

172.   Gadde S. Multi-drug delivery nanocarriers for combination therapy. MedChemComm. 2015;6(11):1916-29. doi: 10.1039/C5MD00365B.

173.   Moysan E, Bastiat G, Benoit J-P. Gemcitabine versus Modified Gemcitabine: A Review of Several Promising Chemical Modifications. Molecular Pharmaceutics. 2013;10(2):430-44. doi: 10.1021/mp300370t.

174.   Moysan E, Bastiat G, Benoit JP. Gemcitabine versus Modified Gemcitabine: a review of several promising chemical modifications. Mol Pharm. 2013;10(2):430-44. Epub 2012/09/18. doi: 10.1021/mp300370t. PubMed PMID: 22978251.

175.   Lansakara PD, Rodriguez BL, Cui Z. Synthesis and in vitro evaluation of novel lipophilic monophosphorylated gemcitabine derivatives and their nanoparticles. International journal of pharmaceutics. 2012;429(1-2):123-34. Epub 2012/03/20. doi: 10.1016/j.ijpharm.2012.03.014. PubMed PMID: 22425885; PMCID: PMC3335205.

176.   Besancon OG, Tytgat GA, Meinsma R, Leen R, Hoebink J, Kalayda GV, Jaehde U, Caron HN, van Kuilenburg AB. Synergistic interaction between cisplatin and gemcitabine in neuroblastoma cell lines and multicellular tumor spheroids. Cancer letters. 2012;319(1):23-30. Epub 2011/12/21. doi: 10.1016/j.canlet.2011.12.016. PubMed PMID: 22182450.

177.   Fortuni B, Inose T, Ricci M, Fujita Y, Van Zundert I, Masuhara A, Fron E, Mizuno H, Latterini L, Rocha S, Uji-I H. Polymeric Engineering of Nanoparticles for Highly Efficient Multifunctional Drug Delivery Systems. Scientific reports. 2019;9(1):2666-. doi: 10.1038/s41598-019-39107-3. PubMed PMID: 30804375.

178.   Immordino ML, Brusa P, Rocco F, Arpicco S, Ceruti M, Cattel L. Preparation, characterization, cytotoxicity and pharmacokinetics of liposomes containing lipophilic

gemcitabine prodrugs. J Control Release. 2004;100(3):331-46. Epub 2004/11/30. doi: 10.1016/j.jconrel.2004.09.001. PubMed PMID: 15567500.

179.   Mah LJ, El-Osta A, Karagiannis TC. γH2AX: a sensitive molecular marker of DNA damage and repair. Leukemia. 2010;24(4):679-86. doi: 10.1038/leu.2010.6.

180.   Zhou B-BS, Elledge SJ. The DNA damage response: putting checkpoints in perspective. Nature. 2000;408(6811):433-9. doi: 10.1038/35044005.

181.   Giglia-Mari G, Zotter A, Vermeulen W. DNA damage response. Cold Spring Harb Perspect Biol. 2011;3(1):a000745-a. doi: 10.1101/cshperspect.a000745. PubMed PMID: 20980439.

182.   van Engeland M, Nieland LJ, Ramaekers FC, Schutte B, Reutelingsperger CP. Annexin V-affinity assay: a review on an apoptosis detection system based on phosphatidylserine exposure. Cytometry. 1998;31(1):1-9. Epub 1998/02/05. PubMed PMID: 9450519.

183.   Rieger AM, Nelson KL, Konowalchuk JD, Barreda DR. Modified annexin V/propidium iodide apoptosis assay for accurate assessment of cell death. Journal of visualized experiments : JoVE. 2011(50):2597. doi: 10.3791/2597. PubMed PMID: 21540825.

184.   Xu S, Olenyuk BZ, Okamoto CT, Hamm-Alvarez SF. Targeting receptor-mediated endocytotic pathways with nanoparticles: rationale and advances. Advanced drug delivery reviews. 2013;65(1):121-38. Epub 09/29. doi: 10.1016/j.addr.2012.09.041. PubMed PMID: 23026636.

185.   Behzadi S, Serpooshan V, Tao W, Hamaly MA, Alkawareek MY, Dreaden EC, Brown D, Alkilany AM, Farokhzad OC, Mahmoudi M. Cellular uptake of nanoparticles: journey inside the cell. Chemical Society reviews. 2017;46(14):4218-44. doi: 10.1039/c6cs00636a. PubMed PMID: 28585944.

186.   Yu JW, Bhattacharya S, Yanamandra N, Kilian D, Shi H, Yadavilli S, Katlinskaya Y, Kaczynski H, Conner M, Benson W, Hahn A, Seestaller-Wehr L, Bi M, Vitali NJ, Tsvetkov L, Halsey W, Hughes A, Traini C, Zhou H, Jing J, Lee T, Figueroa DJ, Brett S, Hopson CB, Smothers JF, Hoos A, Srinivasan R. Tumor-immune profiling of murine syngeneic tumor models as a framework to guide mechanistic studies and predict therapy response in distinct tumor microenvironments. PLoS One. 2018;13(11):e0206223-e. doi: 10.1371/journal.pone.0206223. PubMed PMID: 30388137.

187.   Lu J, Liong M, Li Z, Zink JI, Tamanoi F. Biocompatibility, Biodistribution, and Drug-Delivery Efficiency of Mesoporous Silica Nanoparticles for Cancer Therapy in Animals. Small. 2010;6(16):1794-805. doi: 10.1002/smll.201000538.

188.   Li Z, Zhang Y, Feng N. Mesoporous silica nanoparticles: synthesis, classification, drug loading, pharmacokinetics, biocompatibility, and application in drug delivery. Expert Opinion on Drug Delivery. 2019;16(3):219-37. doi: 10.1080/17425247.2019.1575806.

189.   Hingorani SR, Petricoin EF, Maitra A, Rajapakse V, King C, Jacobetz MA, Ross S, Conrads TP, Veenstra TD, Hitt BA, Kawaguchi Y, Johann D, Liotta LA, Crawford HC, Putt ME, Jacks T, Wright CV, Hruban RH, Lowy AM, Tuveson DA. Preinvasive and invasive ductal pancreatic cancer and its early detection in the mouse. Cancer cell. 2003;4(6):437-50. Epub 2004/01/07. doi: 10.1016/s1535-6108(03)00309-x. PubMed PMID: 14706336.

190.   Mukherjee P, Basu G, Tinder T, Subramani B, Bradley J, Arefayene M, Skaar T, De Petris G. Progression of Pancreatic Adenocarcinoma Is Significantly Impeded with a Combination of Vaccine and COX-2 Inhibition. Journal of immunology (Baltimore, Md : 1950). 2009;182:216-24. doi: 10.4049/jimmunol.182.1.216.

191.   Waghray M, Yalamanchili M, di Magliano MP, Simeone DM. Deciphering the role of stroma in pancreatic cancer. Curr Opin Gastroenterol. 2013;29(5):537-43. doi: 10.1097/MOG.0b013e328363affe. PubMed PMID: 23892539.

192.   Thomas D, Radhakrishnan P. Tumor-stromal crosstalk in pancreatic cancer and tissue fibrosis. Mol Cancer. 2019;18(1):14-. doi: 10.1186/s12943-018-0927-5. PubMed PMID: 30665410.

193.   Feig C, Gopinathan A, Neesse A, Chan DS, Cook N, Tuveson DA. The pancreas cancer microenvironment. Clinical cancer research : an official journal of the American Association for Cancer Research. 2012;18(16):4266-76. Epub 2012/08/17. doi: 10.1158/1078-0432.ccr-11-3114. PubMed PMID: 22896693; PMCID: Pmc3442232.

194.   Xu M, Zhou BP, Tao M, Liu J, Li W. The Role of Stromal Components in Pancreatic Cancer Progression. Anti-cancer agents in medicinal chemistry. 2016;16(9):1117-24. Epub 2016/04/05. PubMed PMID: 27039918.

195.   Feig C, Gopinathan A, Neesse A, Chan DS, Cook N, Tuveson DA. The pancreas cancer microenvironment. Clinical cancer research : an official journal of the American Association for Cancer Research. 2012;18(16):4266-76. doi: 10.1158/1078-0432.CCR-11-3114. PubMed PMID: 22896693.

196.   Zhan H-x, Zhou B, Cheng Y-g, Xu J-w, Wang L, Zhang G-y, Hu S-y. Crosstalk between stromal cells and cancer cells in pancreatic cancer: New insights into stromal biology. Cancer letters. 2017;392(Supplement C):83-93. doi: https://doi.org/10.1016/j.canlet.2017.01.041.

197.   Samandari M, Gil Juliá M, Rice A, Chronopoulos A, del Rio Hernandez A. Liquid Biopsies for Management of Pancreatic Cancer. Translational Research. 2018;201:98-127. doi: 10.1016/j.trsl.2018.07.008.

198.   Gu D, Schlotman KE, Xie J. Deciphering the role of hedgehog signaling in pancreatic cancer. J Biomed Res. 2016;30(5):353-60. Epub 04/10. doi: 10.7555/JBR.30.20150107. PubMed PMID: 27346466.

199.   Tian H, Callahan CA, DuPree KJ, Darbonne WC, Ahn CP, Scales SJ, de Sauvage FJ. Hedgehog signaling is restricted to the stromal compartment during pancreatic carcinogenesis. Proceedings of the National Academy of Sciences of the United States of America. 2009;106(11):4254-9. Epub 02/25. doi: 10.1073/pnas.0813203106. PubMed PMID: 19246386.

200.   Jesus-Acosta AD, O'Dwyer PJ, Ramanathan RK, Hoff DDV, Maitra A, Rasheed Z, Zheng L, Rajeshkumar NV, Le DT, Hoering A, Bolejack V, Yabuuchi S, Laheru DA. A phase II study of vismodegib, a hedgehog (Hh) pathway inhibitor, combined with gemcitabine and nab-paclitaxel (nab-P) in patients (pts) with untreated metastatic pancreatic ductal adenocarcinoma (PDA). Journal of Clinical Oncology. 2014;32(3_suppl):257-. doi: 10.1200/jco.2014.32.3_suppl.257.

201.   Feldmann G, Habbe N, Dhara S, Bisht S, Alvarez H, Fendrich V, Beaty R, Mullendore M, Karikari C, Bardeesy N, Ouellette MM, Yu W, Maitra A. Hedgehog inhibition prolongs survival in a genetically engineered mouse model of pancreatic

cancer. Gut. 2008;57(10):1420-30. Epub 2008/06/03. doi: 10.1136/gut.2007.148189. PubMed PMID: 18515410; PMCID: PMC2707354.

202.   Thayer SP, di Magliano MP, Heiser PW, Nielsen CM, Roberts DJ, Lauwers GY, Qi YP, Gysin S, Fernandez-del Castillo C, Yajnik V, Antoniu B, McMahon M, Warshaw AL, Hebrok M. Hedgehog is an early and late mediator of pancreatic cancer tumorigenesis. Nature. 2003;425(6960):851-6. Epub 2003/10/02. doi: 10.1038/nature02009. PubMed PMID: 14520413; PMCID: PMC3688051.

203.   Yao J, An Y, Wie JS, Ji ZL, Lu ZP, Wu JL, Jiang KR, Chen P, Xu ZK, Miao Y. Cyclopamine reverts acquired chemoresistance and down-regulates cancer stem cell markers in pancreatic cancer cell lines. Swiss medical weekly. 2011;141:w13208. Epub 2011/06/02. doi: 10.4414/smw.2011.13208. PubMed PMID: 21630164.

204.   Li X, Ma Q, Duan W, Liu H, Xu H, Wu E. Paracrine Sonic Hedgehog Signaling Derived from Tumor Epithelial Cells: A Key Regulator in the Pancreatic Tumor Microenvironment. Critical reviews in eukaryotic gene expression. 2012;22:97-108. doi: 10.1615/CritRevEukarGeneExpr.v22.i2.20.

205.   Bailey JM, Swanson BJ, Hamada T, Eggers JP, Singh PK, Caffery T, Ouellette MM, Hollingsworth MA. Sonic hedgehog promotes desmoplasia in pancreatic cancer. Clinical cancer research : an official journal of the American Association for Cancer Research. 2008;14(19):5995-6004. Epub 2008/10/03. doi: 10.1158/1078-0432.ccr-08-0291. PubMed PMID: 18829478; PMCID: PMC2782957.

206.   Tian H, Callahan CA, DuPree KJ, Darbonne WC, Ahn CP, Scales SJ, de Sauvage FJ. Hedgehog signaling is restricted to the stromal compartment during pancreatic carcinogenesis. Proceedings of the National Academy of Sciences of the United States of America. 2009;106(11):4254-9. Epub 2009/02/28. doi: 10.1073/pnas.0813203106. PubMed PMID: 19246386; PMCID: PMC2647977.

207.   Pasca di Magliano M, Hebrok M. Hedgehog signalling in cancer formation and maintenance. Nature reviews Cancer. 2003;3(12):903-11. Epub 2004/01/23. doi: 10.1038/nrc1229. PubMed PMID: 14737121.

208.   Olive KP, Jacobetz MA, Davidson CJ, Gopinathan A, McIntyre D, Honess D, Madhu B, Goldgraben MA, Caldwell ME, Allard D, Frese KK, Denicola G, Feig C, Combs C, Winter SP, Ireland-Zecchini H, Reichelt S, Howat WJ, Chang A, Dhara M, Wang L, Ruckert F, Grutzmann R, Pilarsky C, Izeradjene K, Hingorani SR, Huang P, Davies SE, Plunkett W, Egorin M, Hruban RH, Whitebread N, McGovern K, Adams J, Iacobuzio-Donahue C, Griffiths J, Tuveson DA. Inhibition of Hedgehog signaling enhances delivery of chemotherapy in a mouse model of pancreatic cancer. Science. 2009;324(5933):1457-61. Epub 2009/05/23. doi: 10.1126/science.1171362. PubMed PMID: 19460966; PMCID: PMC2998180.

209.   Yan BY, Hibler BP, Menge T, Dunn L, Ho AL, Rossi AM. Sonic Hedgehog pathway inhibitors: from clinical trials to clinical practice. British Journal of Dermatology. 2019;180(5):1260-1. doi: 10.1111/bjd.17692.

210.   Catenacci DV, Junttila MR, Karrison T, Bahary N, Horiba MN, Nattam SR, Marsh R, Wallace J, Kozloff M, Rajdev L, Cohen D, Wade J, Sleckman B, Lenz HJ, Stiff P, Kumar P, Xu P, Henderson L, Takebe N, Salgia R, Wang X, Stadler WM, de Sauvage FJ, Kindler HL. Randomized Phase Ib/II Study of Gemcitabine Plus Placebo or Vismodegib, a Hedgehog Pathway Inhibitor, in Patients With Metastatic Pancreatic Cancer. Journal of clinical oncology : official journal of the American Society of Clinical

Oncology. 2015;33(36):4284-92. Epub 2015/11/04. doi: 10.1200/jco.2015.62.8719. PubMed PMID: 26527777; PMCID: Pmc4678179.

211.   Berlin J, Bendell JC, Hart LL, Firdaus I, Gore I, Hermann RC, Mulcahy MF, Zalupski MM, Mackey HM, Yauch RL, Graham RA, Bray GL, Low JA. A randomized phase II trial of vismodegib versus placebo with FOLFOX or FOLFIRI and bevacizumab in patients with previously untreated metastatic colorectal cancer. Clinical cancer research : an official journal of the American Association for Cancer Research. 2013;19(1):258-67. Epub 2012/10/20. doi: 10.1158/1078-0432.ccr-12-1800. PubMed PMID: 23082002.

212.   Catenacci DVT, Junttila MR, Karrison T, Bahary N, Horiba MN, Nattam SR, Marsh R, Wallace J, Kozloff M, Rajdev L, Cohen D, Wade J, Sleckman B, Lenz H-J, Stiff P, Kumar P, Xu P, Henderson L, Takebe N, Salgia R, Wang X, Stadler WM, Sauvage FJd, Kindler HL. Randomized Phase Ib/II Study of Gemcitabine Plus Placebo or Vismodegib, a Hedgehog Pathway Inhibitor, in Patients With Metastatic Pancreatic Cancer. Journal of Clinical Oncology. 2015;33(36):4284-92. doi: 10.1200/jco.2015.62.8719. PubMed PMID: 26527777.

213.   Mathew E, Zhang Y, Holtz AM, Kane KT, Song JY, Allen BL, Pasca di Magliano M. Dosage-dependent regulation of pancreatic cancer growth and angiogenesis by hedgehog signaling. Cell Rep. 2014;9(2):484-94. Epub 2014/10/15. doi: 10.1016/j.celrep.2014.09.010. PubMed PMID: 25310976; PMCID: Pmc4362534.

214.   Rhim AD, Oberstein PE, Thomas DH, Mirek ET, Palermo CF, Sastra SA, Dekleva EN, Saunders T, Becerra CP, Tattersall IW, Westphalen CB, Kitajewski J, Fernandez-Barrena MG, Fernandez-Zapico ME, Iacobuzio-Donahue C, Olive KP, Stanger BZ. Stromal elements act to restrain, rather than support, pancreatic ductal adenocarcinoma. Cancer cell. 2014;25(6):735-47. Epub 2014/05/27. doi: 10.1016/j.ccr.2014.04.021. PubMed PMID: 24856585; PMCID: PMC4096698.

215.   Shim G, Kim M-G, Kim D, Park JY, Oh Y-K. Nanoformulation-based sequential combination cancer therapy. Advanced Drug Delivery Reviews. 2017;115(Supplement C):57-81. doi: https://doi.org/10.1016/j.addr.2017.04.003.

216.   Zhang B, Wang H, Jiang T, Jin K, Luo Z, Shi W, Mei H, Wang H, Hu Y, Pang Z, Jiang X. Cyclopamine treatment disrupts extracellular matrix and alleviates solid stress to improve nanomedicine delivery for pancreatic cancer. Journal of drug targeting. 2018;26(10):913-9. Epub 2018/03/14. doi: 10.1080/1061186x.2018.1452243. PubMed PMID: 29533111.

217.   Zhao J, Wu C, Abbruzzese J, Hwang RF, Li C. Cyclopamine-Loaded Core-Cross-Linked Polymeric Micelles Enhance Radiation Response in Pancreatic Cancer and Pancreatic Stellate Cells. Molecular Pharmaceutics. 2015;12(6):2093-100. doi: 10.1021/mp500875f.

218.   Zhao J, Wang H, Hsiao C-H, Chow DSL, Koay EJ, Kang Y, Wen X, Huang Q, Ma Y, Bankson JA, Ullrich SE, Overwijk W, Maitra A, Piwnica-Worms D, Fleming JB, Li C. Simultaneous inhibition of hedgehog signaling and tumor proliferation remodels stroma and enhances pancreatic cancer therapy. Biomaterials. 2018;159:215-28. doi: https://doi.org/10.1016/j.biomaterials.2018.01.014.

219.   Zhang B, Wang H, Jiang T, Jin K, Luo Z, Shi W, Mei H, Wang H, Hu Y, Pang Z, Jiang X. Cyclopamine treatment disrupts extracellular matrix and alleviates solid stress to

improve nanomedicine delivery for pancreatic cancer. Journal of drug targeting. 2018;26(10):913-9. doi: 10.1080/1061186X.2018.1452243.

220.   Xu M, Li L, Liu Z, Jiao Z, Xu P, Kong X, Huang H, Zhang Y. ABCB2 (TAP1) as the downstream target of SHH signaling enhances pancreatic ductal adenocarcinoma drug resistance. Cancer Letters. 2013;333(2):152-8. doi: https://doi.org/10.1016/j.canlet.2013.01.002.

221.   Cochrane CR, Szczepny A, Watkins DN, Cain JE. Hedgehog Signaling in the Maintenance of Cancer Stem Cells. Cancers (Basel). 2015;7(3):1554-85. doi: 10.3390/cancers7030851. PubMed PMID: 26270676.

222.   Karaca M, Dutta R, Ozsoy Y, Mahato RI. Micelle Mixtures for Coadministration of Gemcitabine and GDC-0449 To Treat Pancreatic Cancer. Molecular pharmaceutics. 2016;13(6):1822-32. Epub 04/27. doi: 10.1021/acs.molpharmaceut.5b00971. PubMed PMID: 26981724.

223.   Ansari D, Bauden MP, Sasor A, Gundewar C, Andersson R. Analysis of MUC4 expression in human pancreatic cancer xenografts in immunodeficient mice. Anticancer research. 2014;34(8):3905-10. Epub 2014/07/31. PubMed PMID: 25075011.

224.   Becker AE, Hernandez YG, Frucht H, Lucas AL. Pancreatic ductal adenocarcinoma: Risk factors, screening, and early detection. World Journal of Gastroenterology : WJG. 2014;20(32):11182-98. doi: 10.3748/wjg.v20.i32.11182. PubMed PMID: PMC4145757.

225.   Yachida S, Jones S, Bozic I, Antal T, Leary R, Fu B, Kamiyama M, Hruban RH, Eshleman JR, Nowak MA, Velculescu VE, Kinzler KW, Vogelstein B, Iacobuzio-Donahue CA. Distant metastasis occurs late during the genetic evolution of pancreatic cancer. Nature. 2010;467(7319):1114-7. doi: http://www.nature.com/nature/journal/v467/n7319/abs/10.1038-nature09515-unlocked.html#supplementary-information.

226.   Canto MI, Harinck F, Hruban RH, Offerhaus GJ, Poley JW, Kamel I, Nio Y, Schulick RS, Bassi C, Kluijt I, Levy MJ, Chak A, Fockens P, Goggins M, Bruno M. International Cancer of the Pancreas Screening (CAPS) Consortium summit on the management of patients with increased risk for familial pancreatic cancer. Gut. 2013;62(3):339-47. Epub 2012/11/09. doi: 10.1136/gutjnl-2012-303108. PubMed PMID: 23135763; PMCID: Pmc3585492.

227.   Kaur S, Kumar S, Momi N, Sasson AR, Batra SK. Mucins in pancreatic cancer and its microenvironment. Nature reviews Gastroenterology & hepatology. 2013;10(10):607-20. doi: 10.1038/nrgastro.2013.120. PubMed PMID: PMC3934431.

228.   Yonezawa S, Higashi M, Yamada N, Goto M. Precursor Lesions of Pancreatic Cancer. Gut and Liver. 2008;2(3):137-54. doi: 10.5009/gnl.2008.2.3.137. PubMed PMID: PMC2871636.

229.   Dreau D, Moore LJ, Alvarez-Berrios MP, Tarannum M, Mukherjee P, Vivero-Escoto JL. Mucin-1-Antibody-Conjugated Mesoporous Silica Nanoparticles for Selective Breast Cancer Detection in a Mucin-1 Transgenic Murine Mouse Model. Journal of biomedical nanotechnology. 2016;12(12):2172-84. Epub 2017/05/20. doi: 10.1166/jbn.2016.2318. PubMed PMID: 28522938; PMCID: Pmc5431076.

230.   Chen Y, Chen H, Shi J. In vivo bio-safety evaluations and diagnostic/therapeutic applications of chemically designed mesoporous silica nanoparticles. Advanced materials

(Deerfield Beach, Fla). 2013;25(23):3144-76. Epub 2013/05/18. doi: 10.1002/adma.201205292. PubMed PMID: 23681931.

231.   Chen F, Ma K, Zhang L, Madajewski B, Zanzonico P, Sequeira S, Gonen M, Wiesner U, Bradbury MS. Target-or-Clear Zirconium-89 Labeled Silica Nanoparticles for Enhanced Cancer-Directed Uptake in Melanoma: A Comparison of Radiolabeling Strategies. Chemistry of Materials. 2017. doi: 10.1021/acs.chemmater.7b02567.